Naval Research Laboratory

Stennis Space Center, MS 39529-5004

NRL/MR/7320--10-9262

The Coastal Dynamics of Heterogeneous Sedimentary Environments: Numerical Modeling of Hydrodynamics and Mass Transport in Estuaries

TIMOTHY R. KEEN

Ocean Dynamics and Prediction Branch
Oceanography Division

K. TODD HOLLAND

Seafloor Sciences Branch
Marine Geosciences Division

August 12, 2010

REPORT DOCUMENTATION PAGE

Form Approved
OMB No. 0704-0188

1. REPORT DATE *(DD-MM-YYYY)*	2. REPORT TYPE	3. DATES COVERED *(From - To)*
12-08-2010	Memorandum Report	

4. TITLE AND SUBTITLE

The Coastal Dynamics of Heterogeneous Sedimentary Environments: Numerical Modeling of Hydrodynamics and Mass Transport in Estuaries

5a. CONTRACT NUMBER

5b. GRANT NUMBER

5c. PROGRAM ELEMENT NUMBER
0601153N

6. AUTHOR(S)

Timothy R. Keen and K. Todd Holland

5d. PROJECT NUMBER

5e. TASK NUMBER

5f. WORK UNIT NUMBER
73-4261-00-5

7. PERFORMING ORGANIZATION NAME(S) AND ADDRESS(ES)

Naval Research Laboratory
Oceanography Division
Stennis Space Center, MS 39529-5004

8. PERFORMING ORGANIZATION REPORT NUMBER

NRL/MR/7320--10-9262

9. SPONSORING / MONITORING AGENCY NAME(S) AND ADDRESS(ES)

Office of Naval Research
One Liberty Center
875 North Randolph Street
Arlington, VA 22203-1995

10. SPONSOR / MONITOR'S ACRONYM(S)

ONR

11. SPONSOR / MONITOR'S REPORT NUMBER(S)

12. DISTRIBUTION / AVAILABILITY STATEMENT

Approved for public release; distribution is unlimited.

13. SUPPLEMENTARY NOTES

14. ABSTRACT

This report discusses details of the numerical algorithms used to simulate wave, tide, and wind-driven hydrodynamics in estuaries and coastal bays. The impacts of the predicted flow on mass transport in estuaries are examined. The results of several sample problems are presented and compared to observations where possible. The results are intended to be used as guidance in formulating modeling strategies for different coastal environments and specific applications.

15. SUBJECT TERMS

Estuaries
Numerical models
San Francisco Bay
St. Louis Bay

16. SECURITY CLASSIFICATION OF:			17. LIMITATION OF ABSTRACT	18. NUMBER OF PAGES	19a. NAME OF RESPONSIBLE PERSON
a. REPORT	b. ABSTRACT	c. THIS PAGE			Timothy Keen
Unclassified	Unclassified	Unclassified	SAR	137	19b. TELEPHONE NUMBER *(include area code)* (288) 688-4950

Table of Contents

The Coastal Dynamics of Heterogeneous Sedimentary Environments: Numerical Modeling of Hydrodynamics and Mass Transport in Estuaries i

1 Introduction 1

2 Approach 10

2.1 Observations and Modeled Oceanographic Databases 10

2.2 Numerical Models 11

3 Wind and tidal circulation in the Mullica-Great Bay Estuary, New Jersey 13

3.1 Forecasts of estuarine circulation in July, 2000 13

3.2 Hindcasts of the MGBE circulation in November, 1999 15

3.3 Sediment resuspension in Little Egg Inlet 16

4 Wind and tidal circulation in the Kotar-Boka Bay estuary, Montenegro 34

5 Hydrodynamics, sediment resuspension, and contaminant transport in San Francisco Bay, California 40

5.1 Circulation in San Francisco Bay 40

5.2 Modeling Hydrodynamics in San Francisco Bay and the south Basin of Hunters Point Shipyard 41

5.2.1 Approach 42

5.2.2 Model validation 43

5.2.3 Hindcast wind, waves, and currents at Hunter Point 45

5.3 Contaminant release and potential transport during southeasterly wind events 46

5.3.1 Approach 47

5.3.2 Model validation and results 47
5.4 Summary 51
6 Estuarine circulation and mass transport in St. Louis Bay and Mississippi Sound 73
6.1 Background 74
6.1.1 Circulation in Mississippi Sound and St. Louis Bay 74
6.1.2 Anthropogenic toxins in St. Louis Bay 76
6.2 Atmospheric forcing in the northern Gulf of Mexico 77
6.3 Numerical modeling 78
6.3.1 NCOM validation 79
6.3.2 Tidal circulation 80
6.3.3 Baroclinic circulation and mass transport during a cold front (March 2005) 80
6.3.4 Combined flow during back-to-back cold fronts (December 2005) 81
6.3.5 Circulation and mass transport during Hurricane Katrina (August 2005) 83
6.4 Discussion and summary 85
7 Summary 115
7.1 The estuary as a transitional environment 115
7.2 Multiscale and multimodeling approaches in estuaries 116
8 References 118

1 Introduction

The Office of Naval Research (ONR) has demonstrated an ongoing interest in physical and geochemical processes within the coastal waters around the world, including northern California (Ogston, Cacchione et al. 2000), Papua New Guinea (Kineke, Woolfe et al. 2000), the Amazon shelf (Gibbs 1967), the Louisiana shelf (Kineke, Higgins et al. 2006), and the Adriatic Sea (Lee, Orlic et al. 2007; Harris, Sherwood et al. 2008). These efforts have focused on mixing processes on the continental shelf. The work discussed in this report complements this effort by examining transport processes within estuaries and export to the inner shelf.

An estuary can be defined as *"a semi-enclosed coastal body of water, which has a free connection with the open sea, and within which sea water is measurably diluted with freshwater derived from land drainage"* (Pritchard 1967). Although this definition is general and applies to all coastal water bodies, it has been expanded; *"a semi-enclosed body of water connected to the sea as far as the tidal limit or the salt intrusion limit and receiving freshwater runoff; however the freshwater inflow may not be perennial, the connection to the sea may be closed for part of the year and tidal influence may be negligible"* (Wolanski 2007). The definition of an estuary thus includes well-known water bodies like the Hudson River estuary as well as fjords, lagoons, river mouths, and tidal creeks. A practical definition of an estuary extends between the 1 PSU and the 30 PSU salinity isotherms.

The most common classifications of estuaries are based on either geomorphology or circulation. There are four kinds of geomorphological estuaries: (1) drowned river valleys; (2) lagoons or bar-built; (3) fjords; and (4) tectonically formed. The most common are drowned river valleys like Chesapeake and Galveston Bays. These were formed when sealevel rose 100-130 m between 15000 and 6000 years ago (Roman, Jaworski et al. 2000); they are <40 m in depth. Lagoons are separated from the open ocean by barrier islands, which form by overwash, wave and onshore winds acting on submarine bars and river-discharged sand, flooding of Holocene beach ridges, and elongation of barrier spits by alongshore currents (Leatherman 1987). Examples of this type of estuary include Pamlico Sound, North Carolina, and Mississippi Sound in the Gulf of Mexico. These estuaries are typically <5 m deep. Fjords were formed when glacial valleys flooded as sealevel rose. They have sills <100 m at their entrances that are formed by glacial deposits or scoured basement rock. Depths can reach 300 m along their axes and they have restricted circulation because of the shallow sills (Bogen 1983). The least common type of estuary is formed by tectonic processes like subsidence, faulting, volcanoes, and landslides (Fairbridge 1980). San Francisco Bay is an excellent example of this type (Jackson 2004). Compound estuaries include components of more than one of these types; for example, Mississippi Sound in the Gulf of Mexico is a bar-built lagoon that incorporates drowned river valleys (e.g., Mobile Bay and St. Louis Bay).

Manuscript approved May 10, 2010.

For the purpose of this report, circulation is the most important way to classify estuaries. The classical estuarine circulation consists of upstream bottom flow of salt water and seaward surface flow of fresh water (Festa and Hansen 1976). Estuaries can be classified as well mixed, partially mixed, and salt wedge types (Fig. 1.1). A well-mixed estuary results from a large tidal flow relative to the river input (Fig. 1.2a). Tidal mixing keeps the water turbulent and reduces stratification, such that the flow oscillates with the tide and residual flow is restricted to the surface. Partially mixed estuaries result from greater river inflow (Fig. 1.2b). A salt-wedge results from very large inflow and weak tidal mixing. Real estuaries exhibit a range of mixing, however, with partially mixed conditions common in the upper estuary and well-mixed salinity near the mouth (Levasseur, Shi et al. 2007). The circulation is further complicated by lateral mixing (Nidzieko, Hench et al. 2009), the tidal cycle (Nakayama, Okada et al. 2005; Guo and Valle-Levinson 2007; Shiraki and Yanagi 2007; Stacey, Fram et al. 2008), freshwater inflow (Yanagi and Shimomura 2006), and long-term meteorological variability (Aoki and Isobe 2006). The interaction of these processes also produces estuaries that have higher salinities than ocean values (reverse estuaries) and net inflow from the ocean (storage estuaries). Discharge circulation results when fresh-water input is sufficient to drive net outflow at all depths (e.g., Mississippi and Amazon Rivers).

Fresh water from river inflow mixes with salt water from offshore in a regular manner, which leads to the development of a dynamic region near the salinity limit (Fig. 1.3) (Menon, Gibbs et al. 1998). This zone is commonly referred to as the estuarine turbidity maximum (ETM). It is characterized by changes in turbulence (Dyer, Christie et al. 2004), properties of fine-grained sediment (Mitchell and West 2002; Manning, Bass et al. 2006; Dickhudt, Friedrichs et al. 2009), dissolved material (Tappin, Harris et al. 2003), geochemical processes (Abril, Etcheber et al. 1999), and biological activity (Hollibaugh and Wong 1999). The ETM is a dynamic zone that varies with time and space (Uncles, Stephens et al. 2002; Park, Wang et al. 2008). The development of the ETM is influenced by gravitational circulation (Schubel 1968), stratification (Geyer, Signell et al. 1993), tidal asymmetry (Jay and Musiak 1994), topography (Allen, Salomon et al. 1980), wind and wave effects (Weir and Mcmanus 1987; Kessarkar, Rao et al. 2009), and flocculation (van Leussen 1988). All estuaries have an ETM but their development and physical characteristics vary substantially. An ETM can occur in small mountainous rivers (Liu, Hung et al. 2009), large rivers (Kineke, Sternberg et al. 1996), highly-turbid rivers (Uncles, Stephens et al. 2006; Deloffre, Verney et al. 2007), low-turbidity rivers (Goni, Cathey et al. 2005), microtidal estuaries (Kostoglidis, Pattiaratchi et al. 2005), macrotidal estuaries (Yang, Eisma et al. 2000), and estuaries with fringing mangrove swamps (Anthony 2004). Estuaries and the mixing zones that occur within them are good candidates for simultions with numerical models because of this complex interplay of processes.

River water carries to the inner shelf, including a variety of allogenic material that is supplemented by authigenic substances produced within the ETM and estuary. This mixed water enters the coastal ocean as a plume, which is characterized by low-salinity, turbid water

with high concentrations of biogeochemical material (Wiltshire, Harsdorf et al. 1998; Chen, Li et al. 2004; Valente and da Silva 2009). Figure 1.4 shows an example of the surface expression of these turbid waters. The estuarine plume is typically restricted to the surface layer after it reaches the ocean (Fig. 1.5) (Kineke, Woolfe et al. 2000). Once delivered to the inner shelf (< 30 m depths), the river load is deposited, processed, or dissipated to become part of the coastal ocean.

The objective of this report is to document studies at NRL on the dynamics of exchange between estuaries and the inner shelf. This work was undertaken as part of several projects within the 6.1/6.2 base program. Examples of applying ocean circulation models to estuarine circulation in a straightforward manner will be briefly discussed and examples that are more complex will be described in detail. This work has shown that it is feasible to simulate these complex regions with operational models but that there are several caveats that must be considered in doing so.

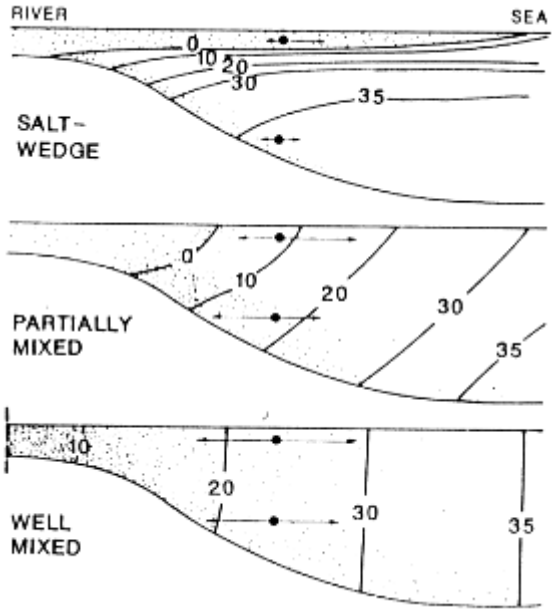

Figure 1.1. Schematic sections of general types of estuaries. Fresh water from a river enters an estuary (top) and ocean water forms a salt wedge. The degree of vertical mixing determines the type of estuary. If salinity gradients are angled (center), the estuary is partially mixed. Vertical salinity gradients (bottom) indicate a well-mixed estuary. SOURCE: http://www.icsu-scope.org/downloadpubs/scope50/images/fig5.7.gif

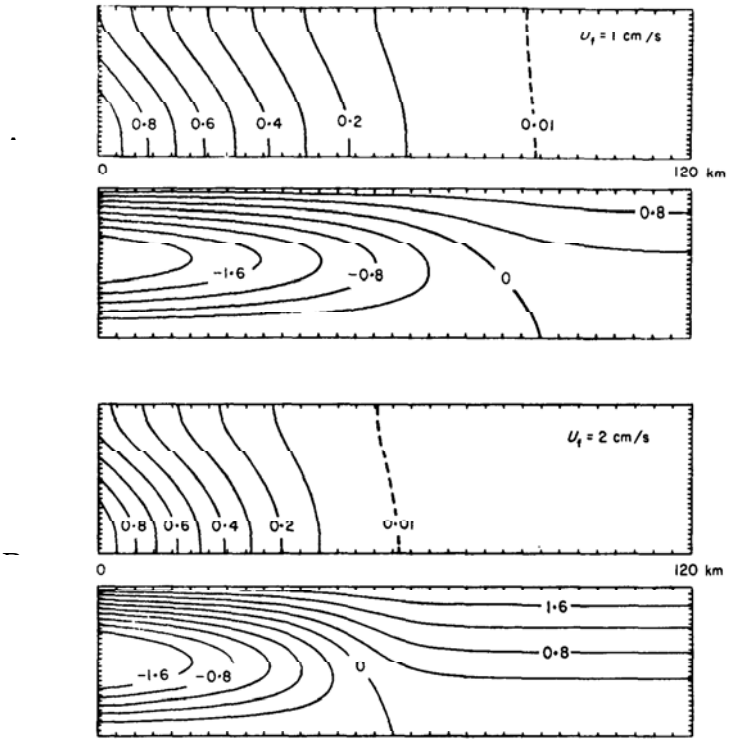

Figure 1.2. Salinity and stream-function fields as a function of river flow U_f. Salinity fields are contoured from 0 to 1 in intervals of 0.1. The stream-function fields are scaled by 10^3 and contoured from 0 in intervals of 0.4 (Festa and Hansen 1976).

a

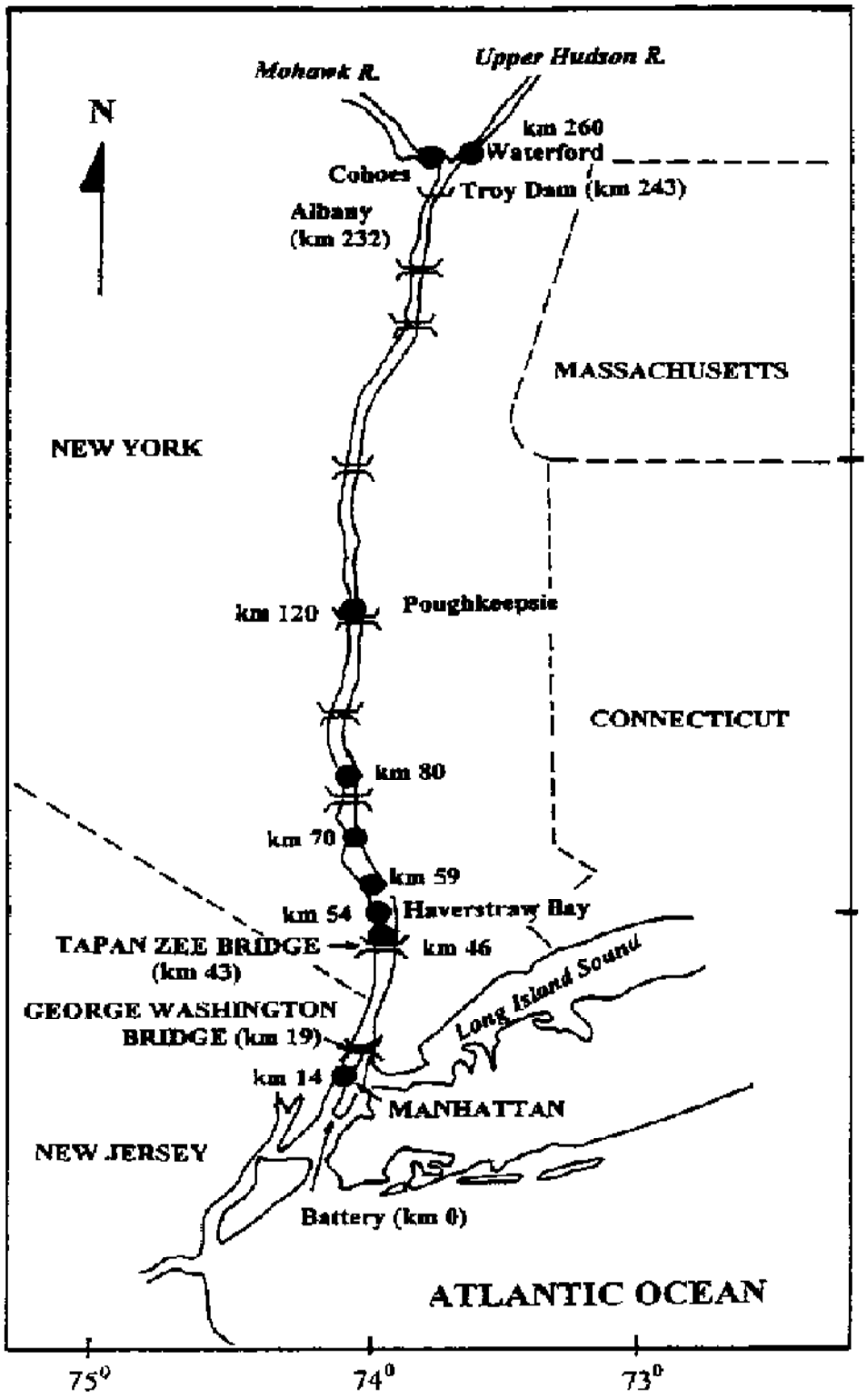
Mohawk R.
Upper Hudson R.
N
km 260
Waterford
Cohoes
Troy Dam (km 243)
Albany
(km 232)
MASSACHUSETTS
NEW YORK
km 120
Poughkeepsie
CONNECTICUT
km 80
km 70
km 59
km 54
Haverstraw Bay
TAPAN ZEE BRIDGE
(km 43)
km 46
GEORGE WASHINGTON
BRIDGE (km 19)
Long Island Sound
km 14
MANHATTAN
NEW JERSEY
Battery (km 0)
ATLANTIC OCEAN
75°
74°
73°

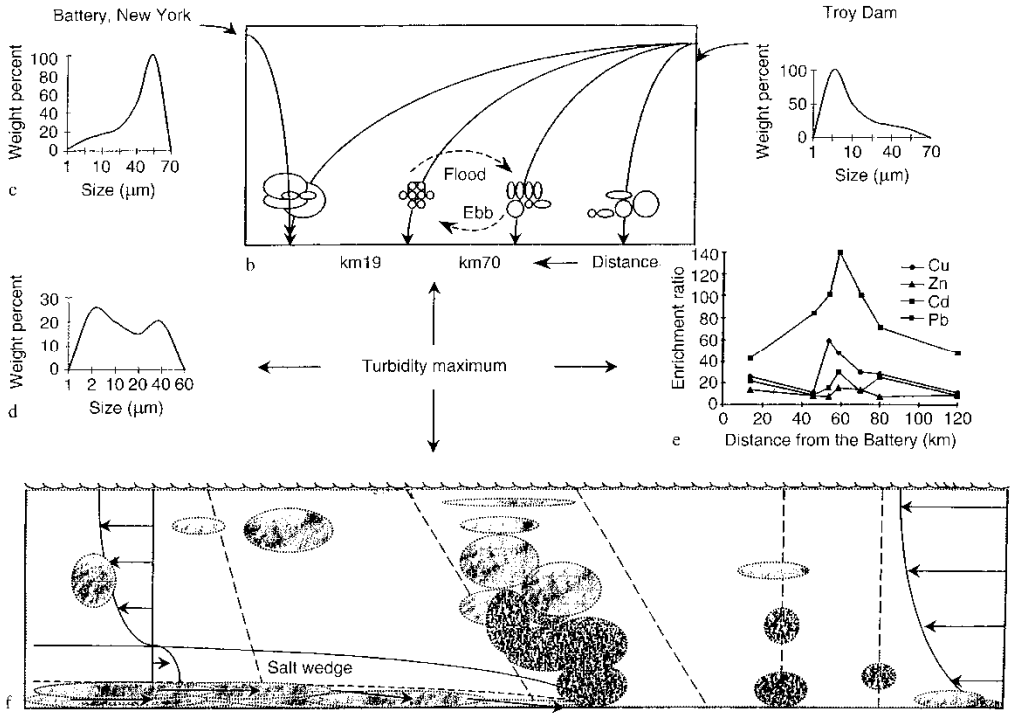

Figure 1.3 (**a**) Map of the Hudson River and sampling sites with distances (km) from the Battery, New York. Schematic diagram showing possible dynamics of mud and metal accumulation in the Hudson River estuary turbidity maxima. (**b)** Model suggesting the flood-ebb cycle of sediments. (**c)** Particle-size distribution, the Battery, New York. (**d)** Particle-size distribution, the Haverstraw Bay. (**e)** Heavy metal accumulation in the Haverstraw Bay. (**f)** Model showing aggregation/disaggregation cycles in the turbidity maximum at the fresh/saltwater interface (Menon, Gibbs et al. 1998).

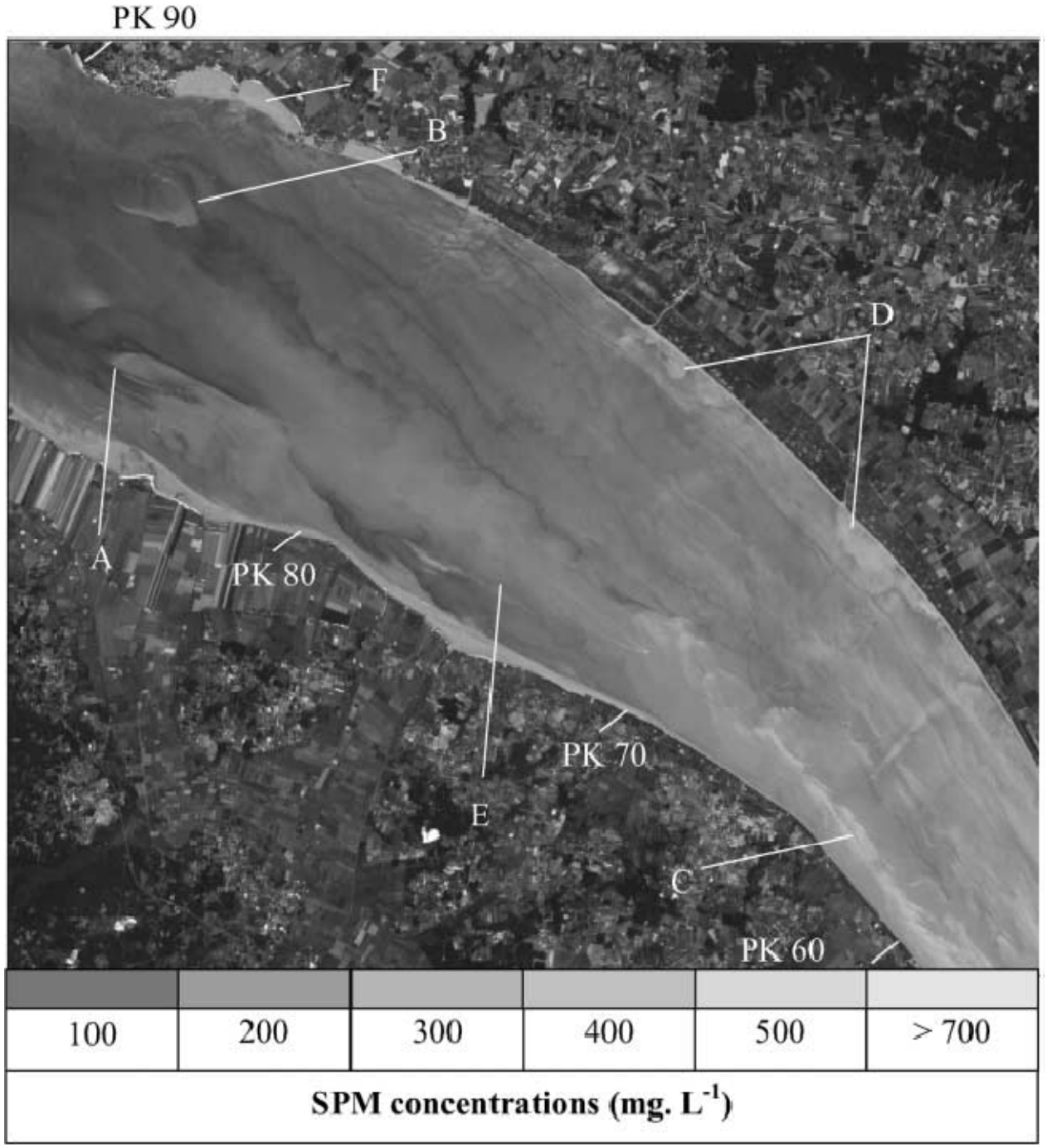

Figure 1.4. SPOT-XS image (@CNES 14/07/96, 11:23 TU) of the downstream part of the Gironde estuary. The SPM concentrations were calculated from relationship presented in (Doxaran, Froidefond et al. 2002).

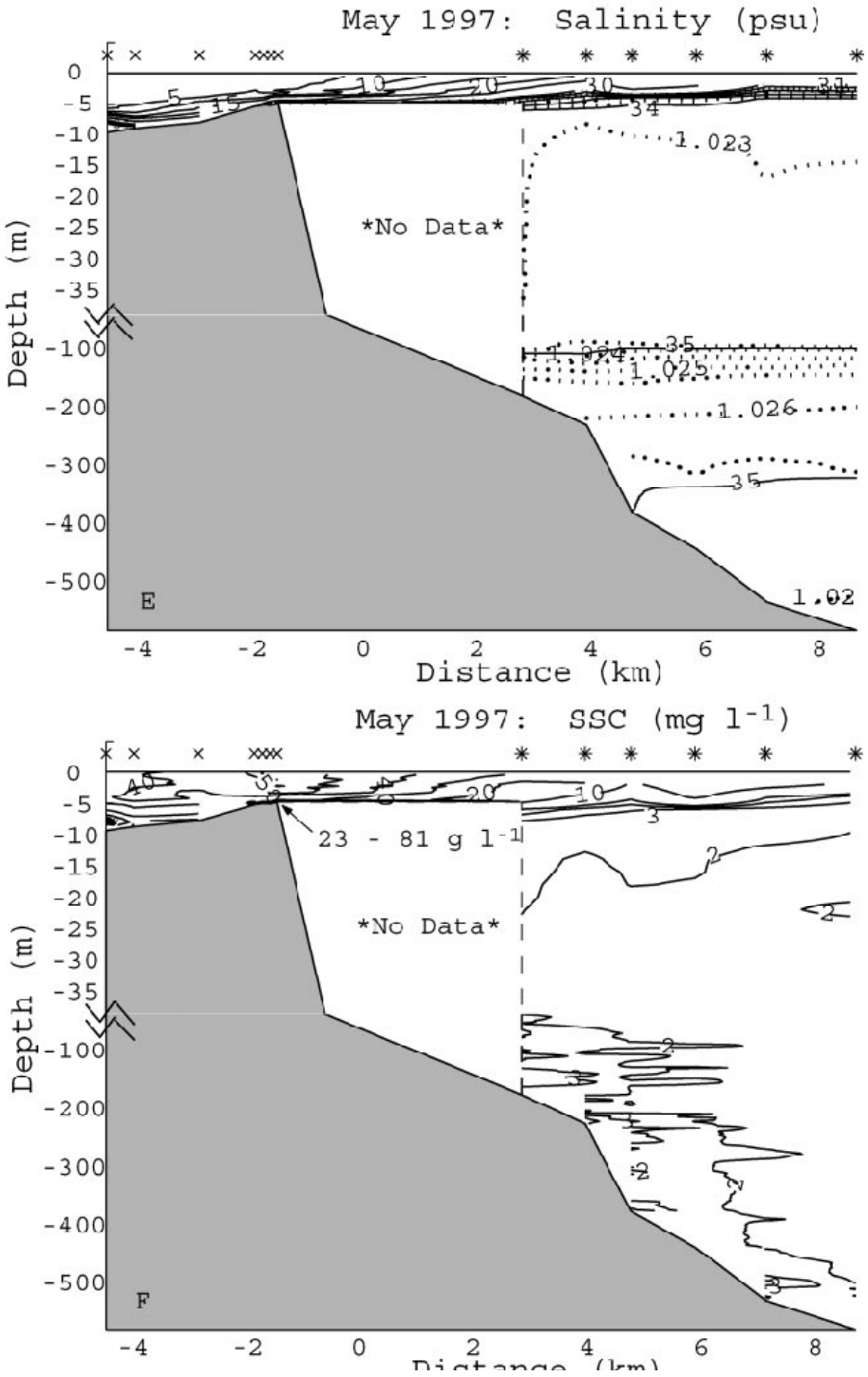

Figure 1.5. Cross-shelf transects of salinity and suspended sediment concentration (SSC) (B) during a period of low discharge, May 1997 from approximately 5 km up the Sepik River to 9 km seaward of the river mouth. Zero km is referenced to the 100m isobath at the river mouth. Density in g cmÿ3 is added to emphasize structure deep in the water column (Kineke, Woolfe et al. 2000).

2 Approach

The general methods discussed in this report have been utilized in other studies, but the manner in which they are applied to estuaries has required some modification of their more traditional uses. There are three general components used in these studies: (1) observations and databases from other models (e.g., atmospheric forcing); (2) numerical models of physical processes; and (3) integration, which is the coupling of data and models to produce a numerical system for the problem of interest.

2.1 Observations and Modeled Oceanographic Databases

The use of observations in earlier coastal studies at NRL was restricted to model validation. Observations are also useful in characterizing the overall behavior of an area, such as the tidal circulation and local water depth. These data are useful in determining the kind of model to apply to the area. The observations used in these estuarine/shelf studies are typically limited in spatial and temporal extent. They are thus most useful for validating a model for specific processes that will indicate its performance on related problems (Keen 2002).

It has proven necessary to rely on published observations for most of the examples discussed in this report. For example, the circulation study of the Atchafalaya Bay system used published hydrodynamic and hydrographic data from previous studies (Walker and Hammack 2000). The study of circulation in San Francisco Bay used observations available on-line (http://sfbay.wr.usgs.gov/access/wqdata/webbib.html) as well as in a publicly released report (Battelle, ENTRIX et al. 2002). Studies within Mississippi Sound and St. Louis Bay used previously published hydrographic and model data (Keen 2002), and tidal data from the National Oceanic and Atmospheric Administration (NOAA). The range of data sources used for these areas indicates the disparate approach to data use required in these nearshore studies.

Hydrodynamic data are available from the archive of global and regional model runs at NRL. These include the NCOM results for ocean circulation (Barron, Smedstad et al. 2004). The 1/8° global results were used for San Francisco Bay, Mississippi Sound/St. Louis Bay (Keen and Harding 2008), the Atchafalaya Bay system (Cobb, Keen et al. 2008), and Patos Lagoon, Brazil. The model current fields used in the Papua New Guinea study (Keen, Ko et al. 2006) were extracted from the East Asia Seas Nowcast/Forecast system (http://www7320.nrlssc.navy.mil/EAS16_NFS/). These currents were used to drive a Lagrangian particle model, and for boundary conditions to a higher-resolution model of the Gulf of Papua (Slingerland, Selover et al. 2008). The numerical models discussed in this report

also require atmospheric forcing and wave forecasts. NOGAPS and COAMPS atmospheric fields were used.

2.2 Numerical Models

This report discusses simulations of inner shelf and shoreface hydrodynamics and mass transport. The models that have been used are the Princeton Ocean Model (POM), the Estuarine and Coastal Ocean Model (ECOM), the Navy Coastal Ocean Model (NCOM), the Simulating Waves Nearshore (SWAN) wave model, the Littoral Sedimentation and Optics Model (LSOM), and the HydroQual Contaminant Model (HQCM). Each model will be briefly described in this section with respect to the features that helped determine its use.

Several of the studies discussed in this report were started before the NCOM circulation model became available. The first circulation model to be applied to this problem was POM, which is still in use (Aoki and Isobe 2006). POM uses split modes; the external (fast) mode is solved explicitly with a small time step whereas the internal (slow) modes are solved using a much larger time step. It has a free surface and uses sigma-coordinates for the vertical axis. It has proven robust but has some instability problems in shallow water because of the explicit solution for the water surface. ECOM was used for one example and the results will be compared to POM in this report. It is very similar to POM but the version used herein also incorporates equations for suspended sediment and dissolved substances (tracers). Neither of these models had a multi-processor capability, which can be a significant detriment for longer simulations. Both were used before the global archives of circulation were available; thus they were used with open boundaries that used a no-gradient condition for salinity and temperature, and surface elevations from either a regional tidal model (Martin, Smith et al. 2009) or a numerical model (Leuttich, Westerink et al. 1992). River data were generally unavailable and were not utilized with these models in this work.

NCOM replaced POM and ECOM when it became available because of its improved numerical scheme, which permitted multiple processor use on desktop computers. NCOM is slightly different from POM in that it does not use a split mode; however, it incorporates an implicit solver for the free surface. This greatly increases its ease of use for estuaries under most conditions. NCOM can be nested to a coarse-grid model to supply boundary conditions at the open boundary of the domain. All of the NCOM simulations discussed herein utilized open boundaries from outer nests as well as climatological monthly river inflow. Open boundary conditions for NCOM comprise water levels and vertically integrated transports that consist of separate subtidal and tidal flows, and profiles of temperature, salinity, and currents. A radiation boundary condition is used for momentum, heat, and mass at open boundaries. Rivers are represented by specifying transport, temperature, and salinity at inflow grid cells. Specific boundary conditions for the simulations presented in this paper are discussed in the following sections.

The surface boundary condition for the hydrodynamic simulations consisted of wind speed and direction from coastal observations, offshore buoys, the Coupled Ocean-Atmosphere Prediction System (COAMPS), or interpolated from the 1° Navy Global Operational Atmospheric Prediction System (NOGAPS) forecast fields. A flux was used for the surface boundary condition for salinity in San Francisco Bay.

The SWAN model was designed for application to shallow water regions. Input consists of bathymetry, water level changes, and wind fields. The model can also accept deep-water wave forcing at the open boundary. It calculates refraction, wave breaking, dissipation, wave-wave interaction, and local wind generation. The model does not compute diffraction and it should not be used when wave heights are expected to vary over a few wavelengths. Thus, the wave field is not generally accurate within the immediate vicinity of obstacles. Dissipation of wave energy is computed for white-capping, bottom friction, and depth-induced wave breaking.

HQCM is derived directly from the ECOMSED model (Anonymous 1998). It consists of the full equations for solving tracer, wave, particle, and suspended sediments for external forcing (i.e., from files). This model was developed in order to have these capabilities without the additional burden of the hydrodynamic code, which was no longer used at NRL. There has been no validation work prior to this report, which will attempt to qualify its performance for tracer calculations. HQCM was used only in studies that also utilized NCOM, which supplies horizontal and vertical momentum fluxes and mixing coefficients.

Communication between models has been primarily with NetCDF files. An exception was the use of a CORBA (Common Object Request Broker Architecture) model coupling framework (Allard, Wallcraft et al. 2003).

3 Wind and tidal circulation in the Mullica-Great Bay Estuary, New Jersey

Great Bay (GB) is a bar-built estuary (lagoon) located on the Atlantic coastal plain ~13 km north of Atlantic City (Fig. 3.1). It is fed by the Mullica River, with a mean monthly summer discharge of ~1.5 m^3/s and a mean winter discharge of ~6 m^3/s. A record discharge of 51 m^3/s occurred in July 2007. Great Bay averages 1.5 m in depth and has extensive aquatic vegetation. The Mullica-Great Bay Estuary (MGBE) contains large intertidal sand and mud flats (Able, Lathrop et al. 1996) but the Mullica River has a small sediment load because its watershed consists of pine barrens (Coonley, Baker et al. 1971). The estuary connects to the Atlantic Ocean through Little Egg Inlet (LEI), which is partially blocked by islands that separate Great Bay from Little Egg Harbor (LEH) to the north. The flood tide has formed multiple lobed deltas in both water bodies with some lobes terminating in small islands and shoals. The bottom sediment consists of silt near the Great Bay delta (see Fig. 3.1) and clay to the north except near the barrier island (R. Stavn, unpublished data). The tides at Atlantic City are semidiurnal with a mean range of ~6 feet (<2 m) (Fig. 3.2). The tides may be larger in Great Bay but no observations are available. This location is of interest because it is a national wildlife refuge, and the LEO-15 (Long-Term Environmental Observatory 15 m) observation site is located ~5 km SE of LEI.

3.1 Forecasts of estuarine circulation in July, 2000

These simulations were run in real time with a series of shell scripts that processed the atmospheric forcing into files for POM, ECOM, and LSOM. The 48-hr forecasts were started every 12 to 24 hr. The COAMPS winds were unavailable, however, between 20 and 25 July and forecasts were not run. The models did not use restart files but the tidal circulation was ramped up over 48 hours prior to each forecast. The simulations of circulation, waves, and sedimentation in GB were completed before river data were accessible. No hydrographic data were available either and constant values of 20° C and 35 psu were used, respectively, for temperature and salinity. This is a reasonable assumption given the weak inflow from Mullica River and the shallow depths within the estuary. The flow is very likely barotropic for much of the time during the summer.

Available bathymetry data were merged to form a grid with 43×56 m cells (x and y). The grid extends offshore as far as the 20 m isobath (Fig. 3.3). The water column was discretized with 6 sigma levels. The numerical models were forced with winds from different sources. Preliminary runs with POM (cell size ≈100 m) used COAMPS wind fields on a ~1/5° (18 km) grid, which permitted only one grid point for the model domain. The COAMPS wind forcing for the model domain consisted of forecasts at 6-hr intervals. The wind speed varied substantially between forecasts at times as indicated by the different lines in Fig. 3.4. Note that each successive forecast begins 6 hrs after the preceding one. The dash line shows the measured wind speed and direction at buoy 44009 (~130 km to the south), which is the nearest buoy to MGBE. Note the

gap in the measured wind at JD 211 when no data were available. The COAMPS forecasts are qualitatively similar to the buoy but display more variability and have time differences as great as 24 hr. They also have significant speed errors as in the JD 201 forecast (red line in Fig. 3.4), which predicted a wind speed of 24 m/s at 24 hr (JD 202.0) when the measured wind was < 10 m/s. The directions from COAMPS (Fig. 3.4b) had slightly larger errors than the wind speed because of fluctuations between forecasts. Part of these discrepancies arises from the location of the buoy 130 km from the grid point from COAMPS used for the simulations.

Although similar in magnitude to Hurricane Alberto, which passed to the east of the area in August, the wind event between JD 201 and JD 203 was not associated with a tropical cyclone. The wind rotated CCW from westerly to southerly, with a maximum SSW wind at JD 202.5. This wind event was not consistently predicted by the COAMPS forecasts; e.g., the JD 201 forecast (red line) predicts a wind speed of more than twice the observations whereas the JD 202 forecast (black line with ellipses) was reasonable. The wind direction was within ~50° in all of the forecasts. This meteorological event was selected to evaluate the circulation pattern for a southerly wind because of the consistent forecast wind speed and direction.

The excessive winds predicted by the JD 201 forecast generated instabilities in POM and the simulation did not finish. Although the JD 202 forecast matches the wind record better, it is too close to the event for the estuary circulation to be fully developed; therefore, we will examine the currents (FC0007191200) predicted using the JD 201.5 forecast (black line with pluses in Fig. 3.4). The sea surface anomaly predicted by POM for this hindcast ranged from a high of 1.64 m (5.4 ft) to a minimum of -0.76 m (-2.5 ft). The model did not permit drying of wet grid cells but this lower level would have reduced local water depth to 75 cm because a minimum depth of 1.5 m was used. The tides near LEI ranged from -0.3 m (-1 ft) to 1.1 m (3.6 ft) for a tidal range of 4.6 ft, which is very similar to the tides at Atlantic City (Fig. 3.2).

The wind steadily strengthened over the MGBE during 18 July and reached 5 m/s as the simulation began. The bay circulation during the following tidal cycle (Figs. 3.5A-F) shows minimal response to this SW wind, however. Flood-tide currents exceed 1 m/s in LEI and somewhat less in the main channel of LEH. The flow weakens rapidly within the shallow estuary and the mean circulation is < 10 cm/s. Multiple eddies develop within the upper parts of the bay during high water (Fig. 3.5B) and on the shelf during low water (Fig. 3.5D). A weak alongshelf flow with a NW heading also developed at this time. The tides within the estuary were relatively unaffected by the wind for the next 12 hr as the wind decreased to 2 m/s (Figs. 3.5G, H). The wind's influence becomes more noticeable during the next tidal cycle (Figs. 3.5I – N) as the wind speed increased to 10 m/s. The high-water eddies have not developed in the upper bay (Figs. 3.5J, N), nor have the low-water eddies at LEI (Figs. 3.5K, M). The flow regime is impacted by July 21 when the inflow along the southern coast of GB is reduced (Fig. 3.5M) and the flow within LEH is disrupted. The low-water at ~0900 UT on 21 July indicates greater outflow than previously (compare Figs. 3.5P, L). This is partly due to the slight shift in

the low-water timing because the tide is not exactly diurnal. Finally, the following flood tide is weaker, partly because it is opposed by the eastward wind (Fig. 3.5Q).

3.2 Hindcasts of the MGBE circulation in November, 1999

The fall is the beginning of the northeaster season, when extratropical cyclones pass over the east coast of the US and strong NE winds persist for days (Keen and Glenn 1995). These storms could modify the flow within the MGBE with respect to exchange between the estuary and the Atlantic Ocean. The results from the forecasts presented in Fig. 3.5 indicate that the flow simulations could be improved as well. A series of hindcasts were completed using both POM and ECOM. The POM simulation used the wind data from buoy 44009 (Figs. 3.6A, B) whereas the ECOM hindcasts used buoy 44011 (Figs. 3.6C, D). Comparing these two buoys shows the large scale of atmospheric flow in the NW Atlantic. The SWAN wave model was also run on the 50 m grid using the observations from buoy 44009.

The first hindcast used the 100 m grid with the ECOM circulation model. The interval 16-19 Nov. 1999 (JD 320-323) was simulated with tides as for the POM forecasts. The WSW wind (shown as a vector on Figs. 3.7A, B) recorded a speed of 6.5 m/s. The circulation from ECOM (Figs. 3.7A, B) shows a strong response to the wind as well as baroclinic effects, despite the uniform initial salinity and temperature. The surface currents (Fig. 3.7A) reveal a CCW rotation around GB with a weak central flow 90° to the left of the wind; this snapshot is from the early flood tide. Flow into LEI is uniform at ~60 cm/s. The bottom currents (Fig. 3.7B) are aligned with surface flow in the channels and along the north shore of GB, but they are weaker. The bottom flow is ~45° to the west of the surface flow in northern GB. The bottom flow is >90° left of the surface currents in LEH.

November 18-21 was simulated with ECOM having no tides in order to examine the effects of moderate winds in this shallow environment where the tidal signal can dominate the circulation. Without the tide masking the wind setup, it can be seen that water is piling up in the upper bay and harbor in response to a SE wind (Fig. 3.7C). The wind-driven surface currents (Fig. 3.7D) are much weaker than the tidal currents from the previous hindcast. The surface flow is aligned with the wind away from shorelines and several eddies have developed along the lee shore of LEH. A larger eddy is present just inside LEI. Note that flow on the shelf is artificial because of the closed boundary although the NE flow south of LEI is probably reasonable.

A higher resolution grid was used to examine the impact of cell size on fine structure within the MGBE. The simulations with POM on the 50-m grid used the winds recorded at buoy 44009 (Figs. 3.6A, B). The circulation will be discussed with respect to specific features. The increased resolution reveals that the tide does not enter GB and LEH simultaneously. The tidal wave first enters GB before LEH (Fig. 3.8A). When both bodies reach high tide (Fig. 3.8B), eddies form within GB and on the shelf outside LEI. A subsequent strengthening of the SE wind during the ebb tide does not reduce the flow through LEI (Fig. 3.8C). During the low tide

at JD 322.92 (Fig. 3.8D), the wind-driven flow visibly bifurcates around the islands in the southern LEH as well as the northern GB. The offshore flow on the shelf should also induce upwelling. Eddies again develop during low water in GB and near the entrance to LEI (Fig. 3.8E). The southerly wind on JD 323.21 (Fig. 3.8F) occurs immediately after high water and eddies are present along the southern shore and west of the northern islands within GB. The weak southerly wind again has no substantial impact on the ebb tide through the main channels of LEH and GB (Fig. 3.8G). Propagation of the subsequent flood tide into MBGE as a coherent wave (Fig. 3.9H) was similar to the ebb tide (Fig. 3.8C). The impact of the weak southerly wind is seen as the next high tide does not produce eddies along the lee shore of LEH (Fig. 3.8I). There may some wind effects as well that contribute to SSH being ~20 cm lower there than elsewhere.

The hindcast wave field developed in response to the SE wind and wave heights exceeded 50 cm in large portions of the MGBE by 2200 UT on 19 Nov. (Fig. 3.9A). The persistent wind with large fetch over the North Atlantic also resulted in wave periods > 6 s in LEI and the deeper water in the tidal channels. It is unlikely that the low periods inside GB (< 3 s) would entrain the cohesive sediment there, which would have been consolidating for some time. However, the long periods in LEI should entrain the fine sand and silt that composes the bottom there. This was investigated using LSOM as before.

3.3 Sediment resuspension in Little Egg Inlet

Sediment input to the MGBE is minimal and resuspension by waves is probably not significant in the summer. Thus, the sedimentation modeling for July 2000 in the MGBE focused on entrainment by the strong tidal currents through LEI only (GB02-Jul2000). These forecasts were completed as part of the original forecasts. The model grid used by LSOM (TRANS98) was the 100 m grid used by POM. The steady flow field was supplied by the currents from POM at 1 m below the surface. The results for 19 July 2000 are shown in Fig. 3.10. The model domain for sedimentation is indicated by the white box in Fig. 3.3. The model used a uniform bottom sediment of very fine sand with a D_{50} = 4.5ϕ (0.04 mm) and a critical shear velocity = 2.5 cm/s (0.67 Pa). At 1300 UT the tide was inbound with a maximum velocity of 90 cm/s within LEI (Fig. 3.10A, top row) and u_* was between 2 and 3 cm/s in the inlet (middle row). The resulting total suspended load (TSS) predicted by LSOM was 1600 g/m^2 at this time in water depths of 2-3 m. The flood tide was nearing high water at 1600 UT (Fig. 3.10B) and the currents remain high only near the northern shore of LEI. Consequently, TSS reached only ~10 g/m^2 in isolated places. Seaward flow during the ebb tide at 1900 UT reached 110 cm/s in the inlet (Fig. 3.10C) and u_* exceeded 4 cm/s in a broad swath across the inlet. The resulting TSS exceeded 2000 g/m^2 on the north side and in the center of LEI. At the end of the simulation (0000 UT on July 20), the flood tide was beginning and had reached 45 cm/s (Fig. 3.10D) but u_* was < 2 cm/s and TSS was negligible.

The fall sedimentation regime in LEI was examined using LSOM simulations for 18-19 November 1999 on the 100-m grid (black box in Fig. 3.3) on a slightly larger domain than was used for the July 2000 simulations. This simulation used the waves from SWAN and tides (Fig. 3.9). The steady flow field was sub-sampled from the barotropic currents computed by POM on the 50-m grid. Three snapshots on 19 Nov. (Fig. 3.11) show the influence of the strengthening wave field throughout the day. The waves had not built yet at 0200 UT and maximum u_{*cw} values of < 6 cm/s were restricted to the southern shore of LEI (middle row of Fig. 3.11A). The resulting TSS (lower row) was also limited to this shore and was less than 200 g/m^2. The currents were very similar during the next flood tide (upper row in Fig. 3.11B) but the increasing waves produced a broader distribution of bottom shear stress in LEI and the TSS maximum has exceeded 700 g/m^2. At 2200 UT the tides were nearing low water (Fig. 3.11C) while the bed u_{*cw} field expanded within the LEI, with a peak magnitude of 7 cm/s. The calculated TSS has now reached 1100 g/m^2 in mid-channel with values greater than 200 g/m^2 on the northern shore of the inlet.

The summer and fall sedimentation simulations are not directly comparable because of differences in hydrodynamic forcing. The July 2000 forecasts neglected waves and used near-surface currents to drive the resuspension model. This was done because it has been found that the near-bottom flow from the primitive-equation models like POM and ECOM tends to be low due to bottom friction and vertical mixing. Another approach to this problem is to use arbitrary entrainment criteria for the bottom sediment–neither method is ideal but they are necessary to improve the realism (accuracy) of the resuspension result. The use of barotropic currents in the Nov. 1999 simulation is a somewhat more realistic assumption since they are closer to the bed, especially in the tidal inlet. This different elevation for the forcing fields explains the discrepancy in TSS for summer and fall. Overall, the Nov. result is more realistic because it includes waves. These compromises are justified, however, in light of the resulting TSS fields, which show consistent results based on predicted hydrodynamics.

The numerical models have helped elucidate the movement of sand along the New Jersey coast in this area, and they partially explain the origin of the flood deltas within the MGBE. Although the ebb tide is slightly stronger, there is very little sediment being transported from the estuary because of the low sediment load. Any sediment that is transported through LEI will be reworked by the dominant NE swell (Hayes and Nairn 2004), which also reinforces transport into the estuary during the flood tide. The flood deltas (see Fig. 3.1) are maintained by the rapid decrease in flood currents beyond the confines of the inlet and tidal channels (see Fig. 3.5A). Sediment for continued flood delta growth is continuously supplied by the southward alongshore drift on Barnegat Island (Smith and Kraus 1999). Furthermore, this estuary is different from some along the Louisiana coast because inlet bypassing (Jaffe, List et al. 1997) does not appear to be common.

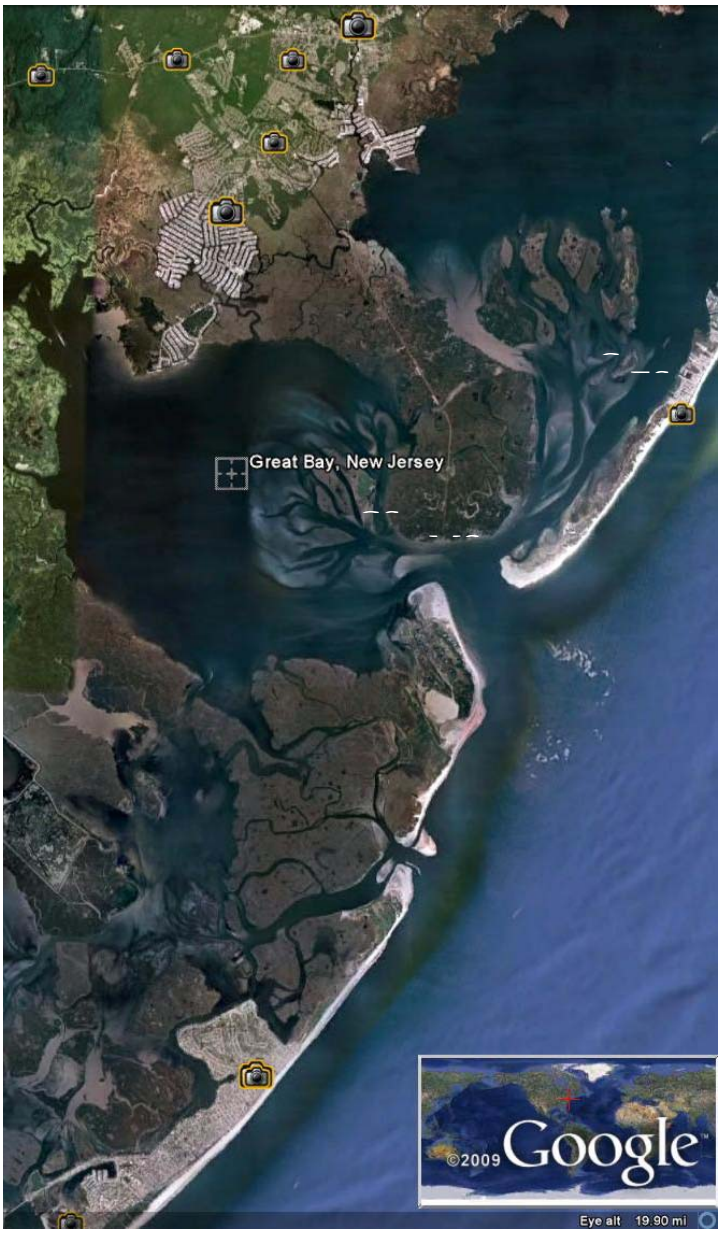

Figure 3.1. Landsat image of Great Bay, New Jersey. This image is approximately the extent of the 50 m model grid used for both POM and ECOM simulations. The letters are locations where sediment data were collected. They indicate the median grain size: (C) = clay; (FS) = fine sand; (CS) = coarse silt; (MS) = medium silt.

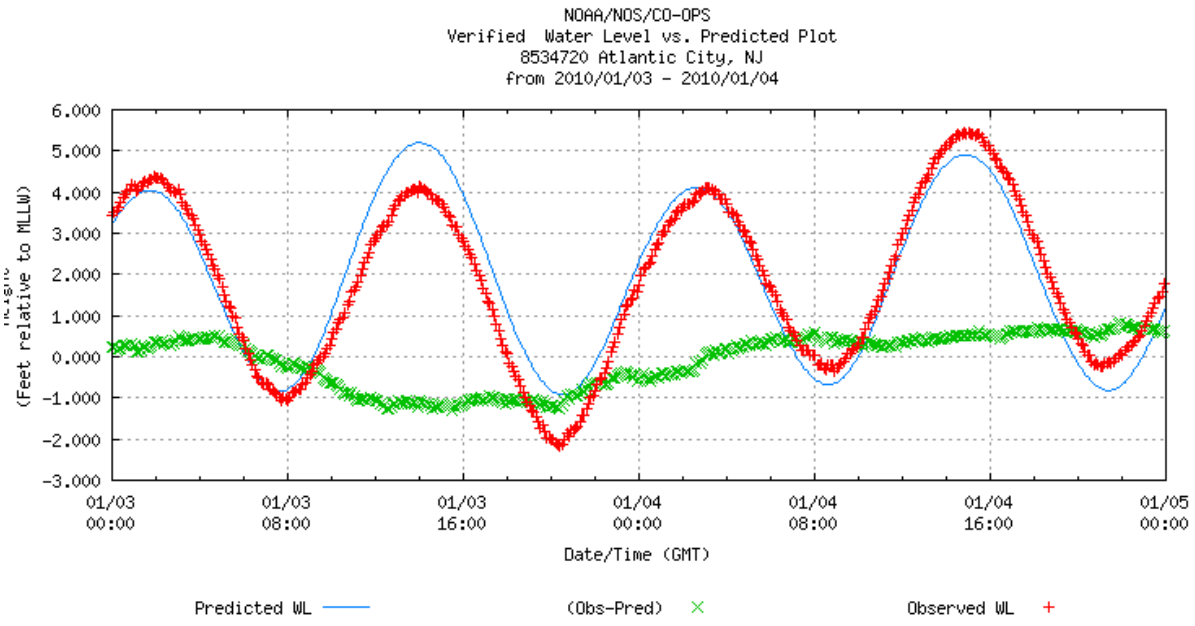

Figure 3.2. Tides at Atlantic City, New Jersey (39.355°N, 74.4183°W), for January 1-5, 2010. SOURCE: http://co-ops.nos.noaa.gov

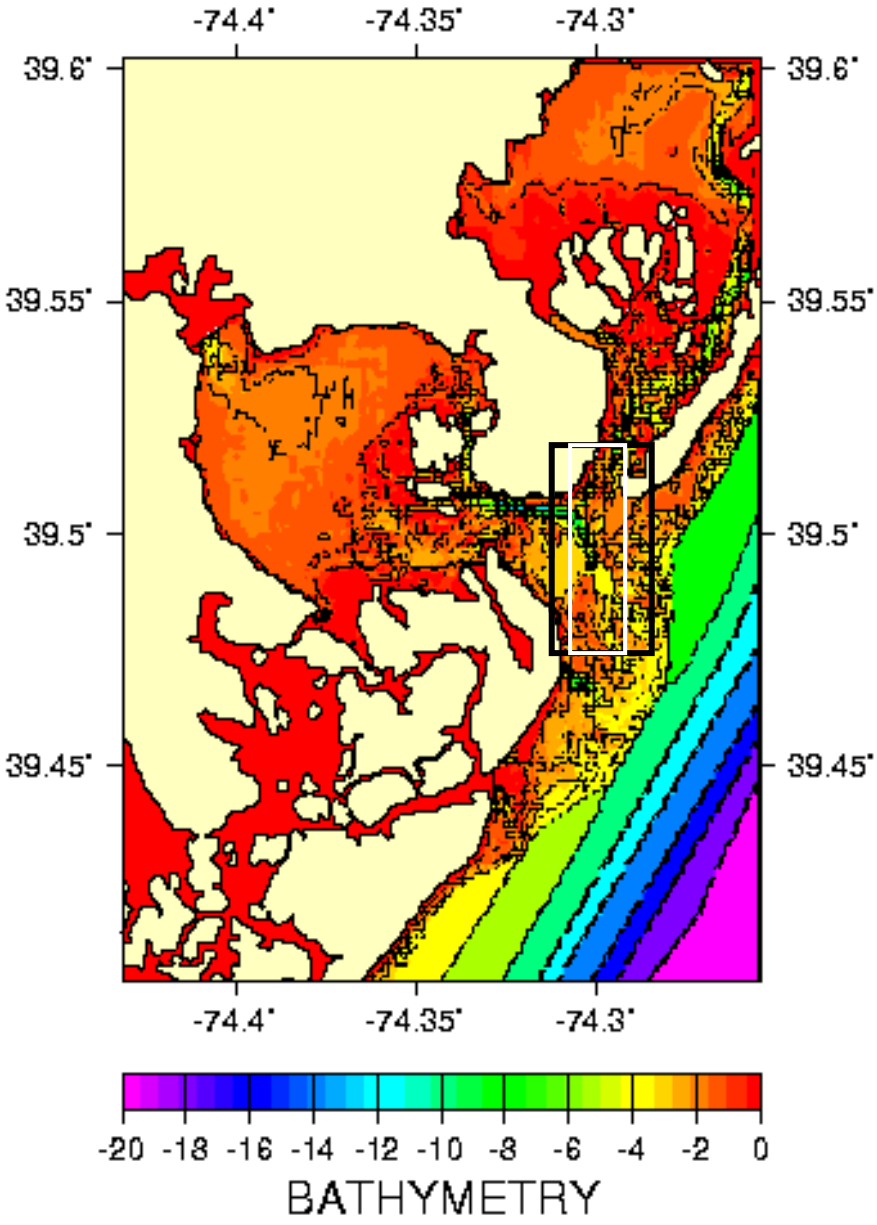

Figure 3.3. Composite bathymetry for Great Bay, New Jersey. The model grid has cells with dimensions of 43 and 56 m, respectively, for the *x* and *y* Cartesian axes. The estuary bathymetry was interpolated from NOAA charts and the offshore bathymetry was from ETOPO5. The domain used for the July, 2000, sedimentation hindcast is indicated by the white box. The November, 1999, domain is outlined with the heavy black box.

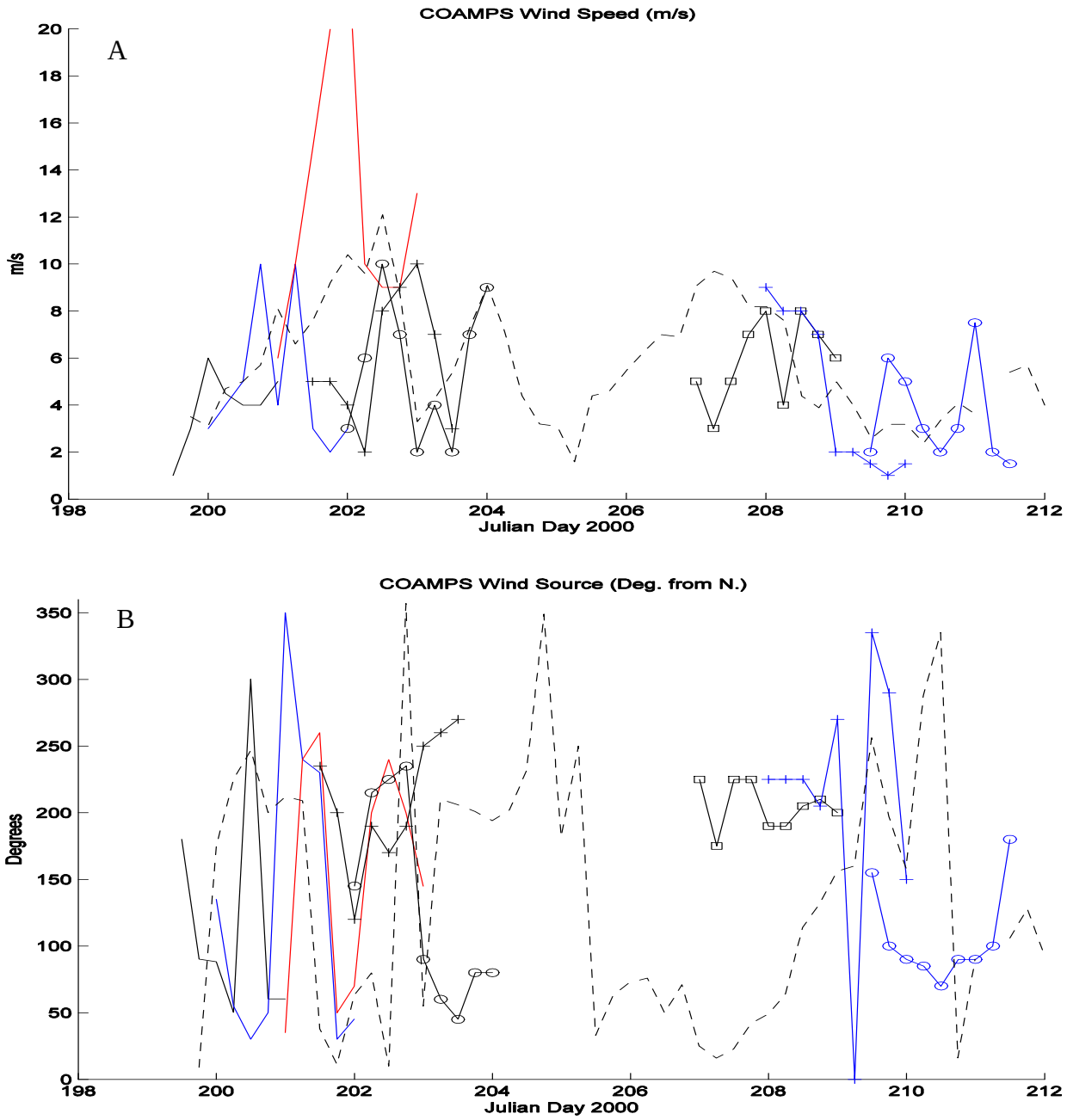

Figure 3.4. Time series of (A) wind speed and (B) direction predicted by COAMPS in July 2000 for the 100 m grid. The different color/symbol lines indicate the predictions from successive forecasts. The dashed line is the measured wind speed and direction at NDBC buoy 44009, located at 38.464 N 74.702 W. Direction is the wind source (bearing) in degrees CW from north.

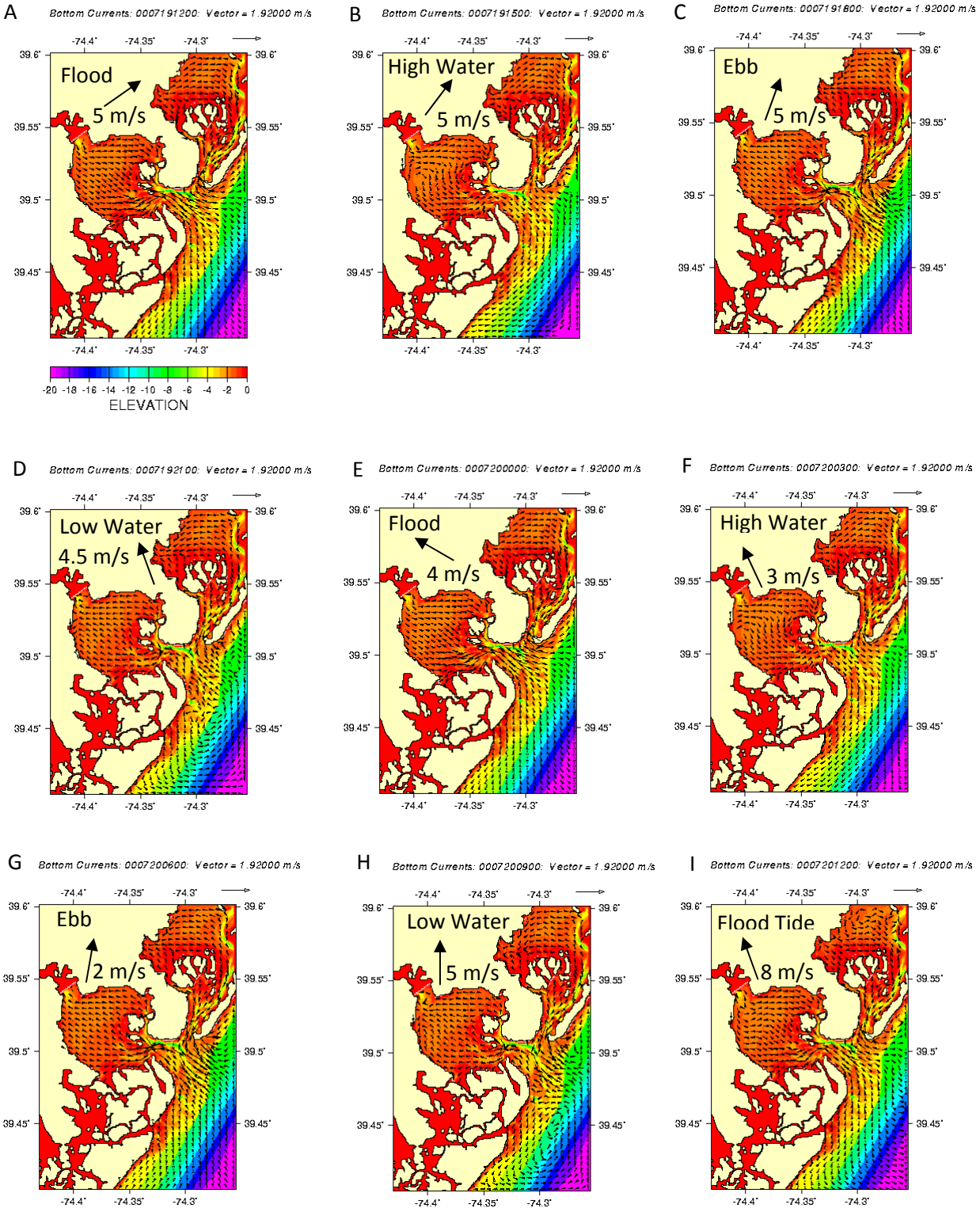
A
Bottom Currents: 00071 91200: Vector = 1.92000 m/s
Flood
5 m/s
B
Bottom Currents: 00071 91500: Vector = 1.92000 m/s
High Water
5 m/s
C
Bottom Currents: 00071 91800: Vector = 1.92000 m/s
Ebb
5 m/s
-74.4° -74.35° -74.3°
39.6° 39.55° 39.5° 39.45°
-20 -18 -16 -14 -12 -10 -8 -6 -4 -2 0
ELEVATION
D
Bottom Currents: 00071 92100: Vector = 1.92000 m/s
Low Water
4.5 m/s
E
Bottom Currents: 00072 00000: Vector = 1.92000 m/s
Flood
4 m/s
F
Bottom Currents: 00072 00300: Vector = 1.92000 m/s
High Water
3 m/s
G
Bottom Currents: 00072 00600: Vector = 1.92000 m/s
Ebb
2 m/s
H
Bottom Currents: 00072 00900: Vector = 1.92000 m/s
Low Water
5 m/s
I
Bottom Currents: 00072 01200: Vector = 1.92000 m/s
Flood Tide
8 m/s

J

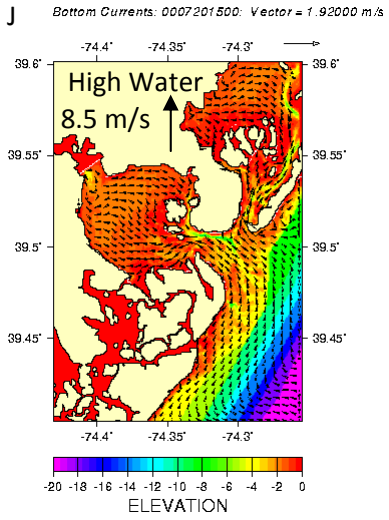
Bottom Currents: 0007201500: Vector = 1.92000 m/s
-74.4° -74.35° -74.3°
39.6° 39.55° 39.5° 39.45°
High Water
8.5 m/s
-20 -18 -16 -14 -12 -10 -8 -6 -4 -2 0
ELEVATION

K

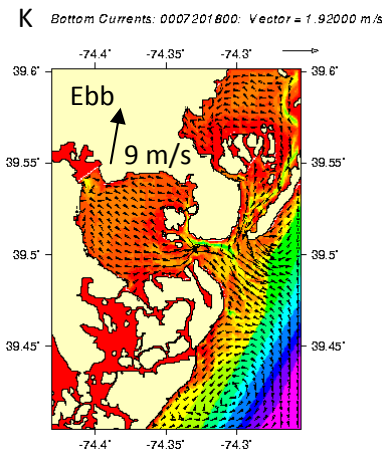
Bottom Currents: 0007201800: Vector = 1.92000 m/s
-74.4° -74.35° -74.3°
39.6° 39.55° 39.5° 39.45°
Ebb
9 m/s

L

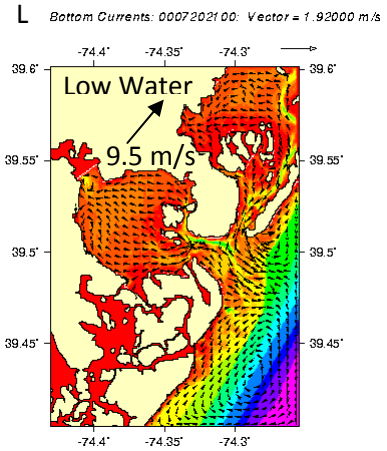
Bottom Currents: 0007202100: Vector = 1.92000 m/s
-74.4° -74.35° -74.3°
39.6° 39.55° 39.5° 39.45°
Low Water
9.5 m/s

M

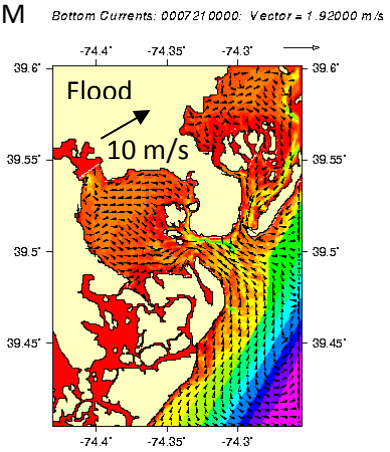
Bottom Currents: 0007210000: Vector = 1.92000 m/s
-74.4° -74.35° -74.3°
39.6° 39.55° 39.5° 39.45°
Flood
10 m/s

N

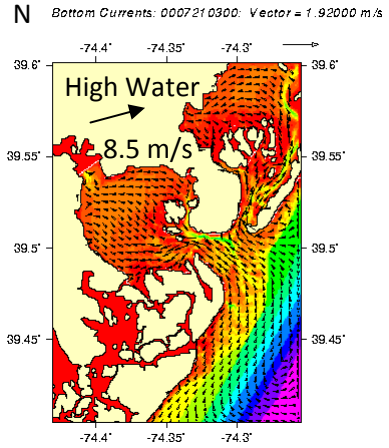
Bottom Currents: 0007210300: Vector = 1.92000 m/s
-74.4° -74.35° -74.3°
39.6° 39.55° 39.5° 39.45°
High Water
8.5 m/s

O

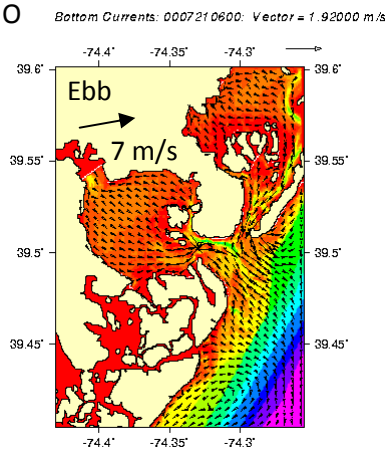
Bottom Currents: 0007210600: Vector = 1.92000 m/s
-74.4° -74.35° -74.3°
39.6° 39.55° 39.5° 39.45°
Ebb
7 m/s

P

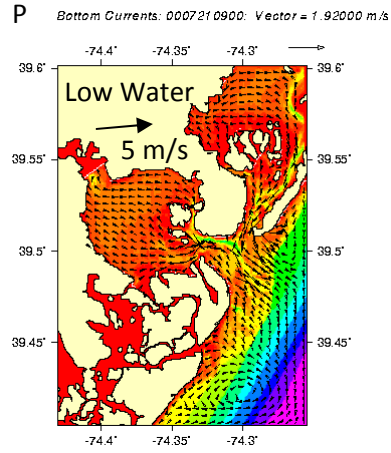
Bottom Currents: 0007210900: Vector = 1.92000 m/s
-74.4° -74.35° -74.3°
39.6° 39.55° 39.5° 39.45°
Low Water
5 m/s

Q

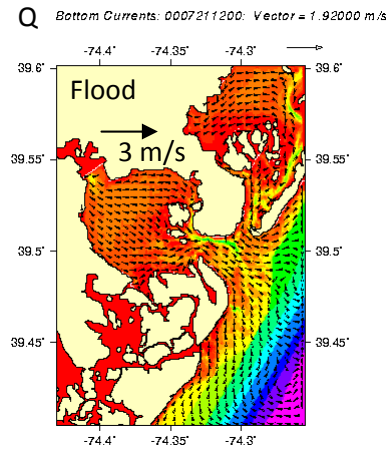
Bottom Currents: 0007211200: Vector = 1.92000 m/s
-74.4° -74.35° -74.3°
39.6° 39.55° 39.5° 39.45°
Flood
3 m/s

Figure 3.5 Sequence of bottom currents every 3 hr from POM on the 100 m grid for Great Bay, 1200 UT 19 to 21 July, 2000. The current vector arrows are 1.92 m/s in length. The tide stage is approximate because the tides are mixed. The wind direction and speed are shown on ebb and flood panels only. The depth color bar is in panels (A) and (J).

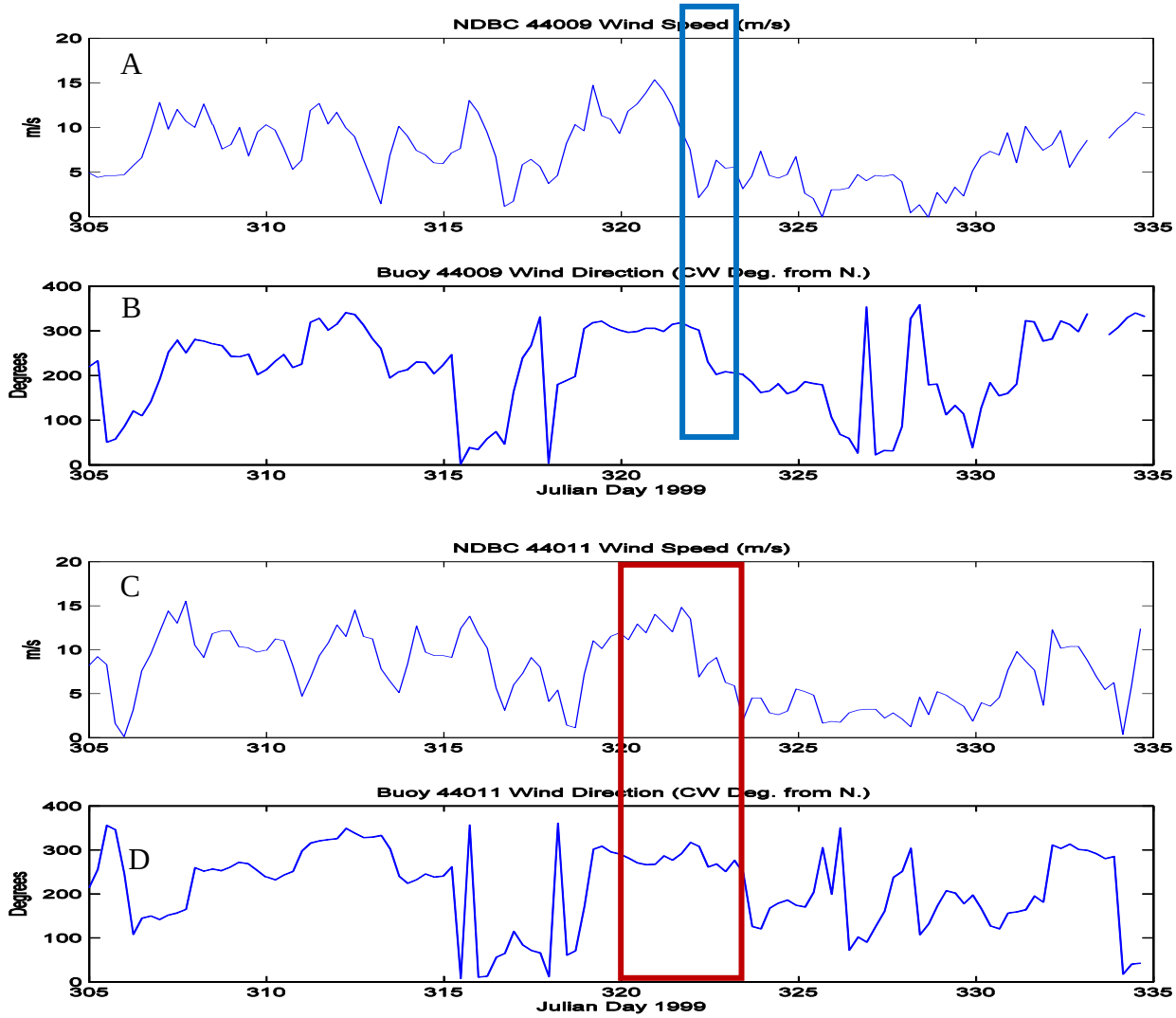

Figure 3.6. Time series of wind measured at NDBC buoy 44009 (38.464 N 74.702 W): (A) speed and (B) direction. The blue box brackets the POM 50-m grid hindcast. Time series of wind measured at NDBC buoy 44011 (41.111 N 66.58 W): (C) speed and (D) direction. The red box indicates the interval for the ECOM hindcasts. Direction is the wind source (bearing) in degrees CW from north.

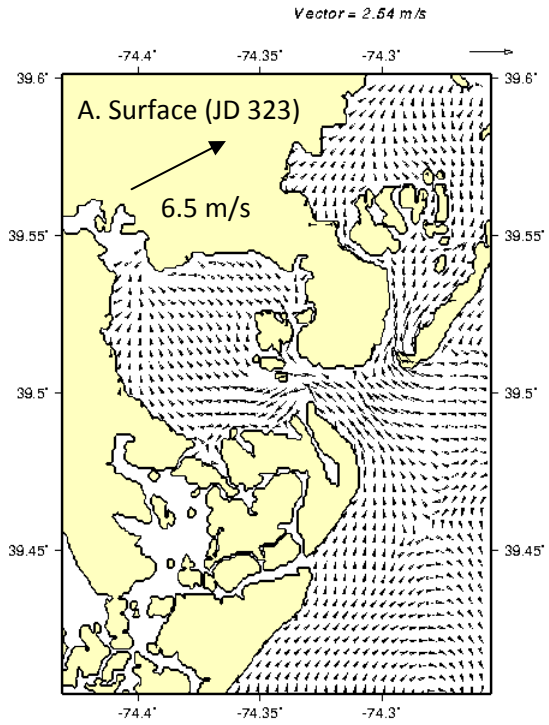
Vector = 2.54 m/s
A. Surface (JD 323)
6.5 m/s
-74.4°
-74.35°
-74.3°
39.6°
39.55°
39.5°
39.45°

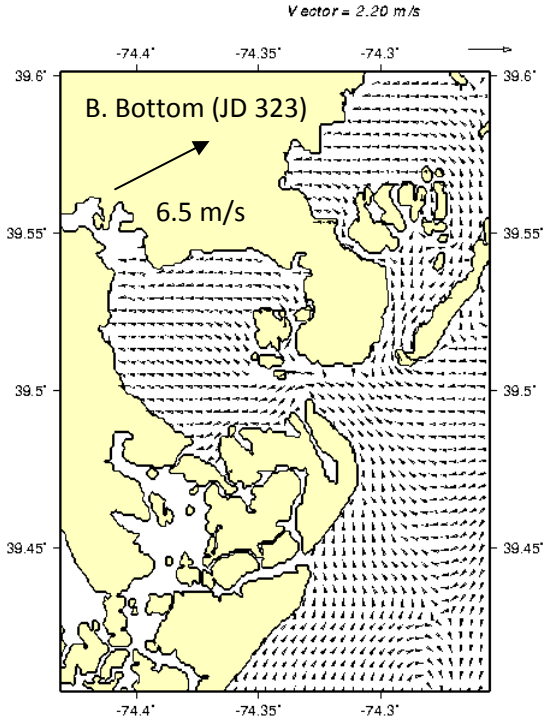
Vector = 2.20 m/s
B. Bottom (JD 323)
6.5 m/s
-74.4°
-74.35°
-74.3°
39.6°
39.55°
39.5°
39.45°

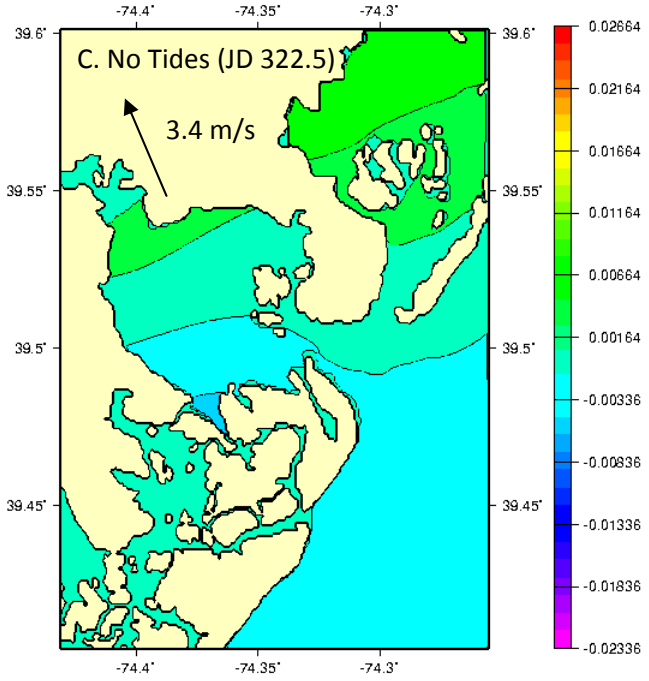
C. No Tides (JD 322.5)
3.4 m/s
0.02664
0.02164
0.01664
0.01164
0.00664
0.00164
-0.00336
-0.00836
-0.01336
-0.01836
-0.02336
-74.4°
-74.35°
-74.3°
39.6°
39.55°
39.5°
39.45°

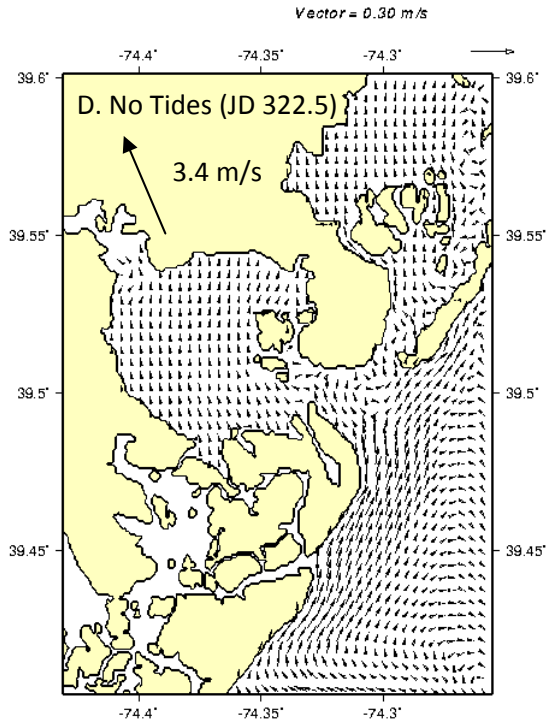
Vector = 0.30 m/s
D. No Tides (JD 322.5)
3.4 m/s
-74.4°
-74.35°
-74.3°
39.6°
39.55°
39.5°
39.45°

Figure 3.7. Output from ECOM hindcasts on the 100 m grid. Results during a flood tide at 0000 UT 19 Nov.: (A) Surface currents; (B) bottom currents. Results without tides at 1200 UT 18 Nov.: (C) Sea Surface Height (SSH); (D) Surface currents. Note that the current vector scales are different. The wind speed/direction is indicated by the large arrow.

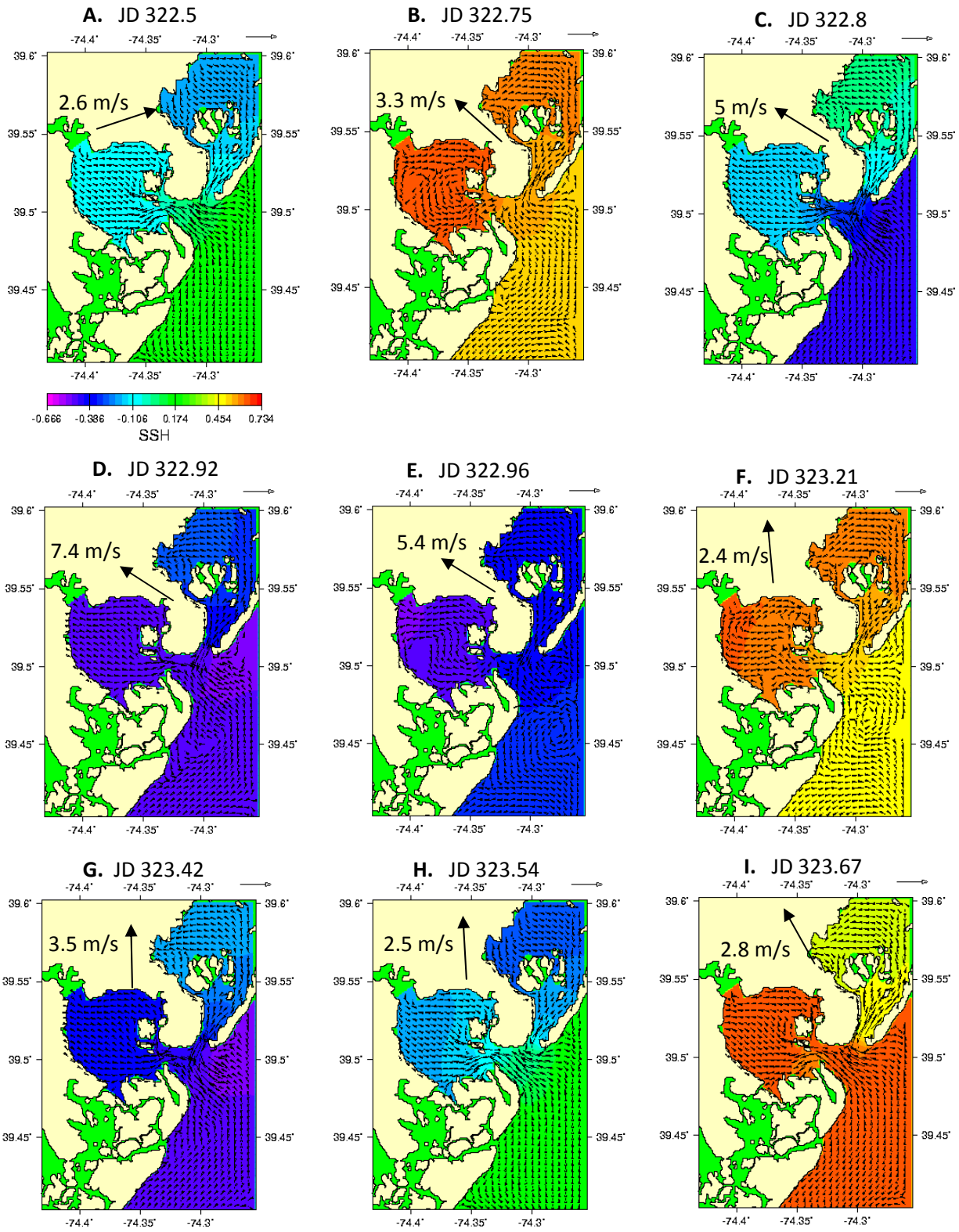
A. JD 322.5
2.6 m/s
B. JD 322.75
3.3 m/s
C. JD 322.8
5 m/s
-0.666 -0.386 -0.106 0.174 0.454 0.734
SSH
D. JD 322.92
7.4 m/s
E. JD 322.96
5.4 m/s
F. JD 323.21
2.4 m/s
G. JD 323.42
3.5 m/s
H. JD 323.54
2.5 m/s
I. JD 323.67
2.8 m/s
-74.4° -74.35° -74.3°
39.6° 39.55° 39.5° 39.45°

Figure 3.8. Barotropic currents and SSH from POM for 18-19 Nov., 1999, on the 50 m grid. (A) Nov. 18, 1200 UT; (B) Nov. 18, 1600 UT; (C) Nov. 18, 2000 UT; (D) Nov. 18, 2200 UT; (E) Nov. 18, 2300 UT; (F) Nov. 19, 0500 UT; (G) Nov. 19, 1000 UT; (H) Nov. 19, 1300 UT; (I) Nov. 19, 1600 UT. The current vector scale = 1.3 m/s. The color-bar for SSH is on panel A.

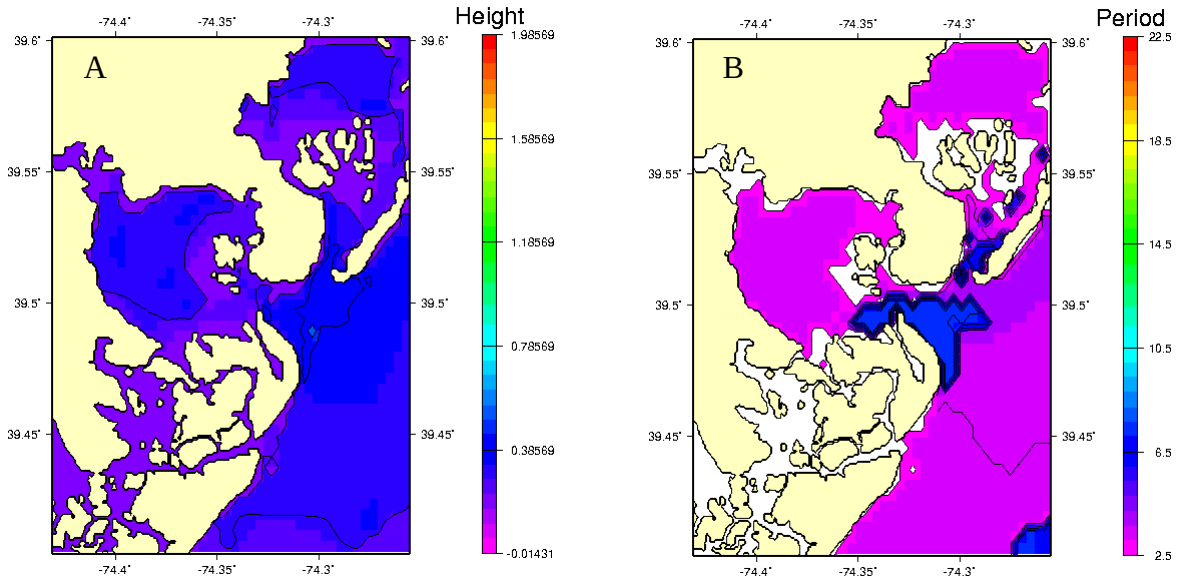

Figure 3.9. Predicted wave fields on the 50 m grid with SWAN at 2200 UT on Nov. 19: (A) Significant wave height. (B) Wave peak period.

A B C D

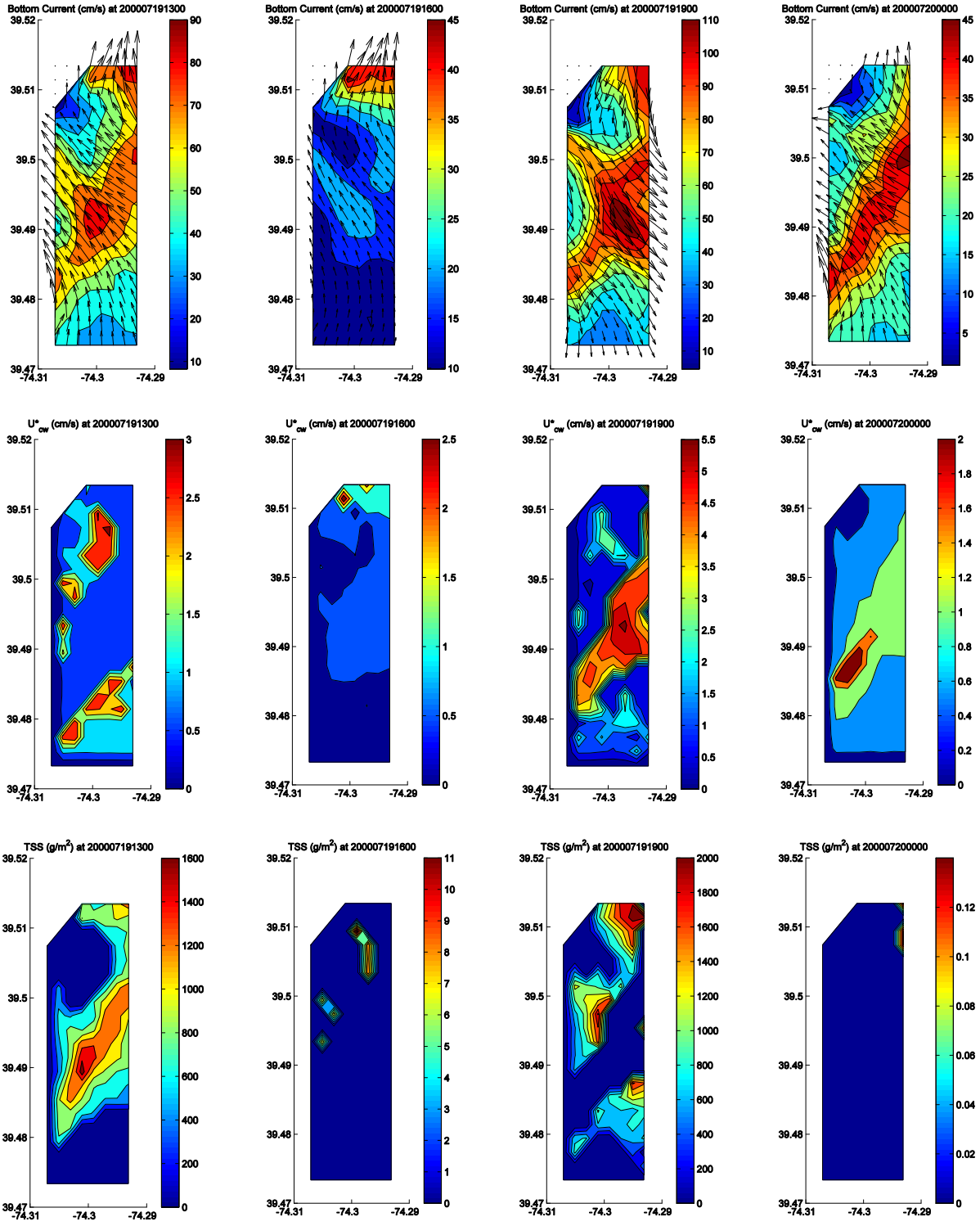
Bottom Current (cm/s) at 200007191300
Bottom Current (cm/s) at 200007191600
Bottom Current (cm/s) at 200007191900
Bottom Current (cm/s) at 200007200000
U*cw (cm/s) at 200007191300
U*cw (cm/s) at 200007191600
U*cw (cm/s) at 200007191900
U*cw (cm/s) at 200007200000
TSS (g/m2) at 200007191300
TSS (g/m2) at 200007191600
TSS (g/m2) at 200007191900
TSS (g/m2) at 200007200000

Figure 3.10. Snapshots of LSOM output on the 100 m grid for the 19 July 2000 forecast in the LEI at: (A) 1300 UT; (B) 1600 UT; (C) 1900 UT; and (D) 2200 UT. Upper row = steady currents; middle row = u_* (no waves); bottom row = Total Suspended Sediment. The domain is shown in Fig. 3.8.

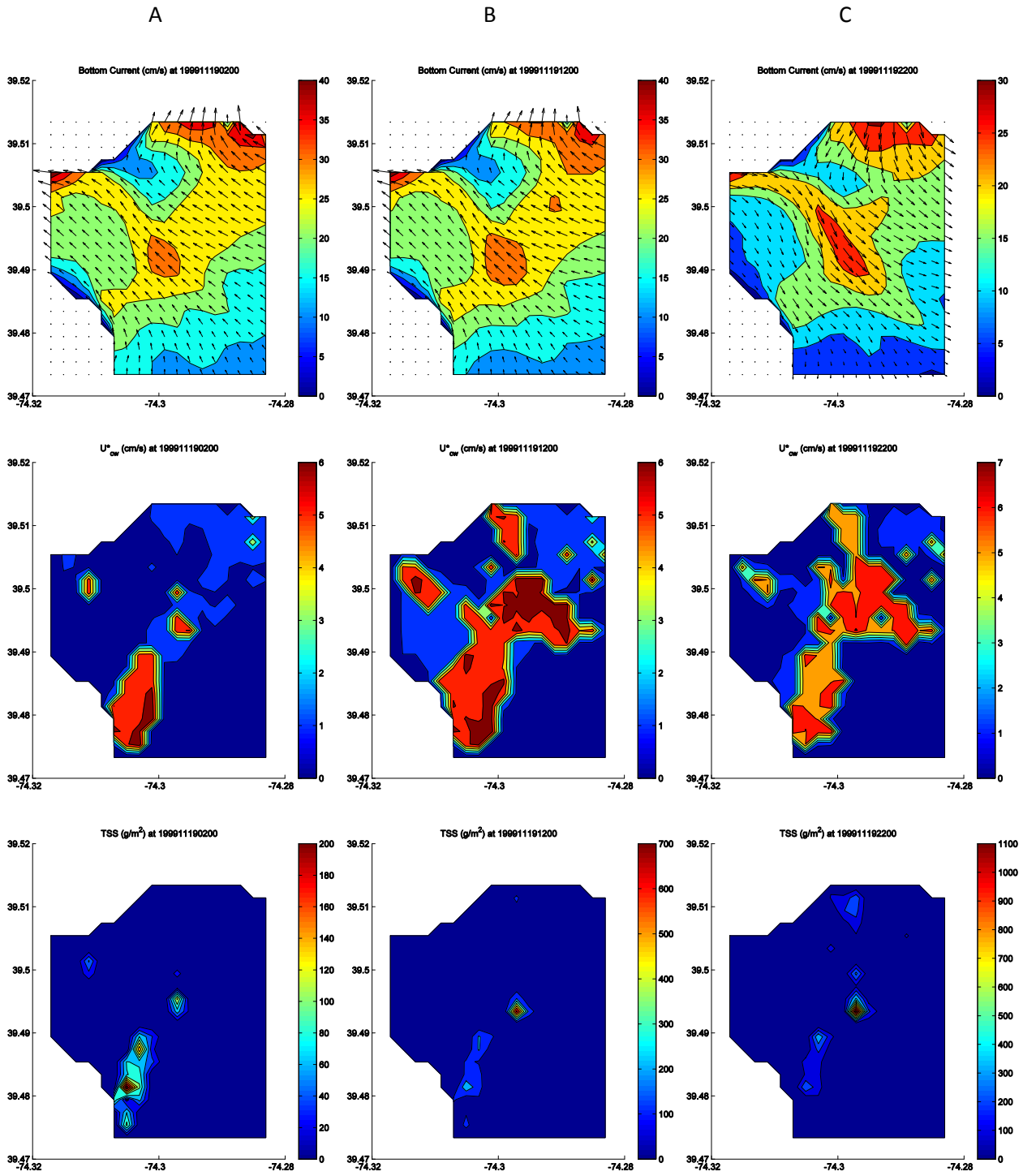

Figure 3.11 Snapshots of LSOM output on the 100 m grid for 19 Nov. 1999 in LEI at: (A) 0200 UT; (B) 1200 UT; and (C) 2200 UT. Upper row = steady currents; middle row = u_{*cw} (with waves); bottom row = Total Suspended Sediment. The domain is shown in Fig. 3.8.

4 Wind and tidal circulation in the Kotar-Boka Bay estuary, Montenegro

The eastern shore of the Adriatic Sea is bounded by the Dinaric-Hellenic belt (Balkan Mountains), which resulted from the Mesozoic to Neogene convergence between the Adriatic and Eurasian crustal plates. These mountains comprise Mesozoic shelf sediments that have been faulted, folded, and eroded by groundwater to form a complex terrain of steep peaks and narrow gorges (Zelic, Levi et al.). The eastern shore of the Adriatic Sea thus contains many tectonic estuaries like the Kota-Boka Bay estuary of Montenegro (Fig. 4.1A). This estuary consists of three connected basins with maximum depths of 55 m (Fig. 4.1B). These sub-basins are connected by narrow passages with depths < 20 m.

The steep slopes of the Balkans are responsible for the Bora winds, which blow from the north through gorges and mountain passes to the Adriatic Sea (Horvath, Ivatek-Sahdan et al. 2009). The impact of these extreme atmospheric events on circulation and sedimentation in the Adriatic has been the subject of several measurement and modeling studies (Cushman-Roisin and Korotenko 2007; Bogunovic and Malacic 2008; Ferrarese, Cassardo et al. 2008; Bever, Harris et al. 2009). The influence of these winds on estuary circulation has not been investigated as much, however (Kourafalou 1999; Cucco and Unigiesser 2006; Gacic, Kovacevic et al. 2009). A preliminary study was thus undertaken to examine any special problems associated with circulation in the Kota-Boka Bay system, which is strongly influenced by orographic effects on the local wind.

The period examined in this study was 14-15 June, 1999. The Bora wind does not occur in summer, however. In fact, there has been a recent decrease in these winds and the southerly winds of the Adriatic have been the dominant atmospheric forcing for several decades (Pirazzoli and Tomasin 1999). The wind was simulated using COAMPS on a 6-km grid. The wind field consisted of two patterns; a NNW wind (Fig. 4.2A) and a southerly wind (Fig. 4.2B). The maximum wind speed was 4.3 m/s. These wind fields were approximately equally distributed over the simulation interval of 36 hr, with the southerly wind occurring during the day (local time = UT+1 hr). The primary meteorological event thus appears to be a local sea breeze.

The circulation during the simulation interval was modeled using POM on a Cartesian grid with uniform cells of 50 m along both axes. Temperature and salinity were constant (20° and 35 psu, respectively). No freshwater inflow was incorporated. The open boundary was forced by mixed tidal elevations (Fig. 4.3), with estimated semidiurnal and diurnal amplitudes of ~10 cm each. A recent study suggests these amplitudes should be 8 cm and 6 cm, respectively, and that the components should not be perfectly in phase (Cushman-Roisin and Naimie 2002).

The simulated tide was at low water at 0100 UT on 15 June (hour 25 in Fig. 4.3) and the predicted water level was uniform throughout the estuary except for the furthest reaches of the upper bay. The wind varied from westerly near the mouth to northerly in the upper bay (Fig. 4.2A) but it was too weak to have a dramatic effect on the bottom currents because of the basin depth (Fig. 4.4A). The main flow is into the basin at < 5cm/s but there is a shallow current along the eastern shore of the central basin (Kota Bay). The flow increases to 15 cm/s through the channels. The tide was ebbing at 1100 UT (Fig. 4.4B) while the wind was southerly (Fig. 4.2B). There seems to be a more noticeable effect at this time near the mouth and within the lower bays. The flow along the shallow margins of the lower bay is into the bay rather than out as suggested by the ebb tide. This is noticeable in the shallow channel between the lower bay and Kota Bay where the flow is to the east at ~8 cm/s.

Neither wave nor sedimentation calculations were completed for this study. The local geology further suggests that there is very little mobile sediment because the dominant rock type is limestone, which produces no sediment in this environment. This study is useful in that it demonstrates the interaction of tides and winds in steeply sided tectonic basins, as well as the importance of higher resolution wind fields that can capture local effects like sea breeze and orographic steering of winds.

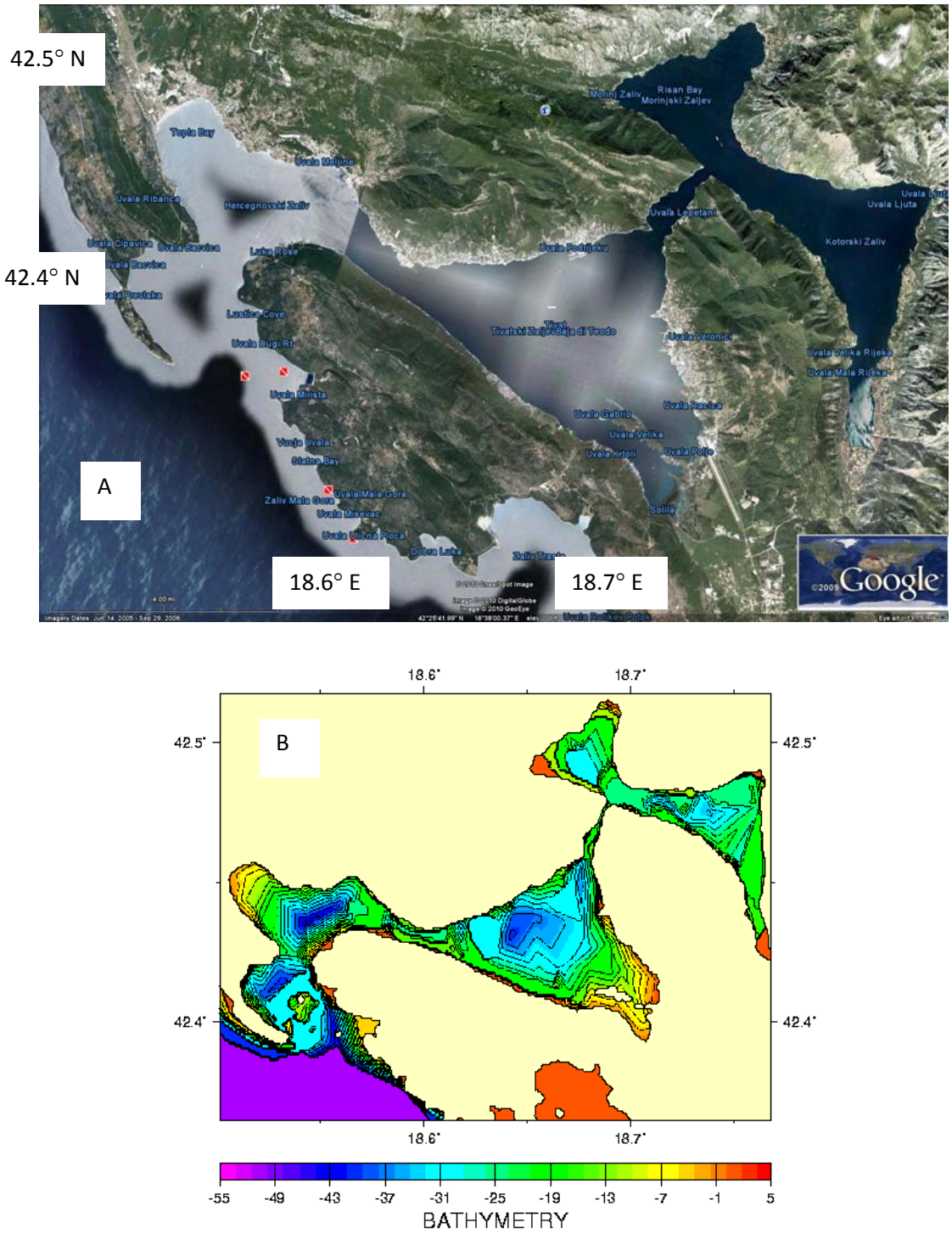

Figure 4.1. (A) Satellite image of the Kotar-Boka Bay estuary near Tivat, Montenegro, on the Adriatic east shore. (B) Bathymetry compiled from nautical charts.

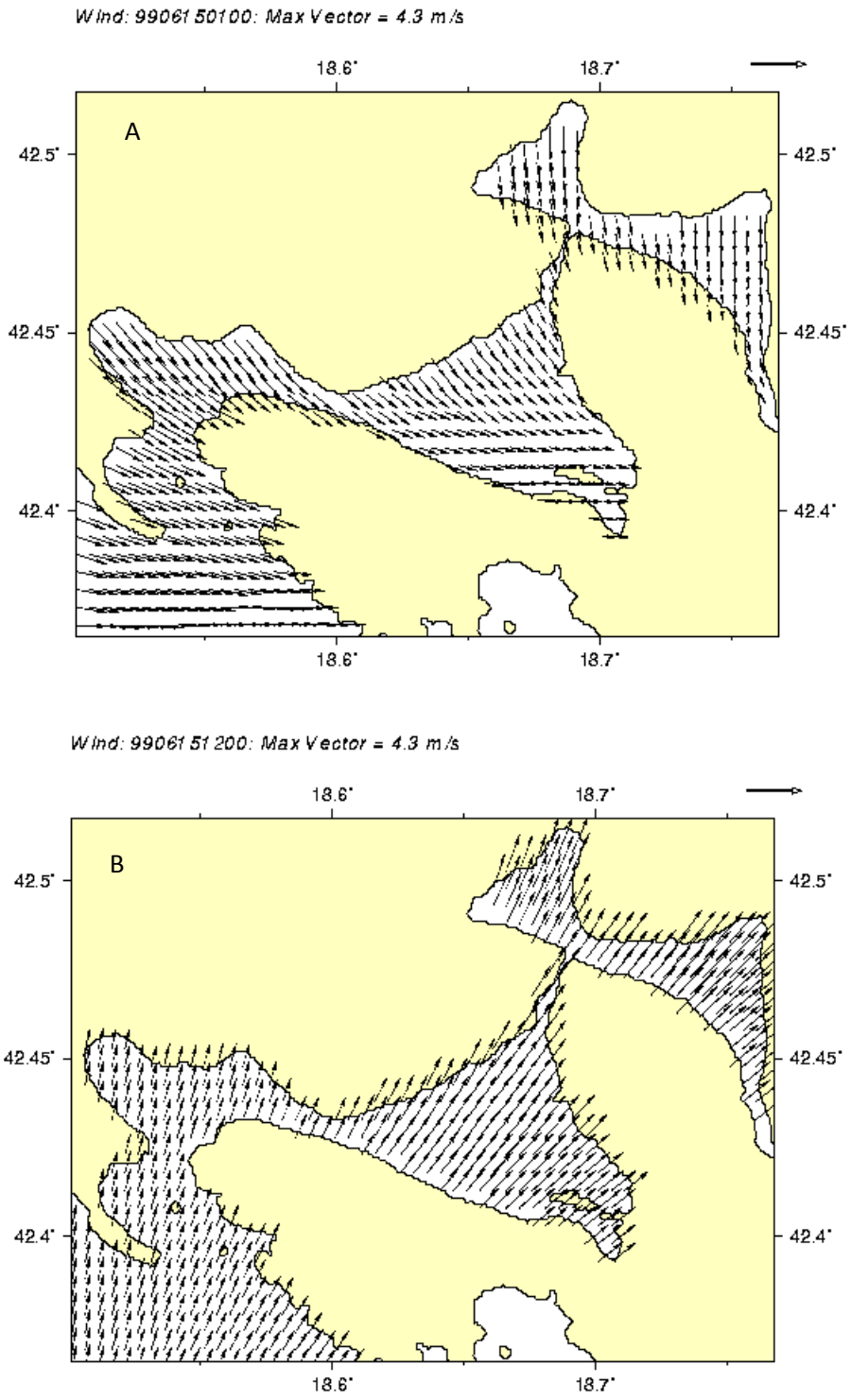

Figure 4.2. Wind field computed by COAMPS for the Kota-Boka estuary on 15 June 1999: (A) 0100 UT; (B) 1200 UT.

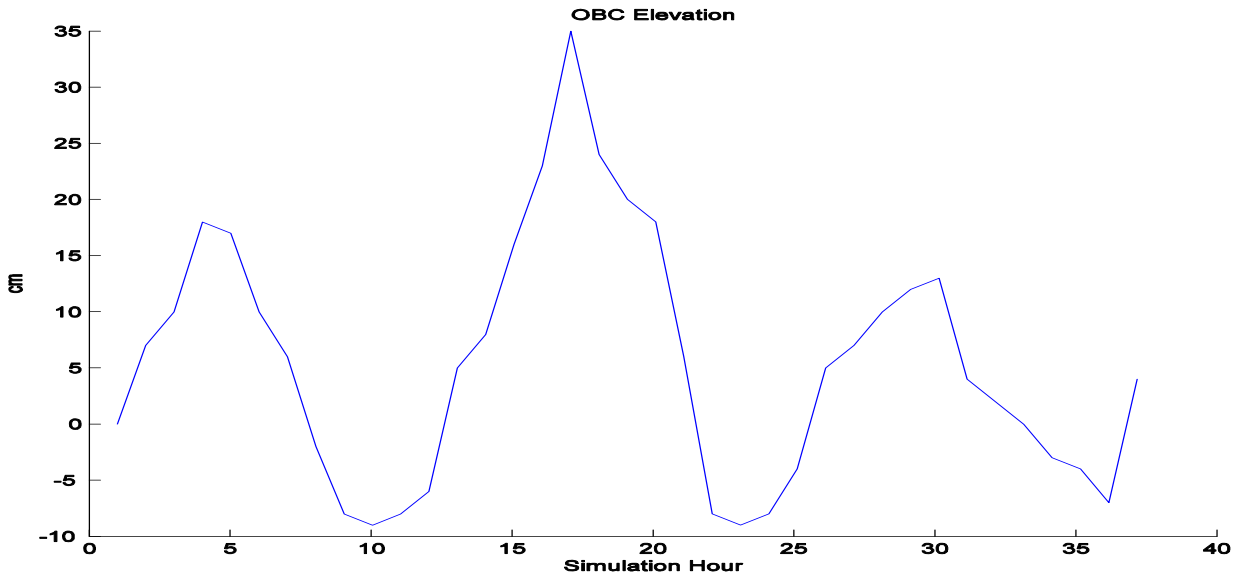

Figure 4.3. Time series of estimated elevations at the open boundary.

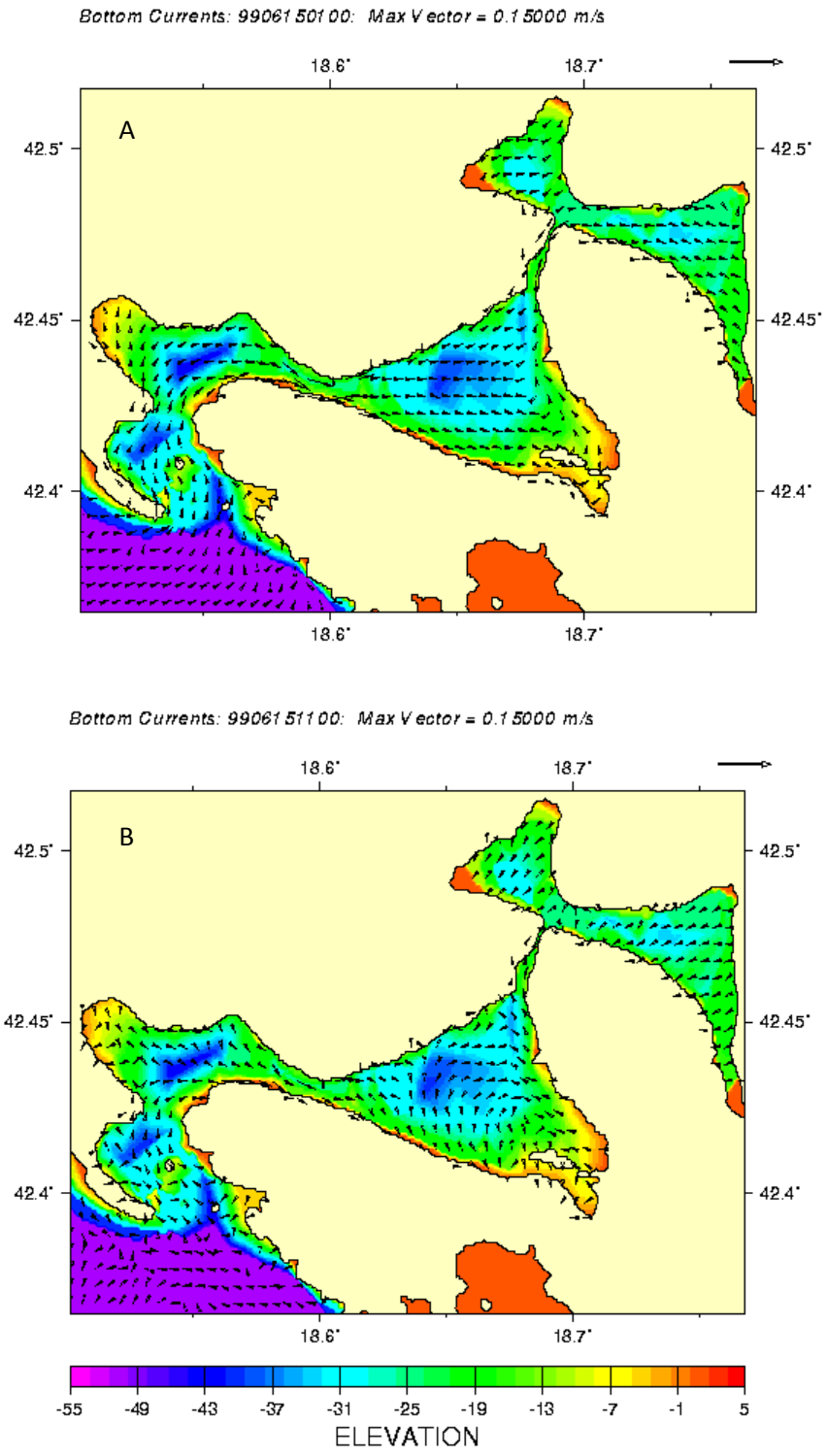

Figure 4.4. Simulated bottom currents from POM for the Kota-Boka Bay system on 16 June 1999: (A) 0100 UT and (B) 1100 UT. The contours are bathymetry in meters.

5 Hydrodynamics, sediment resuspension, and contaminant transport in San Francisco Bay, California

San Francisco Bay is a tectonic estuary comprising three sub-basins (Fig. 21): San Pablo Bay in the north; Central Bay; and South San Francisco Bay. These sub-basins have different properties in terms of water depth, seasonal trends, and hydrography. They also have unique ecological and environmental problems. San Francisco Bay has a strong seasonal trend in terms of inflow and resulting salinity (Monismith, Kimmerer et al. 2002), and thus it is not in equilibrium as suggested by the estuarine circulation scheme. It can instead be classified as a monsoonal estuary (Vijith, Sundar et al. 2009), with annual run-off that is many times the volume of the estuary occurring within a short time span (winter). Central Bay has overall properties that are closest to ocean water whereas San Pablo and South Bay have seasonal patterns of organic mass production, alternating between heterotrophic in winter and autotrophic in summer (Smith and Hollibaugh 2006). The ecosystems within the sub-basins reflect a complex interplay of anthropogenic contaminants, salinity, biomass, and terrigenous sediment at tidal to decadal time scales (Cloern 1984; Murrell, Hollibaugh et al. 1999; Ritson, Bouse et al. 1999; van Geen and Luoma 1999; Grenz, Cloern et al. 2000; Lehman 2000; Cloern, Canuel et al. 2002; Schoellhamer 2002). Sewage effluent contributes up to 80% of the nutrients to the bay and anthropogenic contaminants have been a source of toxins within the ecosystem for decades (Pereira, Hostettler et al. 1999). The last decade has seen a concerted effort to restore the bay's habitat to a natural condition (Denisoff and Movassaghi 1998; Travis, Blanchfield et al. 1998). This has required detailed measurements of different contaminant levels throughout the estuary and its biomass (Oram, McKee et al. 2008; Shellenbarger, Athearn et al. 2008; Hwang, Green et al. 2009; Miles and Ricca 2010). Some of this work is related to the closing of commercial salt ponds in South Bay but there are also point sources associated with specific sites like the naval shipyard at Hunters Point (Battelle, ENTRIX et al. 2002).

5.1 Circulation in San Francisco Bay

Much of the scientific work in San Francisco Bay (SFB) has been focused on the ecosystem because of widespread contamination by heavy metals and hydrocarbons (Denisoff and Movassaghi 1998). The general circulation has been discussed in depth (Cheng, Casulli et al. 1993) and will briefly summarized here. The astronomical tides (range ≈ 2 m) and inflow from the Sacramento-San Joaquin delta together dominate flow in the estuary. The mean freshwater inflow in summer is 10^2 m^3/s and 10^4 m^3/s in the winter. Two high tides of different amplitude occur each day. The large tidal range and common shoals create substantial areas of intertidal

mudflats. Furthermore, the spring tide can be as much as twice the neap tide. The major constituents are the semidiurnal M_2 and the diurnal K_1 (Fig. 5.2).

There is a longitudinal salinity gradient along the main channel from the delta to the Golden Gate. Vertical stratification is greatest in winter when freshwater inflow increases. South San Francisco Bay (SSFB) and the shoals are typically well-mixed except during exceptional events. Historical freshwater inflow records (Fig. 5.3) show that delta inflow varies at both annual and seasonal time scales whereas evaporation occurs primarily in the summer (Uncles and Peterson 1996). The observed long-term salinity observations (Fig. 5.4) reflect these cycles. The salinity at Golden Gate (Fig. 5.4, LOWER; panel A) decreased to 13 psu in 1963 and again in 1967 when delta inflow was high (Fig. 5.3A). The salinity steadily decreases upstream, with stations in the Central Bay (Alameda in Fig. 5.4B) showing a multiyear pattern (e.g., 1975 to 1978). The salinities are generally < 15 psu beyond Carquinez Strait (e.g., Sta. 3 and higher).

The TRIM (Tidal, Residual, and Intertidal Mudflat) model has been the mainstay of understanding the hydrodynamics of SFB for many years (Casulli and Cheng 1992; Casulli and Cattani 1994; Cheng, Smith et al. 1998). TRIM incorporates a semi-implicit finite difference scheme for the numerical solution of the three-dimensional shallow water Reynolds equations in which pressure is hydrostatic. The pressure gradient in the momentum equations and the velocities in the vertically integrated continuity equation are discretized with an implicitness parameter (Casulli and Cattani 1994). TRIM has become the *de facto* model for SFB because it accurately predicts tidal and residual flow, as well as salinity (Gross, Casulli et al. 1998; Gross, Koseff et al. 1999; Gross, Koseff et al. 1999). The tides of San Francisco Bay have been examined in detail using TRIM (Cheng, Casulli et al. 1993). TRIM3d has proven useful in elucidating the relationship between river inflow, estuary circulation, and fish distributions (Kimmerer, Gross et al. 2009). It has also been used with success in other coastal estuaries in California (Gross and Stacey 2004).TRIM3d has also been used to examine sediment mobility at Hunters Point Shipyard (Zimmerman, Bricker et al. 2008).

5.2 Modeling Hydrodynamics in San Francisco Bay and the south Basin of Hunters Point Shipyard

Much of the interest in SFB has been focused on environmental concerns but numerical models have been used for only a few cases as discussed above. The closing of the Hunters Point Shipyard in San Francisco, however, has prompted the Strategic Environmental Research and Development Program (SERDP) to fund an in-depth analysis of potential contaminant mobilization and escape from certain areas around the shipyard (Battelle, ENTRIX et al. 2002). A substantial portion of the effort has been directed at characterizing the contaminant distribution and its behavior in the bottom sediment (White, Israel et al. 2002). The initial hydrodynamic measurements at South Basin have been used to evaluate the potential for resuspension by waves during occasional southeasterly winds (Zimmerman, Bricker et al. 2008)

but the transport of dissolved material out of the basin has not been modeled. The purpose of the current study is thus to examine the potential risk of contaminants being released from the bottom and transported into SFSB.

5.2.1 Approach

This study attempts to evaluate the circulation processes at two scales: the entire extent of the estuary from Golden Gate to SSFB, and north to Carquinez Strait; and the tidal basin south of Hunters Point Shipyard (South Basin or SBHP). The estuary simulations were run on a spherical coordinate grid with ~300-m horizontal cells (Fig. 5.5A). The 100 m bathymetry database from the USGS (http://sfbay.wr.usgs.gov) that was used to construct the grid is no longer available. A minimum depth of 2 m was used for all cells.

This simulation covered Dec. 2003 to Nov. 2004. The Hunters Point grid (Fig. 5.5B) used 100 m grid cells and was run for Jan. 2004 only. The SBHP grid (Fig. 5.5C) comprised 30 m cells and was run for Jan. 2004 as well. The vertical axis was represented by 5 sigma levels for all grids. All three grids used NOGAPS winds (Fig. 5.6). The average zonal wind is westerly (blowing to the east) and the average meridional wind is northerly (blowing to the south). The meridional wind is more variable and reveals several events that are characterized by a significant northward component: (1) when the zonal wind is positive, southwesterly winds result (squares); (2) when the zonal wind is negative, southeasterly winds occur (circles). The southeasterly wind is important because it blows into SBHP and maximizes wave fetch. It can also reinforce the flood tide currents flowing into the tidal basin. Note the infrequency of these events, however, with only five occurring in the winter.

The SFB model incorporated additional boundary conditions. The subtidal elevations, as well as temperature and salinity at Golden Gate were taken from the global (1/8°) NCOM database (Barron, Smedstad et al. 2004). The tidal elevations (Table 1) were superimposed on the subtidal flow. The elevations varied across the estuary mouth. Note that they are somewhat different from those computed with the tidally validated TRIM2D model (Cheng, Casulli et al. 1993) that are shown in Fig. 5.2. The tidal elevations and transports were supplied to the HP and SBHP grids through the boundary conditions from the SFB and HP grids, respectively. All models used the NOGAPS wind field, which was uniform because of its coarse grid.

The wave field for Jan. 2004 was simulated using the SWAN wave model. The SFB grid was used as with NCOM and a 30-m grid was nested to this for the SBHP domain. The wind was supplied by COAMPS on the same 300 m grid. This wind field was not available when the NCOM simulations were completed.

5.2.2 Model validation

There are no hydrodynamic observations available for 2004. The predictions from the numerical models will instead be validated against available observations from other years. For example, the nearest NDBC buoy in 2004 was station 46026, located 18 NM (33 km) west of San Francisco. It is appropriate to compare NOGAPS to the buoy because the scales are similar; that is, NOGAPS does not include diurnal (sea breeze) or orographic effects, which are missing in ocean observations as well. The wind speed for Jan. 2004 (Fig. 5.7A) reveals events above 12 m/s on 2, 9, 25, 27, and 31 January. The NOGAPS wind (Fig. 5.6) is shown as components but these can be compared to the buoy to see if these events are reproduced reasonably well. The forecast wind captures events on 2 (12 m/s), 9 (13 m/s), 25 (14 m/s), and 31 (15 m/s). Several others are below 10 m/s. The wind events on 2 and 9 Jan. are southeasterlies (blowing to NW). The measured wind on 2 Jan. had a bearing (Fig. 5.7B) that varied from 230° to 180°. The 9 Jan. wind event varied between 150° and 200°. The forecast wind is in good agreement with the buoy for the Jan. 2004 southeasterly wind events.

The Jan. 2001 observations from the south basin are shown in Fig. 5.8 (Battelle, ENTRIX et al. 2002). These will be compared qualitatively to the model predictions from Jan. 2004. The waves predicted by SWAN (Fig. 5.9A) reveal the expected response to the southerly winds. The largest waves exceed 40 cm during NW wind events, while the significant wave heights remain < 35 cm during NE winds and never reach 10 cm the rest of the time. This is very close to the values measured in the south basin in Jan. 2001 (Fig. 5.8E). It is noteworthy that there were a similar number of such events in the winter of 2001 as well. The wave periods from SWAN (not shown) were also very similar to the observations. The mean currents computed by NCOM on the SBHP grid (Fig. 5.9B) are < 10 cm/s much of the time with peak amplitudes of > 10 cm/s. These are slightly greater than the observed near-bottom currents (Fig. 5.8A), which have tidal maxima of ~7 cm/s with many currents being smaller. The exceptions in the 2001 measurements are the wind events. The highest recorded current was 18 cm/s on 25 Jan. 2001. The model does not reveal this response but the simulated flow does show a disruption of the tidal currents during both NW and NE wind events; however, the currents are reduced rather than enhanced by the wind. The comparison between the models and the observations in SBHP are acceptable for our purpose, which is to examine mixing processes within the SBHP and SFB domains.

It is also useful to evaluate the performance of the SFB model, even though it does not impact the resuspension of sediment in the south basin. It will be used to examine the potential transport of contaminants from Hunters Point if they are mixed into the main bay by the wind events identified in the meteorological records. We will not go into depth for this analysis but limit it to the tides near HPS and the overall flow patterns within the bay, which impact large scale transport on seasonal scales. The measured near-bottom currents north of HPS (not shown) in a small harbor were dominated by semidiurnal east-west flow of < 30 cm/s during

the spring tide (Battelle, ENTRIX et al. 2002). The maximum meridional currents were < 20 cm/s. The residual flow from winter 2001 was to the SSE. The observations show no wind response at all, probably because of the semi-enclosed location of the measurements. The currents from (not shown) the HP grid for NCOM also have a residual flow to the SSE but they are sensitive to the wind because the actual bay where the tripod was installed is not resolved by the 100 m grid. The maximum zonal flow reaches 15 cm/s while the meridional currents attain speeds of 30 cm/s. There is substantial variability, however. It seems that the flow from NCOM is dominated by N-S flow, whereas the observations indicate E-W flow dominance. However, the observations were definitely collected along an E-W oriented coastline, which will exercise some control over the local flow. This subjective comparison suggests that a more detailed comparison of several locations within SFB is needed but it is beyond the scope of this report.

The response of the SFB estuary to the annual cycle of inflow from the delta can be evaluated using surface salinity. Salinity maps from the middle of each month (Fig. 5.10) reveal the impact of winter rains. The model salinity in San Pablo bay reaches a minimum of 2.1 psu in March when low salinity reaches as far south as Hunters Point. The salinity in the upper bay then increases to a summer high of 24 psu in Aug. and Sep. The salinity in South San Francisco Bay approaches oceanic values in Sep. to Dec. These predicted salinities can be qualitatively compared to the results from Fig. 5.4 (Uncles and Peterson 1996). A mean monthly delta inflow of 1620 m^3/s with a salinity of 2 psu was used for March in the SFB model at Carquinez Strait. This inflow corresponds approximately to water year 1979 (Fig. 5.3A), which can thus be used for a comparison of salinity gradients in the bay. The observed mean salinity minimum for 1979 at Station 1 (panel A of lower part of Fig. 5.4) was ~28 psu. The nearest grid cell from the SFB model had a value of 15 psu in mid-Mar, which is considerably lower than the observed mean but higher than the minima from 1983 and 1987. The simulated salinity at Station 2 (Alameda) is ~17, which is closer to the mean of 23 psu from the observations. The other stations are in the delta (upper panel in Fig. 5.4) and outside the model domain. This same comparison can be made for the summer, when delta inflow is low. The mean monthly inflow for the model in September was 600 m^3/s (salinity at Carquinez = 28 psu), which is comparable to most of the summer observations (Fig. 5.3A). The simulated salinity is uniform in the Central and South San Francisco Bays, with values of ~32 psu at Golden Gate and Alameda, respectively. The corresponding observed surface salinities for summer was 32 psu and 30 psu at these same stations. The summer salinity appears to be slightly better predicted, probably because there is less variability in summer inflow than winter between years.

A final comparison of the model salinity can be made with observations collected along the main channel of the bay in 2004 (Fig. 5.11). The winter values (February) are 8 psu lower than summer (September). The boundary condition in NCOM used salinities that were as much as 10 psu too high. This will work with the lack of accurate inflow to cause the model to calculate incorrect salinity throughout the bay. The evaporation rate in the model was 0.3×10^{-7}, which is

in close to the mean annual value from Fig. 5.3C. As expected, the model did better in the summer (red squares in Fig. 5.11B). There is no reason to complete an in-depth analysis of the salinity data because of the known problems with the boundary condition (salinity and inflow rate), low-resolution wind fields, and lack of annual variability of evaporation. Nevertheless, the patterns of salinity predicted by the model (Fig. 5.10) are reasonable since there are no available images of surface salinity or temperature for spatial comparisons. There are remote sensing images of surface sediments (Ruhl, Schoellhamer et al. 2001) but these cannot be used because suspended sediment can originate from the bay bottom and thus does not reflect transport only.

5.2.3 Hindcast wind, waves, and currents at Hunter Point

The predicted currents in the south basin at Hunters Point were primarily barotropic because of the shallow water. We will thus examine the flow during a southeasterly wind event using near-bottom currents (Fig. 5.12). The model included tidal forcing, which can obfuscate the residual flow due to the wind. To minimize this problem, we will focus on ebb currents during the wind event of 8-9 January. This is also useful because the ebb tide would transport suspended or dissolved material into the main bay from the tidal basin. The expected SE flow caused by a northwesterly wind would fail to do this because the wave fetch would be limited by the basin size, and there would be no release of sediment-bound toxins.

The wind began to blow from the south on 5 Jan. and reached 10 m/s at 2300 UT (first circled time in Fig. 5.6B), at which time the hindcast wave heights within SBHP were negligible. The wind rotated to southeasterly (zonal currents more negative in Fig. 5.6B) and the predicted waves reached 25 cm in the tidal basin at 1200 UT on 6 January. The wind remained steady and hindcast wave heights peaked at 42 cm in the south basin at 0600 UT on 7 Jan. (circled in Fig. 5.9A). Despite the steady southeasterly wind, wave heights in SBHP decreased to 10 cm by 1200 UT. The only potential cause of this appears to be a brief interval when the hindcast wind was almost directly from the SE. This time is indicated by the arrow in Fig. 5.6B. The wind was more southerly both before and after 1200 UT on 7 January. There is no evidence of wave attenuation or breaking on the shallow ledge outside of the tidal basin (not shown), however. The cause of this dramatic decrease in wave heights requires further investigation beyond the scope of this report.

The simulated currents reached 6 cm/s along the eastern shoreline of SBHP at 0000 UT on 8 Jan. (Fig. 5.12A) immediately after high water (see Fig. 5.9C). This flow extended from the NE corner of the tidal basin to outer basin in the SE. The wave heights increased again to > 35 cm. The wind strengthened on 8 Jan. and reached a maximum of 13 m/s at 0000 UT on Jan. 9 (second circled time in Fig. 5.6B). The high tide occurs 50 min later each day (Cheng, Casulli et al. 1993) and thus the tide was still at high water (see Fig. 5.9C) 24 hr later, at 0000 UT on 9 Jan. (Fig. 5.12B). The currents inside the south basin were to the NW because of the persistent southeasterly wind and weak (< 1 cm/s) residual flood tide flow. The predicted high water

occurs ~2 hr earlier in the outer basin and thus ebb currents were 3 cm/s to the SE. The predicted currents near the SE shoreline are ~9 cm/s landward rather than into SFB because of the combined ebb tide and the northward wind stress. The most likely reason for the hindcast wave height in SBHP being only 20 cm despite the higher wind speed was the more southerly wind and resulting reduced fetch. This is an interesting contradiction to the situation on 7 Jan. as discussed in the previous paragraph, when larger waves were predicted during southerly winds.

The wind decreased to < 5 m/s over the next 24 hrs and, consequently, waves in SBHP were less than 5 cm at 0000 UT on 10 January (Fig. 5.9A). The flood tide was nearing high water and thus flow was to the NW within the tidal basin (Fig. 5.12C). The near-bottom currents were towards the ESE in the outer basin, however, because of the aforementioned phase lag in the tidal basin. By 2100 UT, the flood tide was propagating into the tidal basin (Fig. 5.9C) and near-bottom currents reached 9 cm/s at its entrance (Fig. 5.12D). The weak wind was not a factor and waves remained < 5 cm. Note that the currents in the outer basin had already begun to ebb.

The discussion above indicates the complexity of hydrodynamic processes in the south basin at Hunters Point. The interaction of tide- and wind-driven steady currents, with oscillatory wave motion in this shallow water is exacerbated by the low magnitudes of most of these processes. This makes it problematical to interpret the observations and model results with respect to the potential release and transport of contaminants contained within the tidal basin sediments. The model currents during high water (Fig. 5.12B) show a CCW transport within SBHP that is in agreement with the observations and residual sediment flux (Battelle, ENTRIX et al. 2002; Zimmerman, Bricker et al. 2008). This transport regime includes a SE flow driven by the ebb tide. This flow is visible in Fig. 5.12A, which shows widespread flow into the outer basin and transport along the eastern shore. The next section will examine the interaction of the waves with this transport regime during southeasterly wind events in an attempt to demonstrate the potential for release and transport of sediment-bound toxins.

5.3 Contaminant release and potential transport during southeasterly wind events

This modeling work was undertaken to demonstrate the viability of general circulation and sedimentation models to understand and predict the movement of toxins in San Francisco Bay and other polluted waterways. Thus, the models have not been highly refined or calibrated for this work. This has reduced their accuracy as seen above, but it can demonstrate if our understanding of estuarine processes is sufficient to avoid localized parameterizations of key processes. The approach used here consists of two components: (1) demonstrate if bottom sediment can be entrained, or resuspended, during the SE wind events; and (2) identify potential transport pathways from the inner basin into SFB that are correlated with the timing of these resuspension events.

5.3.1 Approach

This report describes an approach similar to that used previously at Hunters Point (Zimmerman, Bricker et al. 2008). The hindcast waves from SWAN are combined with the near-bottom currents from NCOM on the 30 m (SBHP) grid using a wave-current bottom boundary layer model (BBLM) that is included in the Littoral Sedimentation and Optics Model (LSOM), which has been described elsewhere (Keen and Holland 2010). The bottom sediments in the south basin range from clay to gravel (Battelle, ENTRIX et al. 2002). To simplify the sediment modeling, a single size class was used in this study–fine sand with a median grain diameter of 74 microns. This grains have a critical shear stress τ_c = 0.86 Pa (u_{*c} = $[\tau_c/\rho]^{0.5}$ or 2.9 cm/s), which is higher than a typical value for clays (e.g., τ_c = 0.4 Pa or u_{*c} = 0.63 cm/s); however, it is representative of consolidated sediments in low-energy environments with low sedimentation rates (e.g., τ_c = 0.1-0.3 Pa). If the bottom sediment is entrained, contaminants that are adsorbed to sediment particles or trapped in pore spaces are assumed to be released into the seawater because of its salinity. The transport of the sediment itself is not important to understanding contaminant exchanges because the dissolved material moves freely with the water.

The release of dissolved contaminants into the water is treated as a point source problem in this study. It is assumed that the toxin is instantaneously exchanged between the sediment/bed and the water column. This boundary condition has been simplified by using a constant release rate. The total quantity of available tracer (dissolved contaminant) is controlled by making the simulations last only as long as the sediment may be disturbed by wave action in the tidal basin. This simple approach has the advantage of being useful for a qualitative evaluation of the causes of high concentrations of the tracer. The computation of tracer movement is completed with the HydroQual Contaminant Model (HQCM) (Anonymous 1998; Keen and Holland 2010). These simulations were performed for 4-10 Jan. 2004.

The potential transport of dissolved tracers by currents in San Francisco Bay can also be evaluated using Lagrangian particle tracking. This technique has been applied to particles within the SBHP grid (30 m cells) using a commercial algorithm (Keen, Ko et al. 2006). The particle-tracking algorithm contained within the HQCM model was used to examine the influence of estuary-scale circulation (on the 300 m SFB grid) on the movement of dissolved tracers that have escaped the tidal basin (Keen and Harding 2008). The tracer calculations were performed for Jan. and Feb. 2004.

5.3.2 Model validation and results

Validation of the models is necessarily qualitative because no observations were available for 2004 and no open boundary conditions from global NCOM or wind forcing from COAMPS was available for 2001. This is not problematic, however, because the hydrodynamics in South Basin are dominantly local and not subject to annually variable factors like freshwater inflow from the Sacramento-San Joaquin delta. The effect of large-scale circulation on drifter

trajectories will be seen to be dominated by tidal flow as suggested in previous work (Galt, Cheng et al. 1997).

The bottom orbital velocities measured in the south basin at Hunters Point (Fig. 5.8C) are a good indication of the timing of resuspension events. As expected, the background values are quite low (< 1 cm/s). The wave events on 23-24 and 26 Jan. 2001 produced SWH = 25 and 35 cm, respectively (Fig. 5.8E). The maximum bottom orbital velocity of 20 cm/s occurred on 26 Jan. whereas the slightly smaller waves on 23-24 Jan. generated wave currents of only 15 cm/s. The smaller waves during this event also had slightly shorter periods (Fig. 5.8D) of 3.5 s versus 4 s on 26 January. Significant wave heights predicted by SWAN during the SE wind event of 6-9 Jan. 2004 (Fig. 5.6B) were 40 cm in a water depth of 1.8 m in SBHP (Fig. 5.14A) and wave periods ≈ 4 s (Fig. 5.14B). These waves are comparable to the Jan. 2001 observations. The maximum bottom orbital diameter computed by the BBLM (Fig. 5.14C) is 130 cm in this shallow water and the corresponding orbital speed (Fig. 5.14D) ≈ 45 cm/s. These oscillatory currents are larger than the observations because the 20-cm height of the measurements was above the wave boundary layer was most of the time. The values reported in Fig. 5.8C represent wave motion above this layer. The model predictions from Jan. 2004 are, therefore, considered representative of bottom flows during SE wind events.

The hourly total suspended sediment (TSS) concentrations in the south basin in Jan. 2001 (Fig. 5.8B) were measured 20 cm above the bed. These concentrations are directly correlated to the waves because the steady (tidal) currents (Fig. 5.8A) were small during the wind events, except for a brief spike on 26 January. The peak TSS of 700 mg/L occurred during the first event (23-24 Jan.) and a smaller concentration (~ 300 mg/L) was measured on 26 January. These numbers will be used to evaluate the validity of the BBLM concentrations in Jan. 2004. There are a number of assumptions to consider in comparing the Jan. 2001 observations to the model predictions for 2004. As discussed above, this study used fine sand instead of clay and silt. This was necessary because the clay entrainment function in LSOM requires some knowledge of several bottom parameters that were not available for this study (Keen and Furukawa 2007). Nevertheless, fine sand can be a proxy for the heterogeneous, partly consolidated, sediment in the south basin by calibrating the entrainment algorithm. The least known of the model parameters is the resuspension coefficient, with reported values ranging from 0.00016 to 0.015 (Keen and Stavn 2000). A value of 0.0005 was selected after several tests were completed. The objective was to produce similar magnitudes to Jan. 2001 because the forcing was similar. The resulting peak TSS values of 450 mg/L (Fig. 5.15) are within the acceptable tolerance for predicting concentrations in this environment. Note that both the predicted TSS time series and the observations (Fig. 5.8B) reveal the sensitivity of entrainment to the τ_c threshold; there are few intermediate values in either record.

The maximum TSS predicted by LSOM during this simulation was at 2300 UT on 6 January. The BBLM calculates two important quantities that relate to contaminant release from the bed.

The first is the active layer depth, which is the thickness of sediment moving as a near-bottom layer that includes particles contained in ripples and bouncing along (saltating). The active layer exceeded 14 cm in thickness at the resuspension maximum. The second quantity is the equivalent bed thickness of sediment particles in suspension, the resuspension depth. There was only one size of particles in these simulations, and the maximum resuspension depth of 0.54 mm (540 microns) did not occur at the same time as the active layer maximum. The predicted u_{*m} at 2300 UT was 9.2 cm/s (τ_m = 8.7 Pa). The depth of erosion can thus be qualitatively compared to the results from laboratory experiments on sediments from Hunters Point (Zimmerman, Bricker et al. 2008). The Sedflume device was used to measure the erosion rates for homogenized sediments after 1 hr and 16 d of consolidation. The erosion rate for sediments at 1 and 13 cm in a core (16 d settling) at a shear stress of 6.4 Pa was 0.01 and 0.008 cm/s, respectively. The same core had a constant erosion rate of ≈0.03 cm/s at a shear stress of 8 Pa. This result suggests that the surface sediments would have been instantly removed. The Sedflume result below the surface of the core does not help because the tested cores were homogenized before settling, thus obliterating their original structure. The similarity of the measured and predicted TSS suggests an erosion depth ≈10 cm, below which the sediment would have been too consolidated to erode because consolidation time would be months rather than days in this low-depositional environment. This hypothesis could not be tested, however, because the deposition rate and consolidation time were both unknown. Having a reasonable estimate of these parameters would improve the LSOM prediction (Keen and Furukawa 2007).

Dissolved toxins and heavy metals are mixed into the bottom sediment by burrowing organisms like clams and worms. These contaminants are released when the bottom sediment is disturbed. The timing of the releases is thus directly related to the significant wave height through the bottom shear stress. The predicted TSS concentration in the south basin had peaks at 0600 and 2300 UT on 7 January (Fig. 5.13). These are likely times for contaminants to be released into the tidal basin. This potential release was simulated in the model using a steady rate of 5 ppt (units are arbitrary) at two locations as shown in Fig. 5.13. The HQCM tracer module was run from 0000 UT on Jan. 7 to 2100 UT on Jan. 8.

The initial tracer release coincides with the resuspension event on 7 Jan. during a SE wind and a low tide (Fig. 5.9). During the ensuing flood tide, the tracer released within the inner basin was transported westward and collected along the western shore (Fig. 5.16A-G). The flow was complicated by the steady SE wind and a secondary high tide at ~1200 UT on 7 January. The CCW circulation within the south basin is seen in the accumulation of the tracer along the western side of the inlet (Fig. 5.16D). The primary high tide occurred between 1800 and 2100 UT and the wind transported the surface water back to the NW and into the inner basin (Figs. 36F, G). The tracer concentration along the western shore was reinforced by the point source just outside the inner basin (Fig. 5.16D). The strong ebb tide during the early hours of 8 Jan. (>10 cm/s) transported the surface tracer along the eastern shore into the outer basin (Figs. 36H-K) before low tide occurred at 1200 UT (Fig. 5.16L). The concentration of the tracer

became quite high in the model and eventually caused numerical instabilities. This is considered acceptable for this application because the actual concentration were unknown as were the release rates. This problem requires further study to understand fully.

A second approach to evaluating the paths of contaminants released from sediments at HPS is to use particles as Lagrangian tracers. This does not directly calculate concentrations, but they can be estimated with adequate knowledge of the release rates and type of dissolved material (Anonymous 1998). This study does not attempt to estimate the concentrations but simply tracks the particles, which do not have decay rates either. Particles that contact the bottom or sides of the domain remain immobilized. This approach was used successfully in the Gulf of Papua (Keen, Ko et al. 2006). The particle model was applied to transport around HPS using the currents calculated by NCOM on the SBHP grid for Jan. 2004 (Fig. 5.17). After 31 days of transport, the heavier particles, which are representative of silt, are primarily distributed around Hunters Point (yellow points in Fig. 5.17). Those released within the south basin are apparently trapped. The lighter particles, which are more like clays and colloids, however, are widely distributed around the HPS area but they have not moved offshore into the main bay (aqua points in Fig. 5.17) although a few have reached the eastern extent of the SBHP grid. The interesting result from this simulation is that particles with finite settling velocities have reached the main bay. This transport occurred over several days under a range of flow conditions. The implication is that, even if adsorbed toxins require several days' exposure to salty water to become dissolved in the water, it is likely that some contaminant would be dissolved into the waters of the main bay.

The results of the tracer simulation (Fig. 5.16) and the particle tracking (Fig. 5.17) for Hunters Point Shipyard together suggest that some quantity of toxins will reach SFB either by direct transport as a solute or release from sedimentary particles suspended in the water column. The final simulation, therefore, is directed at evaluating the potential transport of dissolved toxins within SFB that originate at HPS. Neutrally buoyant particles were released near HPS every 24 hr during Feb. 2004 and tracked with the particle tracking algorithm contained within HQCM (Anonymous 1998). There is very little difference in the spatial distribution of particles after 15 and 28 days in the bay (Fig. 5.18). Particles have reached the southern end of the bay and even into the entrance to San Pablo Bay (Note that for only one particle release per event, there is no numerical diffusion added to the transport and the particles go only where the NCOM currents and diffusion take them.). The distribution reveals the effects of convergence caused by the tidal flow moving from shallow to deep water. This type of convergence occurs in SFB along the deep channel in South Bay (Galt, Cheng et al. 1997). Thus, the pattern in Fig. 5.18 indicates the main channel as well as areas where tidal currents impact the coast. This result is slightly different from that of Galt et al. (1997) (Fig. 5.19) because they used a barotropic model and assumed the oil was limited to the surface. Their model thus did not include surface flow in response to the wind or freshwater input.

5.4 Summary

The simulation of atmospheric, hydrodynamic, sedimentation, and solute transport processes in San Francisco Bay serves as an example of the kind of multi-scale, multi-model approach required in estuarine applications. The purpose of this study was deceptively simple: Can sediment-bound toxins in a small tidal basin escape into the bay and what effects might they have? The south basin at Hunters Point is very small (see Fig. 5.1) but it is only one of many such potential localized areas of interest in the sprawling SFB estuary. Interest in these localized areas is not limited to contaminants, but also includes fish spawning, the spread of invasive species, ecosystem reclamation and restoration, and commercial development. The critical parameter in this study was the potential concentration of several toxins in the water of the main bay. In order to achieve this objective, it was first necessary to examine the potential release of these toxins from the bottom within a shallow tidal basin using very-high resolution numerical models. However, these models could not be treated as independent because of tidal flow within the bay. This necessitated the use of a bay-wide model. The effort to understand the processes that control the release and transport of the toxins was further complicated by their tendency to adsorb to undisturbed fine sediments, but go into solution when in turbulent contact with seawater.

This study has demonstrated some of the problems associated with multi-scale, multi-model simulations. As with most estuary models, the water depth is critical. The shallow water in the south basin is a determining factor in sediment resuspension. A small uncertainty in depth can decrease the wave-current bottom stress below the critical threshold for entrainment and completely change the results. For the same reason, it is important to simulate the tidal amplitude and phase accurately so that the water depth is correct. The wind field is very important in estuaries because of the generation of local waves and currents, which were seen to be important in the south basin. Nesting multiple grids for the NCOM simulations was not a problem in this study but it is important to describe the boundary conditions accurately along the edges of the model grids. For larger scale problems (e.g. ecosystem response to changes in freshwater inflow), it is very important to properly describe the sources of freshwater into the system.

This study is fundamentally robust despite the limitations described above because it utilizes individual numerical models that capture the discrete processes that contribute to the result. The coupling between these models is limited to the basic forcing required for their application. For example, NOGAPS was coupled to NCOM only through the wind stress, which was shown to be valid for this study (compare Figs. 5.6 and 5.7). The nested NCOM grids included boundary conditions for temperature and salinity but these variables were not fundamental for the problem of interest. This is important because of the low skill NCOM demonstrated for salinity in this study (Fig. 5.11). The transport of suspended sediment and dissolved toxins from the south basin to SFB is considered reliable because it is dominated by tidal and wind flow, both

of which are consistent with observations from 2001. This is because both the tides and the seasonal wind patterns are repeatable in the SFB estuary. The release of toxins is also considered reliable because the waves and TSS results are in agreement with observations. We have examined each model result independently and found them to be accurate within acceptable tolerances for this problem. The combined result is, therefore, consistent with observations and accurate to the skill level of the models. After setting up, validating, calibrating, analyzing, and coupling this suite of numerical models, we can answer our deceptively simple question with some confidence.

Table 5.1. Tidal constituents used at the open boundary for the SFB model domain. The actual values varied across the estuary entrance. These are the values at cell (1, 134).

Constituent	Elevation		Normal Velocity		Tangential Velocity	
	Amplitude (m)	Phase (Degrees)	Amplitude (m/s)	Phase (Degrees)	Amplitude (m/s)	Phase (Degrees)
K1	0.303	320	0.145	169	0.171	93
O1	0.198	214	0.213	111	0.233	129
P1	0.095	219	0.529	137	0.065	89
Q1	0.033	200	0.136	111	0.190	101
K2	0.033	183	0.117	114	0.196	122
M2	0.450	187	0.281	253	0.830	137
N2	0.102	163	0.706	110	0.584	74
S2	0.112	191	0.317	46	0.021	117

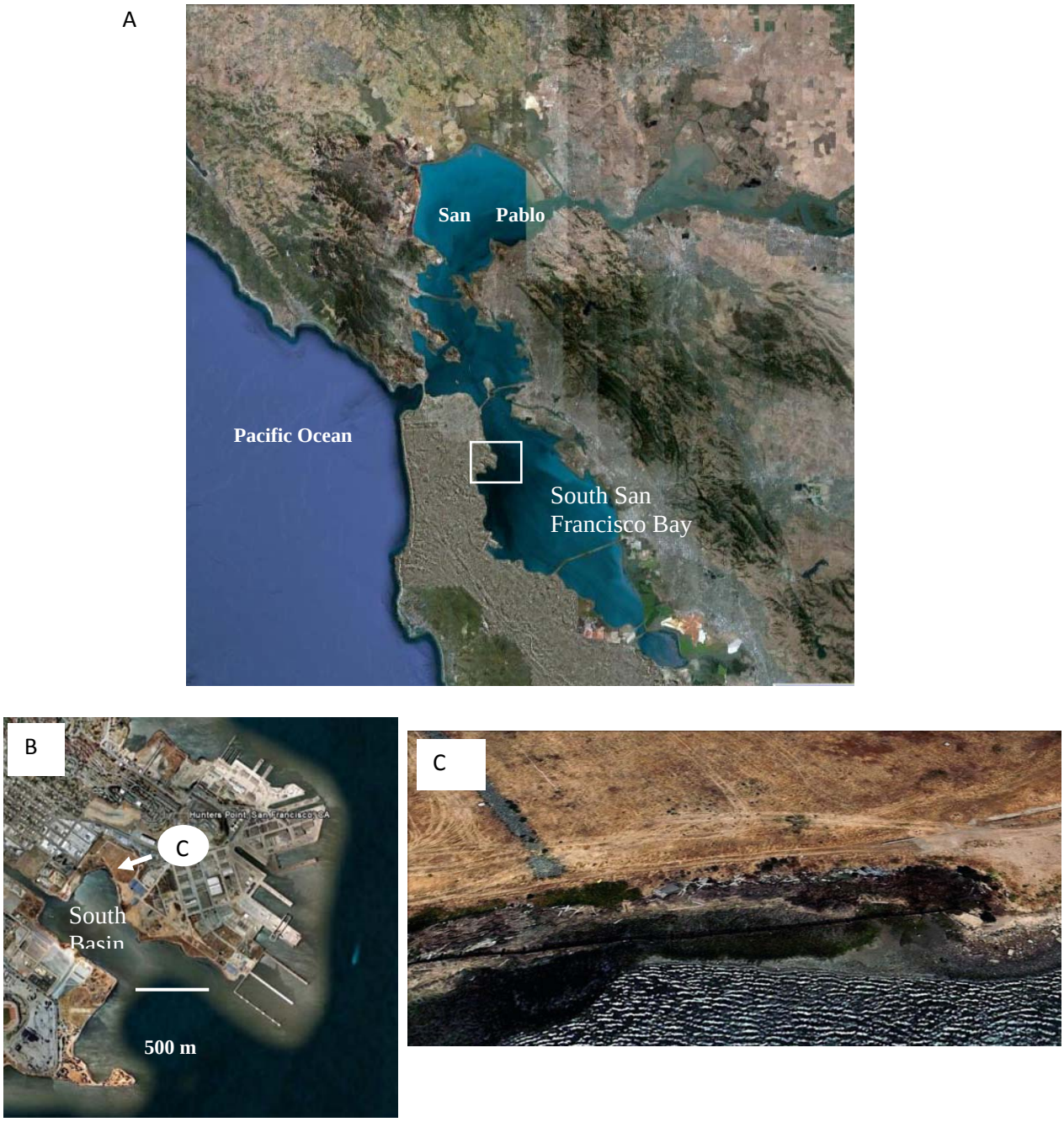

Figure 5.1. The San Francisco Bay and Hunters Point study area. (A) Google Earth© image of San Francisco Bay. The box outlines panel B. (B) Close-up of Hunters Point, showing the location of South Basin. (C) Close-up perspective image of the eastern shore of South Basin. The observations shown in Fig. 28 were taken in the center of South Basin.

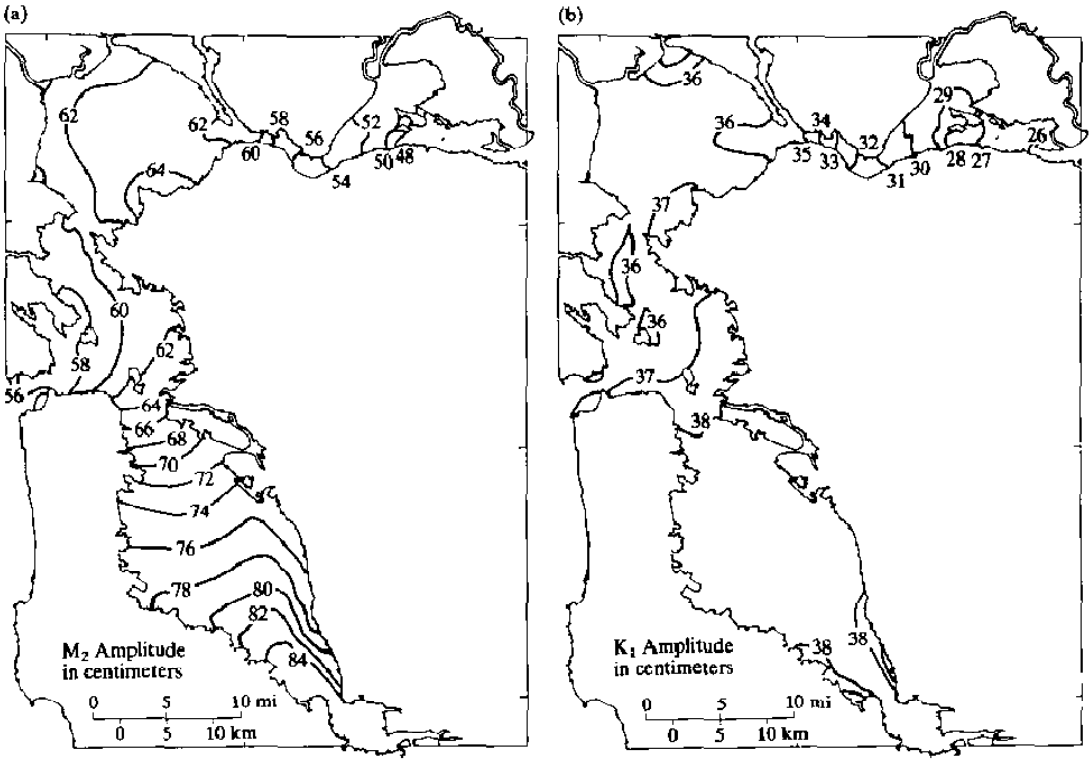

Figure 5.2. Co-range charts (constant amplitude contours) of tides for San Francisco Bay: (A) M_2 tide and (B) K_1 tide (Cheng, Casulli et al. 1993).

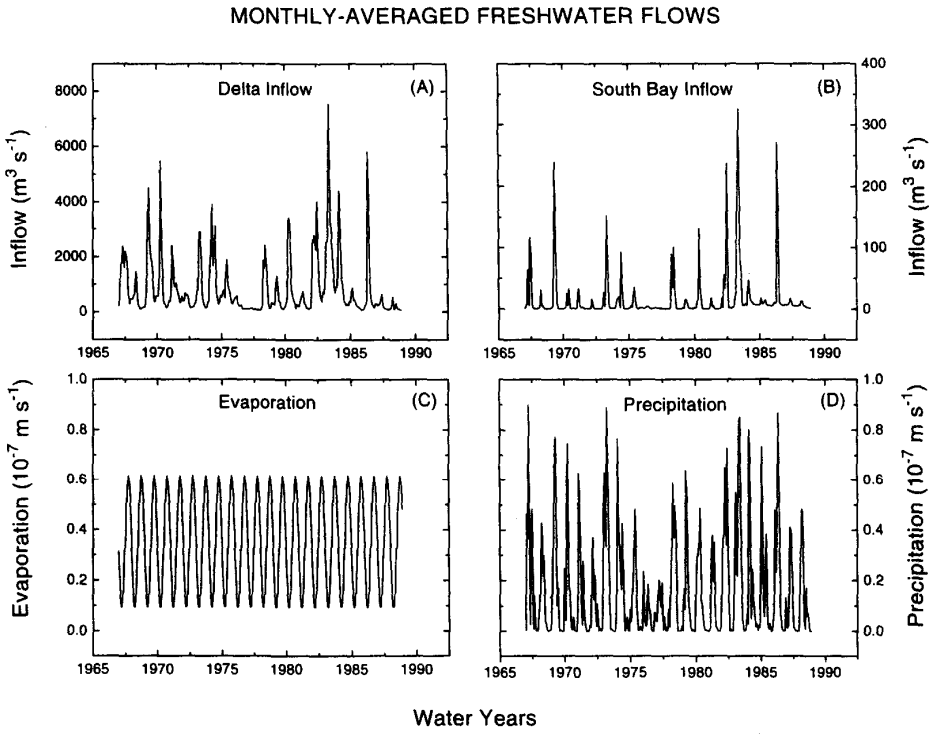

Figure 5.3. Observed, monthly averaged freshwater flows to SFB for water years 1967-1988: (A) Delta inflow ($m^3 s^{-1}$); (B) South Bay inflow ($m^3 s^{-1}$); (C) evaporation rates (taken to be annually repeating in the absence of long-term measured data for the period, units of 10^{-7} m s^{-1}; (D) precipitation rates (units of $10^{-7} m s^{-1}$) (Uncles and Peterson 1996).

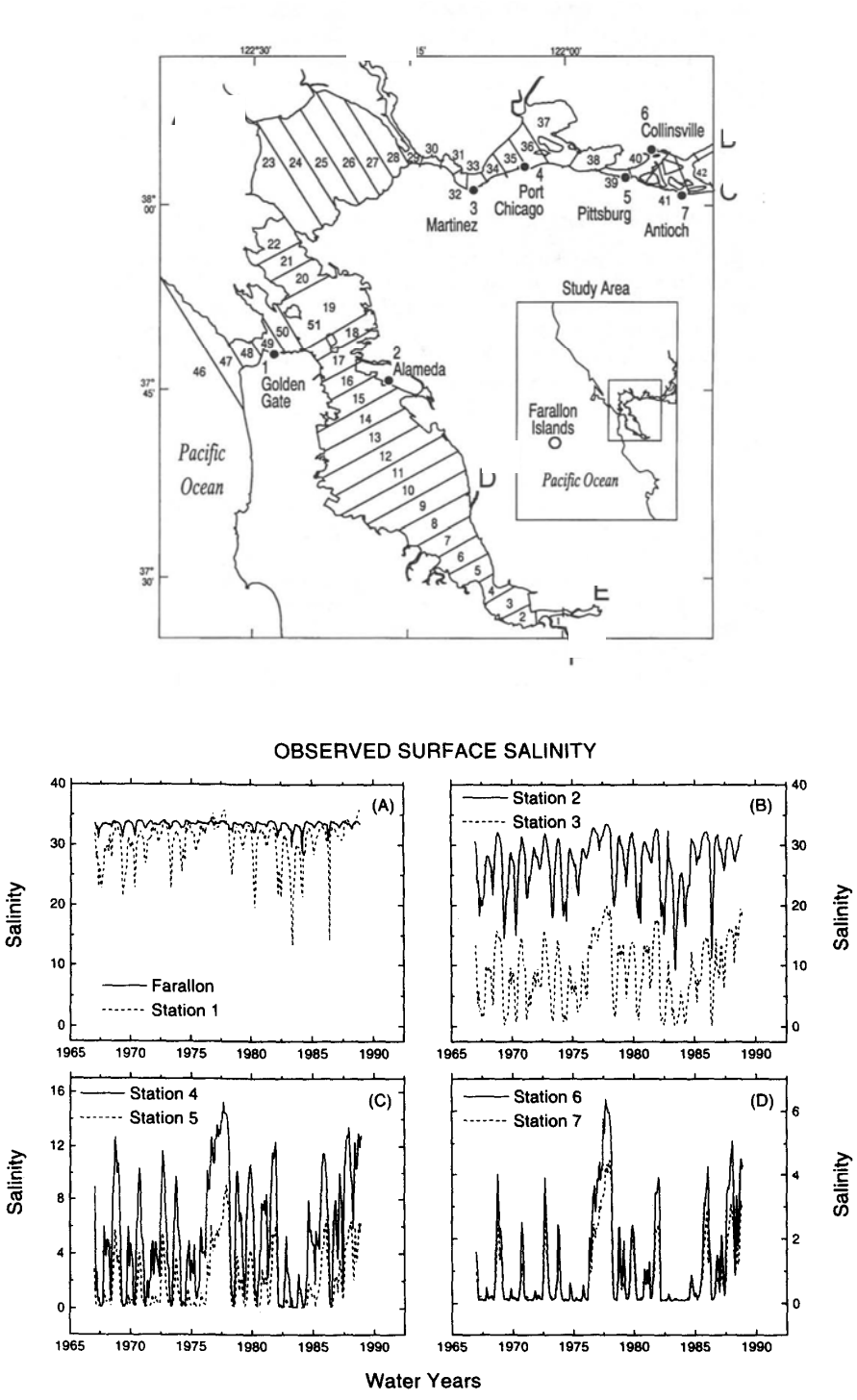

Figure 5.4. UPPER: Map of salinity model segments showing location of stations. LOWER: Observed, monthly averaged surface salinity for water years 1967-1988: (A) Farallon Islands, (solid) and Golden Gate, Sta. 1 (dash); (B) Alameda, Sta. 2 (solid) and Martinez, Sta. 3 (dash); (C) Port Chicago, Sta. 4 (solid) and Pittsburg, Sta. 5 (dash); (D) Collinsville, Sta. 6 (solid) and Antioch, Sta. 7 (dash) (Uncles and Peterson 1996).

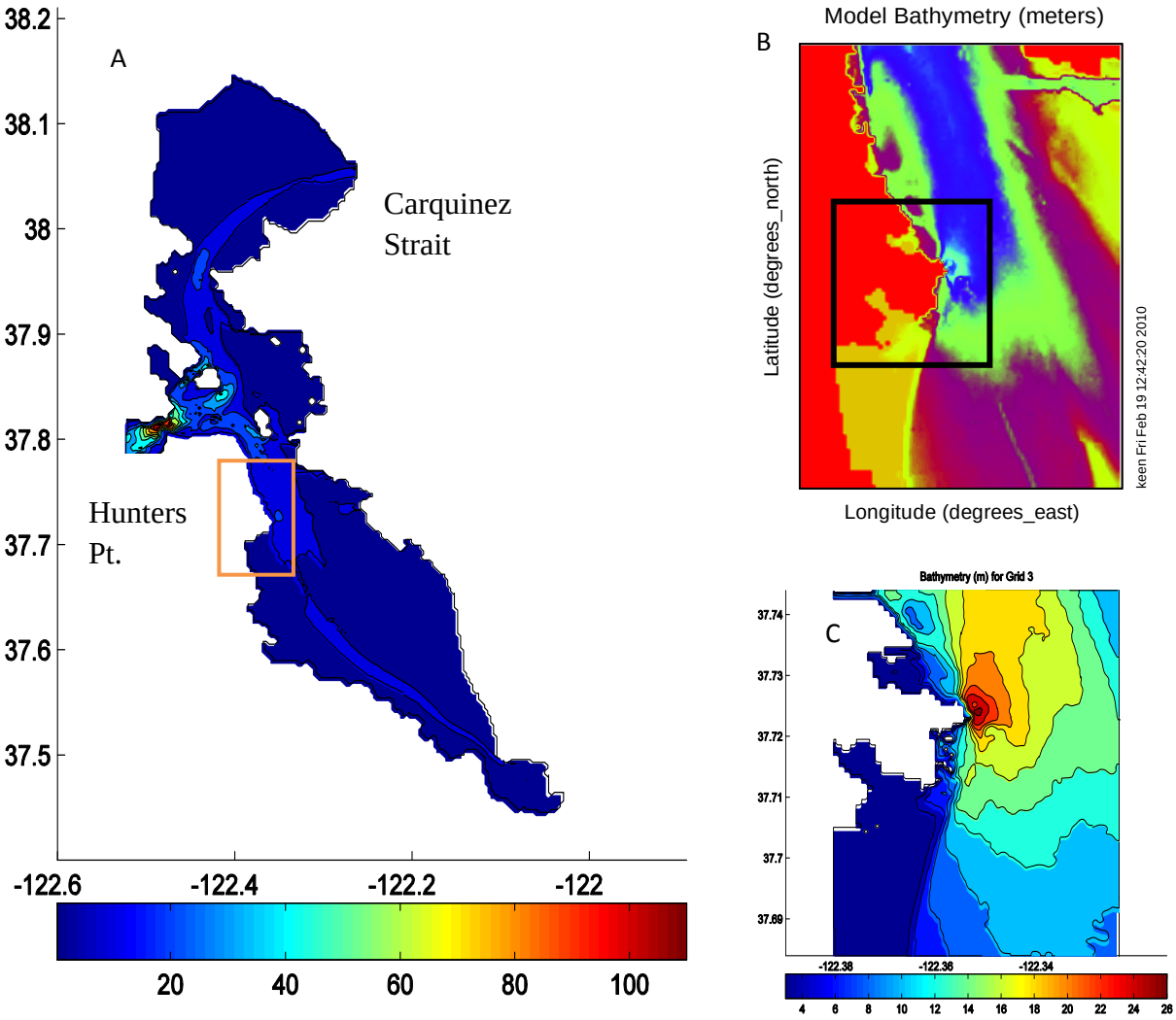

Figure 5.5. Grids used for numerical simulations in this study: (A) the SFB grid with 300 m cells; (B) the Hunters Point (HP) grid with cells 100 m in length; and (C) the SBHP grid with 30 m cells. The box in A indicates the domain of B. The box in B is the SBHP grid in C.

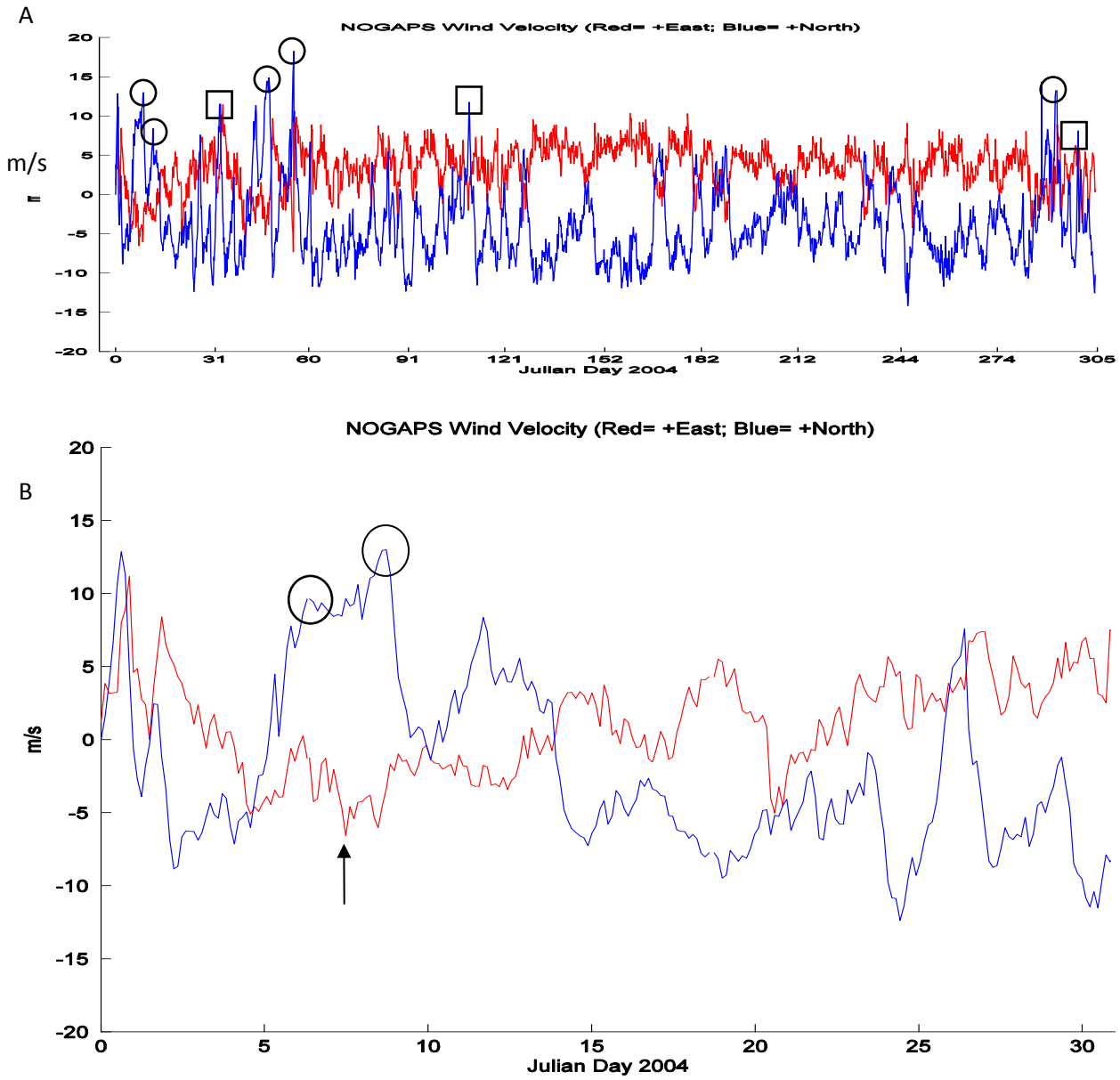

Figure 5.6. (A) Wind speed (m/s) from NOGAPS for 2004 used to force the hydrodynamic models. Circles indicate southeasterly winds and squares represent southwesterly wind events. (B) Detailed record for Jan. only. The red line is the zonal wind (E-W) and the blue line is the meridional (N-S) component. The arrow in (B) indicates 1200 UT on 7 January. The circles in (B) are referred to in the text.

A

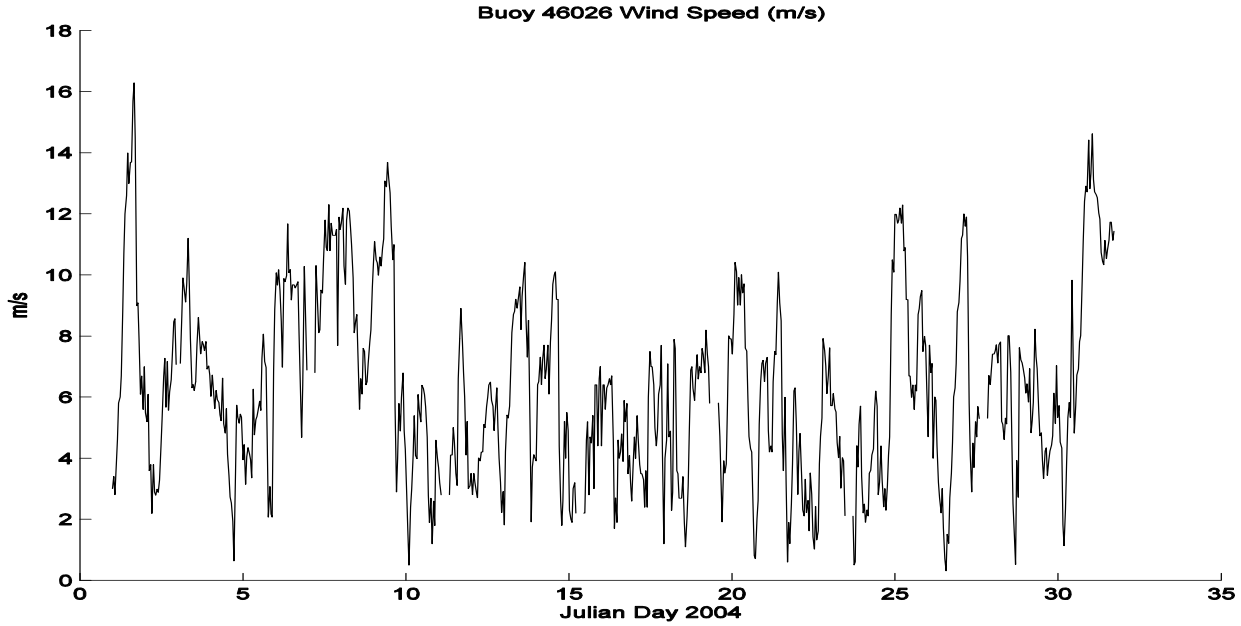

B

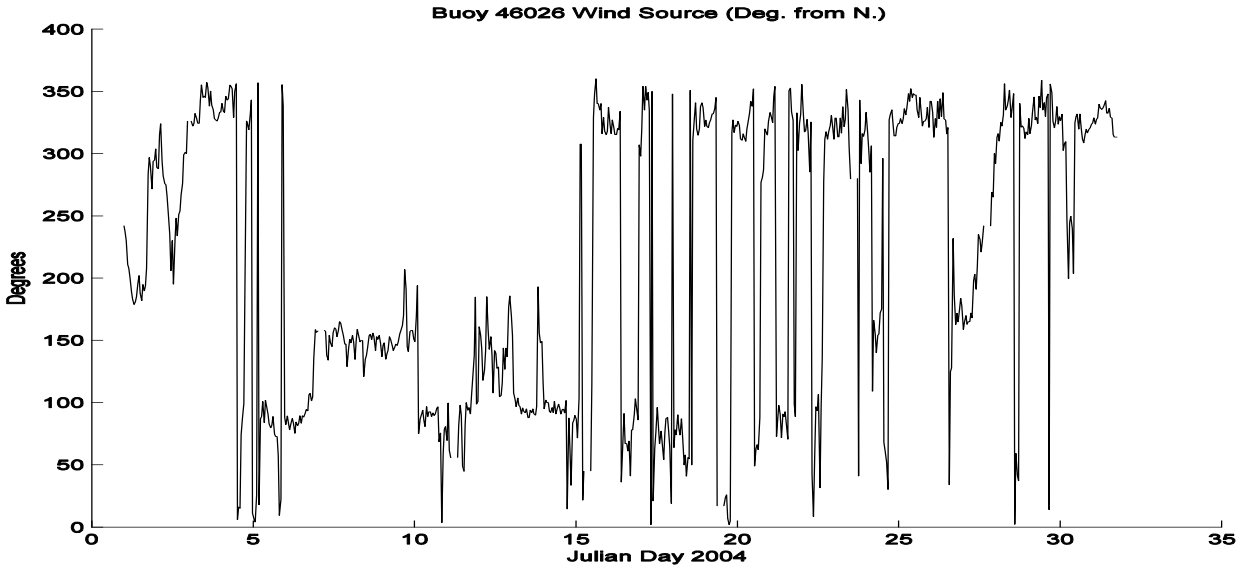

Figure 5.7. Wind speed (A) and direction (B) measured at NDBC buoy 46026 in Jan. 2004. The buoy location is 37.759N, 122.833W.

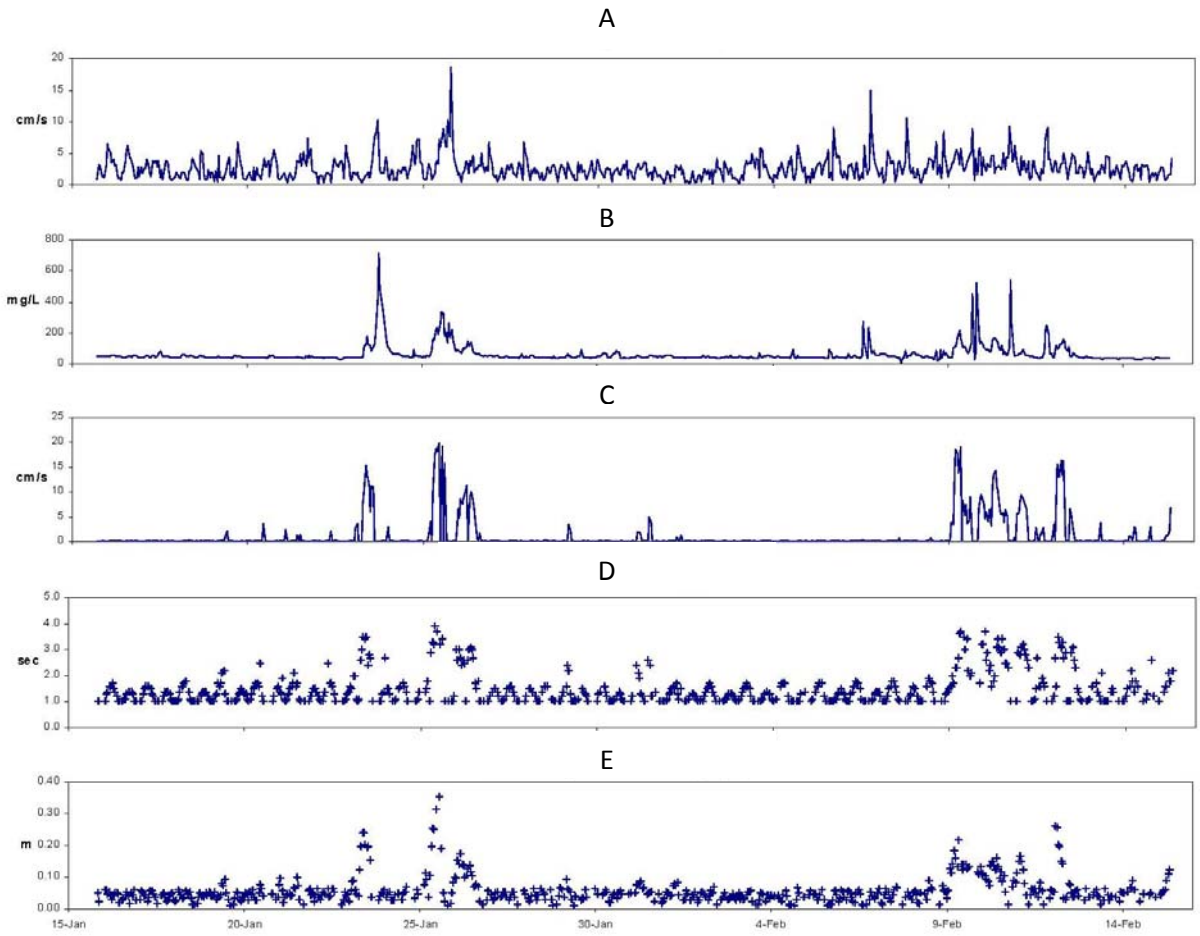

Figure 5.8. Hourly observations from SBHP measured in Jan.-Feb. 2001 (Battelle, ENTRIX et al. 2002). (A) Currents near the bottom (cm/s). (B) Suspended sediment concentration (mg/L). (C) Bottom orbital velocity (cm/s). (D) Wave period (sec). (E) Significant wave height (m). See Fig. 5.1B for location.

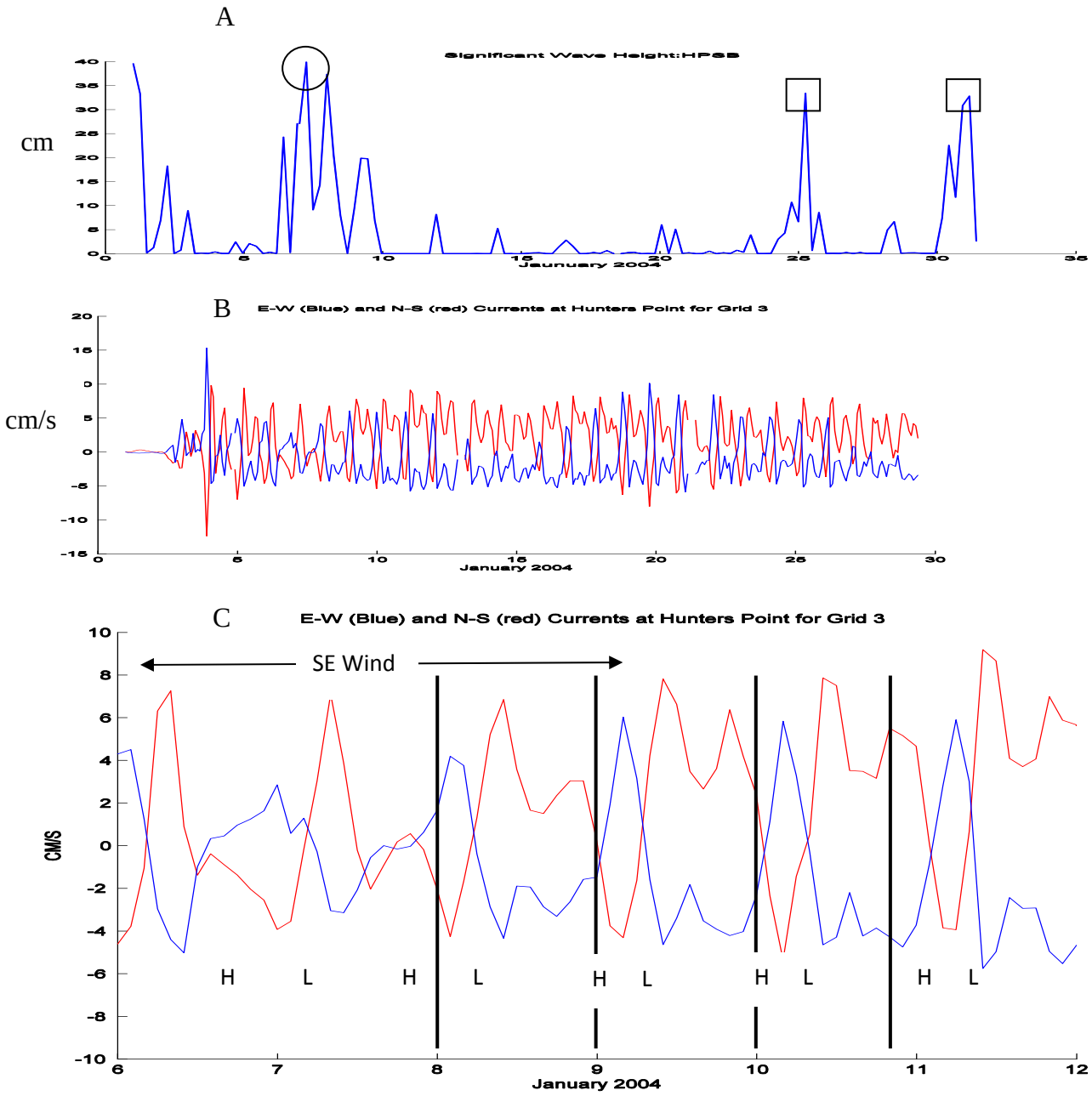

Figure 5.9. Model predictions in Jan. 2004: (A) significant wave height (cm) from SWAN; and (B) currents (cm/s) in SBHP computed by NCOM. The circles and squares indicate waves generated by southeasterly and southwesterly winds, respectively. (C) Subplot from panel B of currents between 6 and 10 January. The blue lines in B and C are the zonal currents and the red lines are the meridional currents. Note that high water occurs ≈ 50 min. later each day (Cheng, Casulli et al. 1993). Key: the solid vertical lines in C are times shown in Fig. 5.12; H = high water; L = low water.

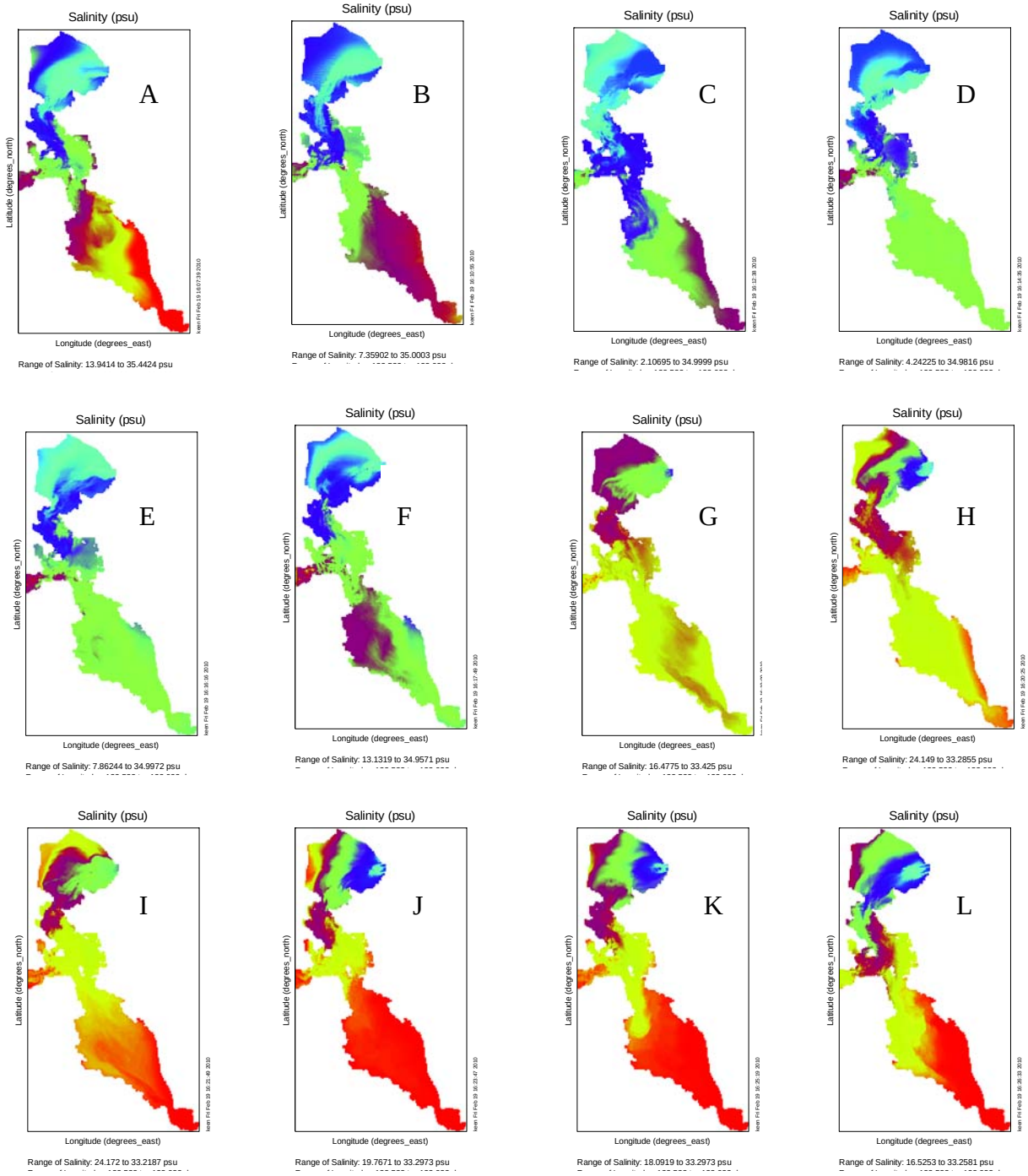

Figure 5.10. Monthly surface salinity maps from NCOM on the 300-m grid. (A) Jan., min/max = 14/35 psu. (B) Feb., min/max = 7.4/35 psu. (C) Mar., min/max = 2.1/35 psu. (D) Apr., min/max = 4.2/35 psu. (E) May, min/max = 7.9/35 psu. (F) Jun., min/max = 13/35 psu. (G) Jul., min/max = 16/33 psu. (H) Aug., min/max = 24/33 psu. (I) Sep., min/max = 24/33 psu. (J) Oct., min/max = 20/33 psu. (K) Nov., min/max = 18/33 psu. .(L) Dec., min/max = 16/33 psu. Dark blue represents minimum salinity and dark red is the maximum in each panel.

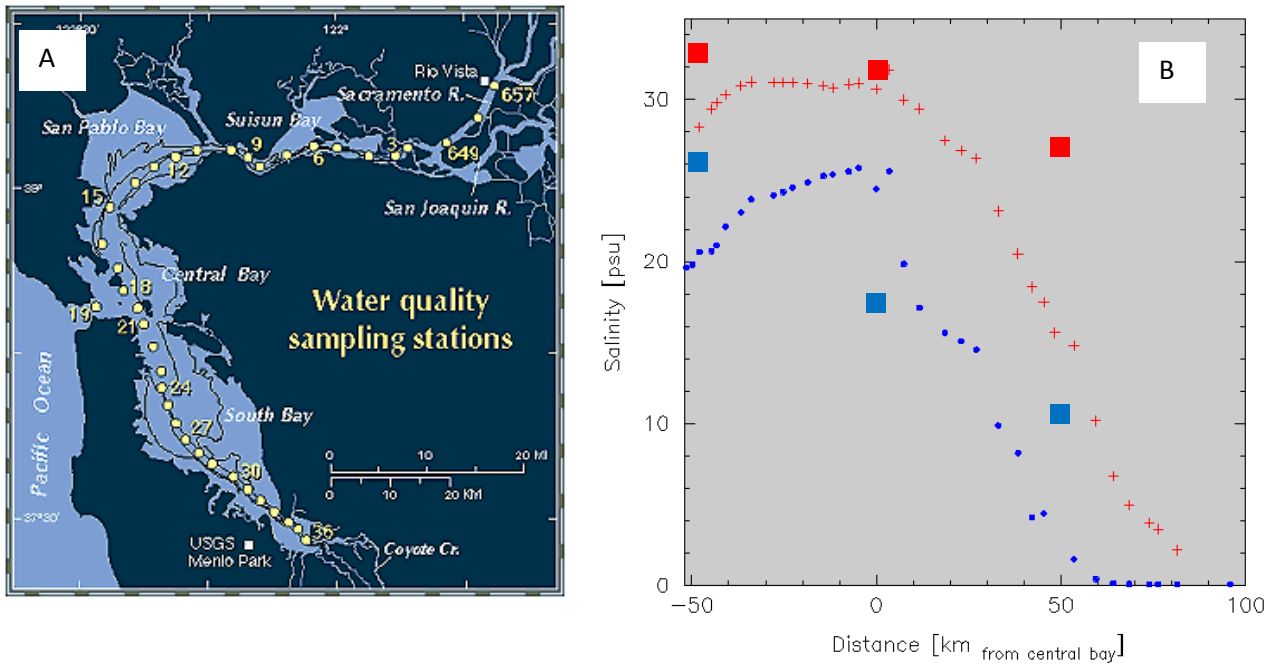

Figure 5.11. (A) Map of San Francisco Bay, showing the sampling stations used for U. S. Geological Survey hydrographic cruises. The stations are numbered starting from the Sacramento River delta. (B) Plot of measured salinity along the axis of San Francisco Bay on 10 Feb. 2004 (•) and 14 Sep. 2004 (+). Distance is measured from the Golden Gate Bridge. Negative values are in South San Francisco Bay. The figures are courtesy of the U.S. Geological Survey. Carquinez Strait is at 50 km (station 9). The squares are the surface salinity from NCOM on the SFB grid.

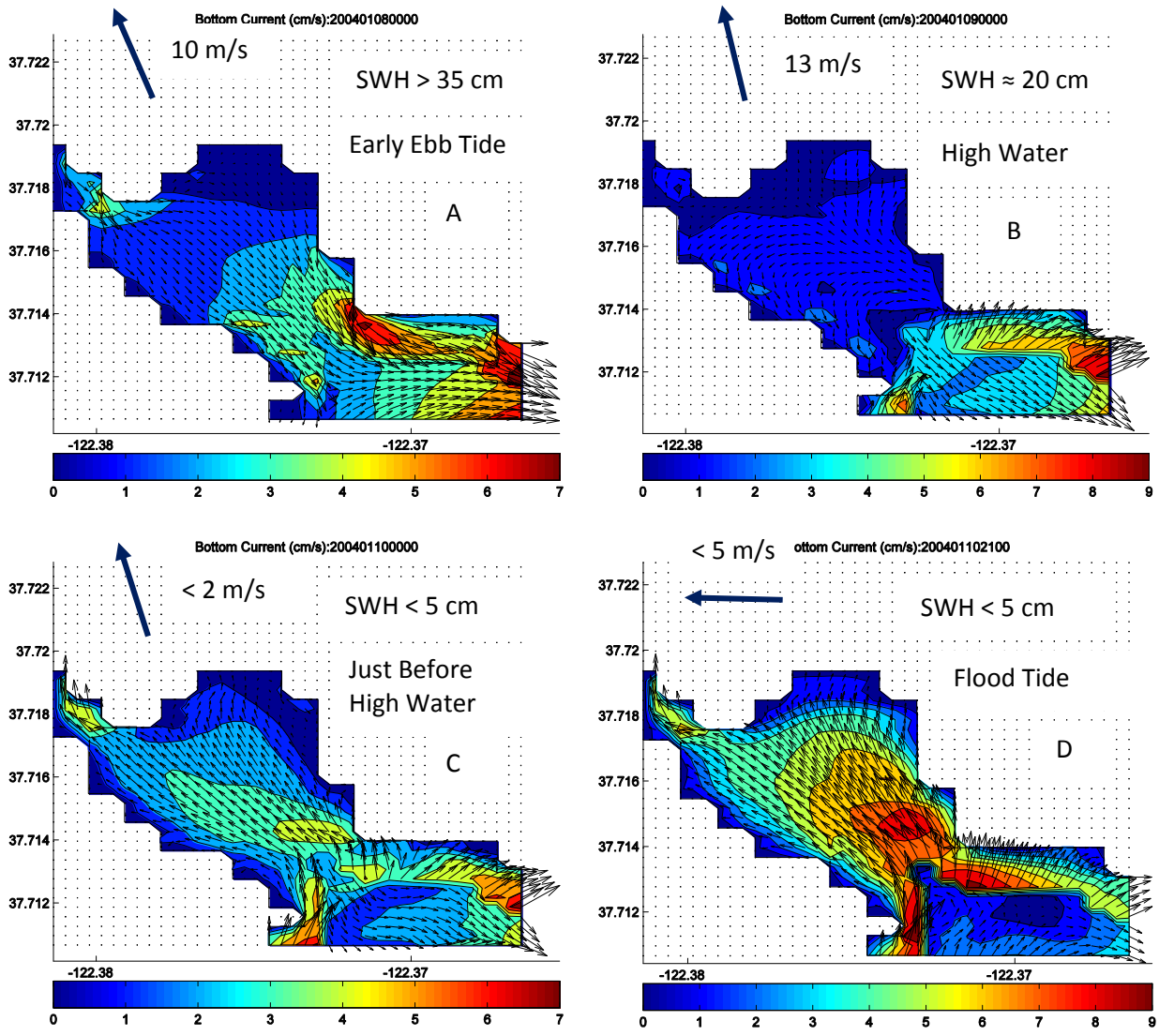

Figure 5.12. Near-bottom currents predicted by NCOM on the 30-m grid in SBHP. The panels show the wind direction and speed (large arrows with annotation) and significant wave height predicted by SWAN at ~24 hr intervals: (A) 0000 UT 8 Jan.; (B) 0000 UT 9 Jan.; (C) 0000 UT 10 Jan.; and (D) 2100 UT 10 January.

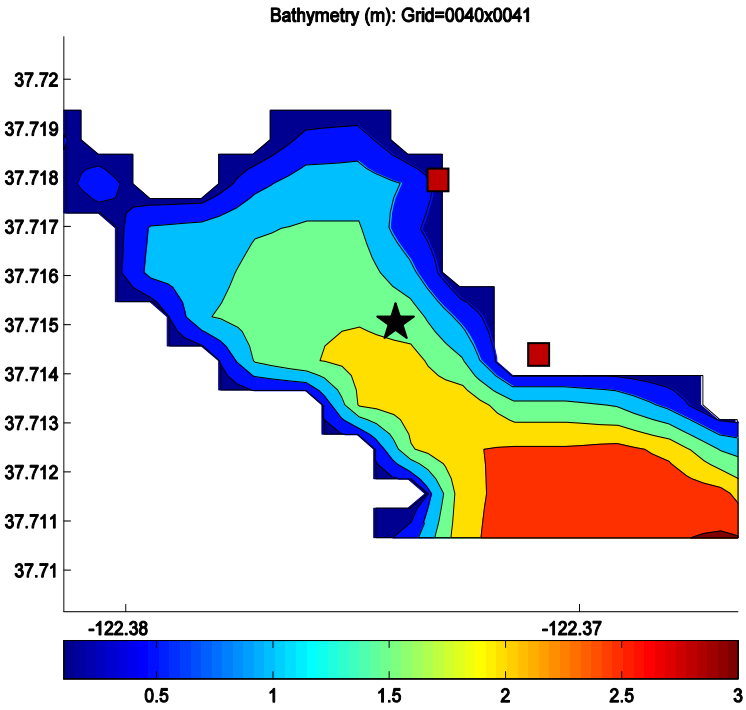

Figure 5.13. Close-up of the gridded bathymetry in the south basin used for the SBHP domain with a cell size of 30 m. For application to NCOM, a minimum depth of 2 m was used. The sedimentation model used the actual depths. The star indicates the location of the BBLM output in Figs. 34 and 35. The red squares indicate the location of point sources used in the HQCM tracer simulations.

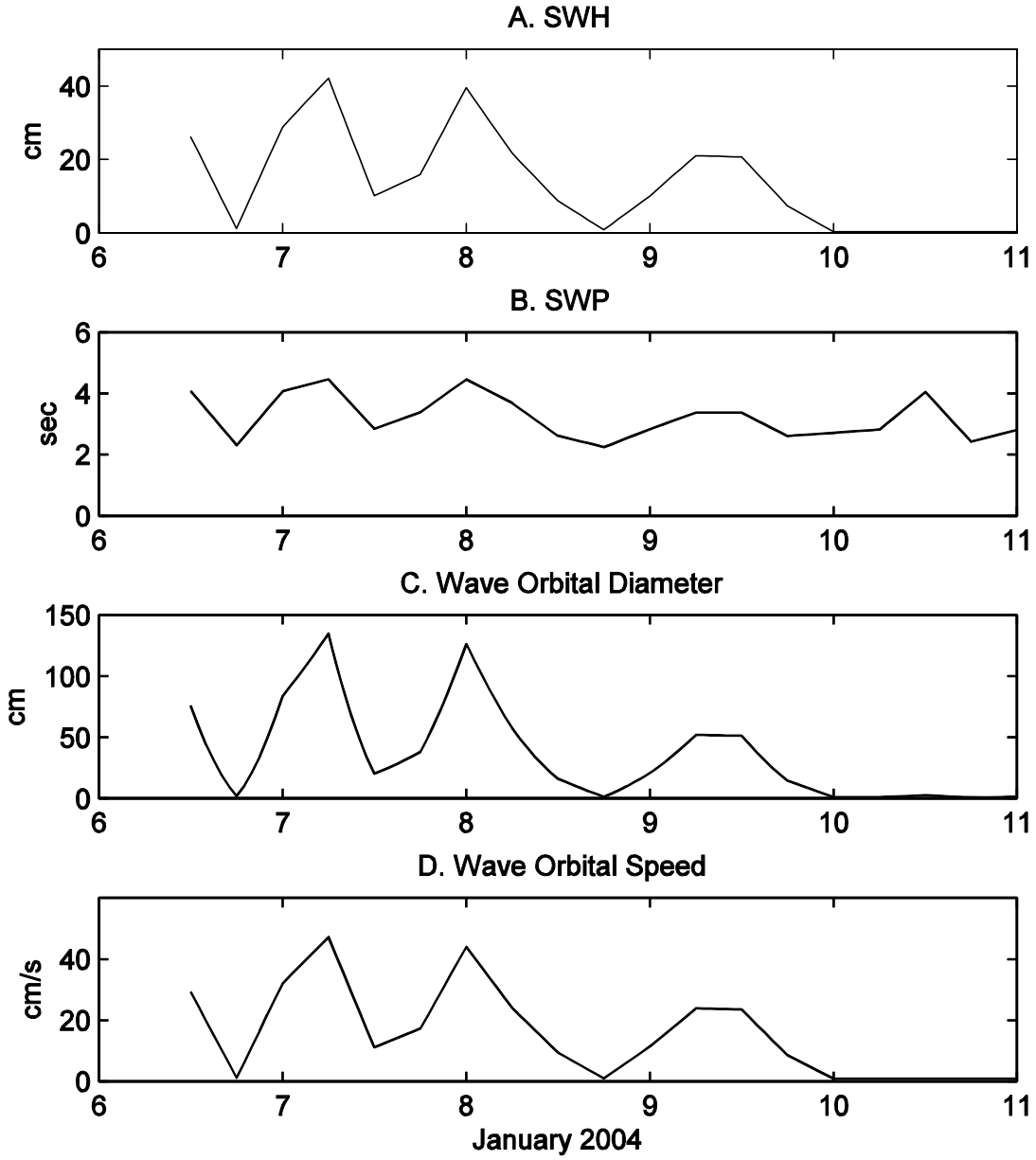

Figure 5.14. Wave parameters used in the BBLM for sediment entrainment. The water depth at this location (18, 107) is 1.82 m. See Fig. 33 for the location of this cell.

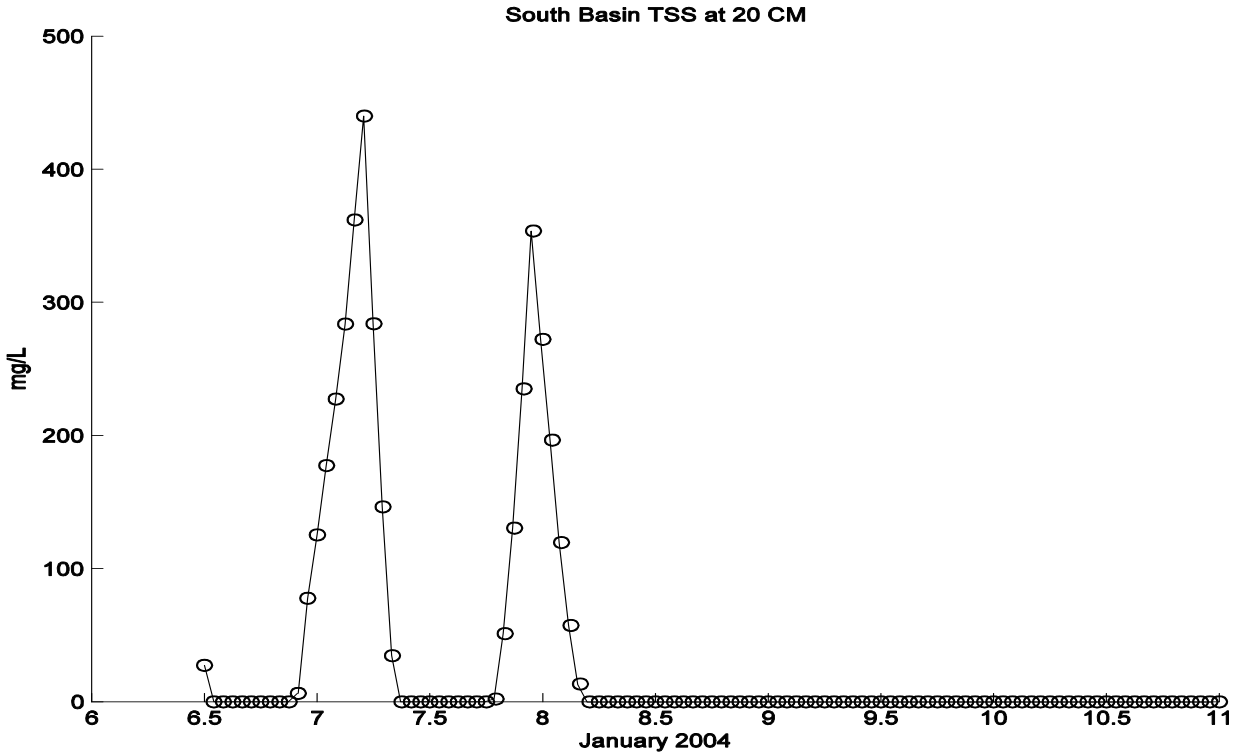

Figure 5.15. Hourly Total Suspended Sediment (TSS) 20 cm above the bed computed by LSOM at grid point (18, 107). Water depth = 1.82 m. See Fig. 33 for location. The entrainment function used the following parameters: $\gamma = 0.43$ and $\gamma_0 = 0.0005$ (Keen and Stavn 2000).

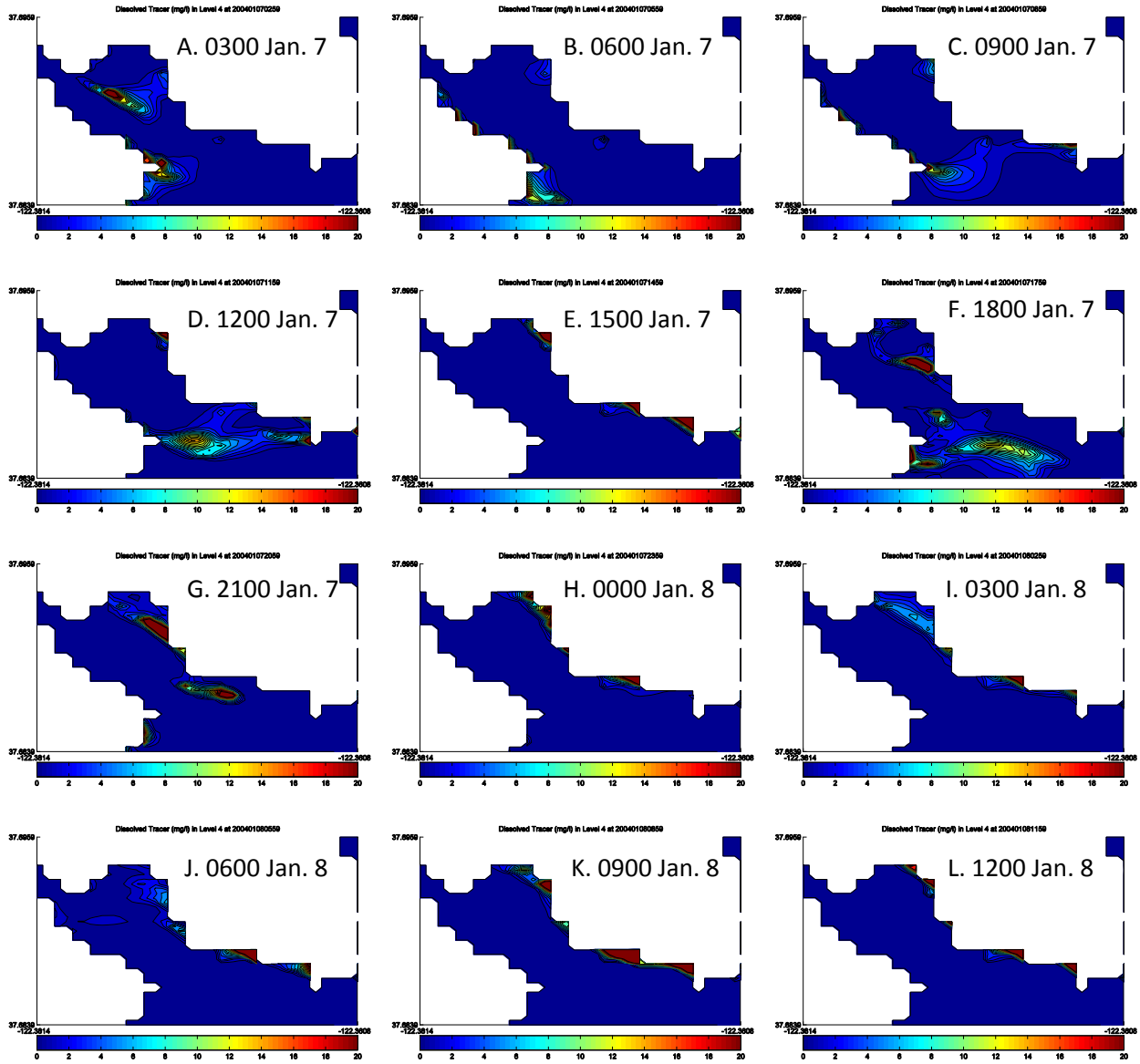

Figure 5.16. Snapshots of surface tracer concentration at 3-hr intervals computed by HQCM on the SBHP grid for 7-8 Jan. 2004. The forcing fields are from NCOM on the 30-m grid (SBHP). Point sources were located along the eastern shore as indicated in Fig. 5.13.

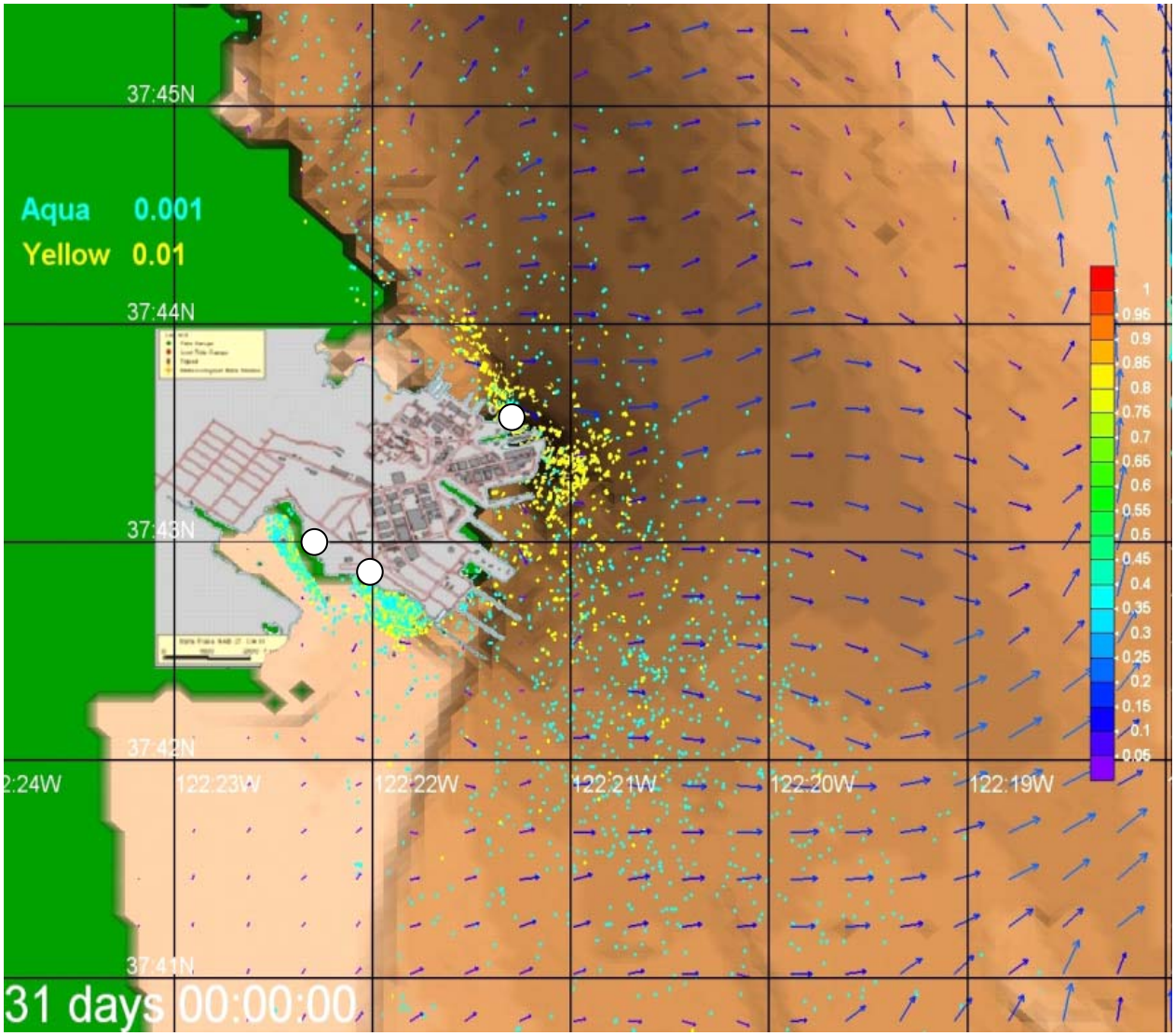

Figure 5.17. Particle distributions near Hunters Point computed by a particle tracking algorithm (Keen, Ko et al. 2006) for Jan. 2004. Particles were released at the locations indicated by the circles. The aqua particles have a settling speed of 10^{-3} mm/s, which is representative of fine clay flocs and particles. The yellow particles have a settling speed of 10^{-2} mm/s, which is more typical for large flocs and silt. The bathymetry is represented by shading. The vectors are the surface currents calculated by NCOM on the 30-m grid. Current speed (m/s) is indicated by shading as shown on the colorbar.

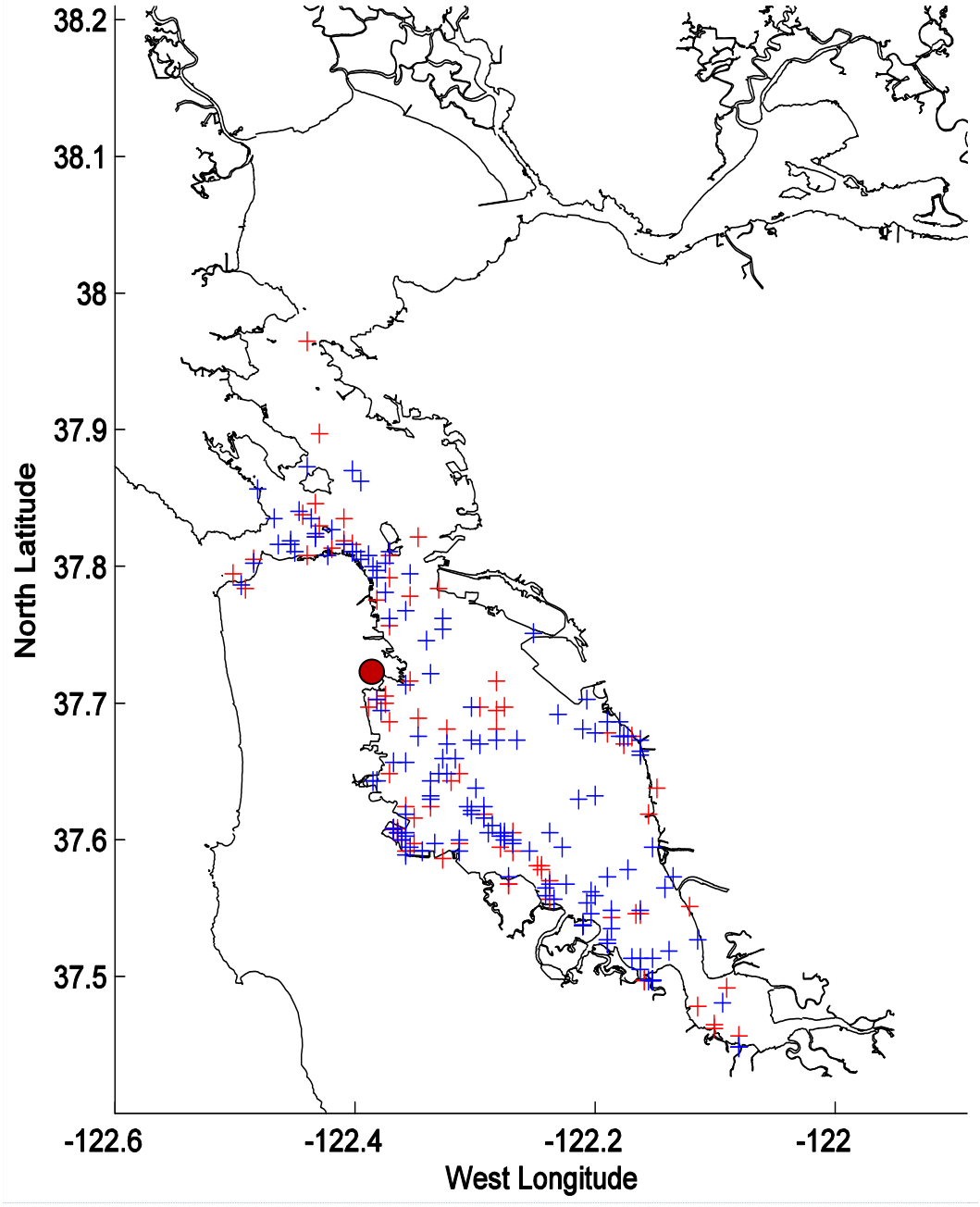

Figure 5.18. Particle distribution in San Francisco Bay after 15 days (red pluses) and 28 days (blue pluses) for Feb. 2004. The hydrodynamic forcing is from the NCOM SFB grid (300 m). One particle was released every 24 hr just south of HPS (red circle).

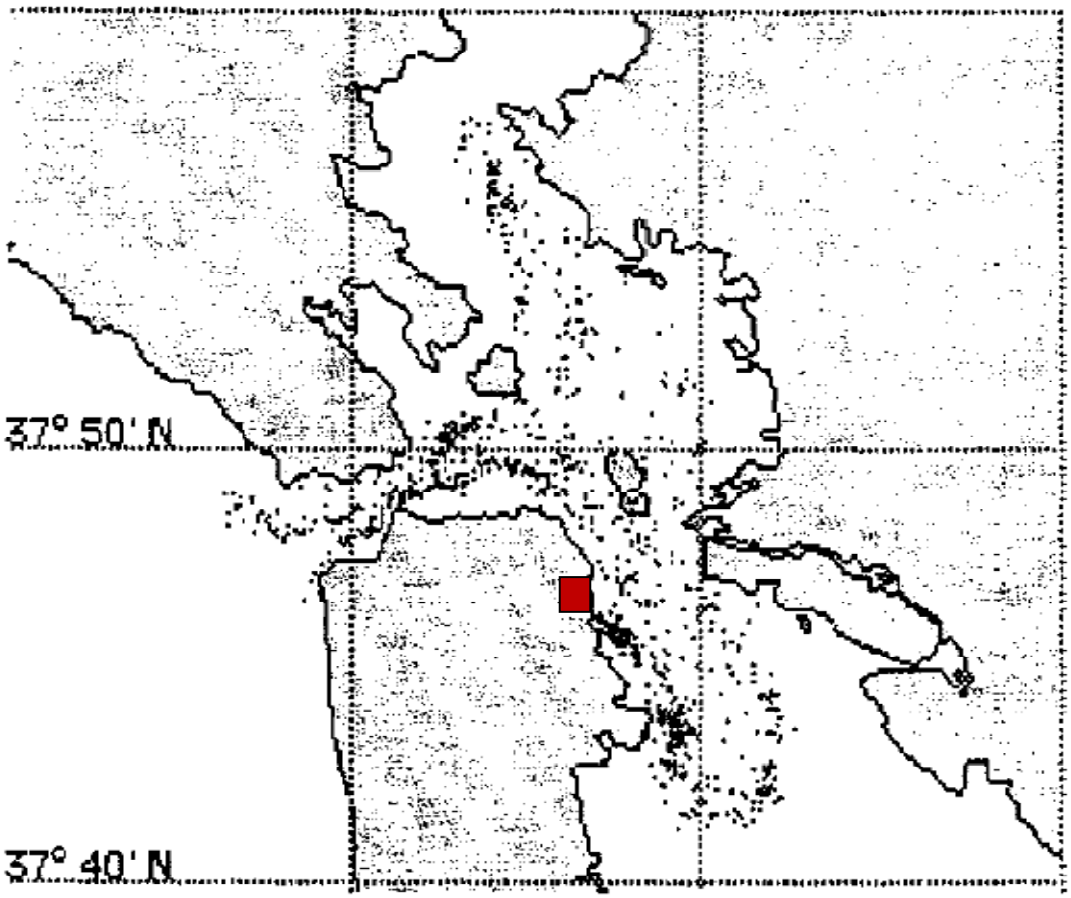

Figure 5.19. Predicted oil distribution on Oct. 30, 1996 from the TRIM2D circulation model on a 250 m grid (Galt, Cheng et al. 1997). The approximate source of the oil is indicated by the red square.

6 Estuarine circulation and mass transport in St. Louis Bay and Mississippi Sound

Mississippi Sound is a compound estuarine area bounded by Mobile Bay on the east, Lake Borgne to the west, and a barrier island chain to the south (Perry 1998). As much as 90% of the fresh water entering the sound comes from the Pearl and Pascagoula Rivers; additional inflow enters through St. Louis and Biloxi Bays (Eleuterius 1978). Mississippi Sound is typically partially to well-mixed due to tide and wind action. It is a heterogeneous sedimentary environment; fine sand comprises the barrier islands and is found dispersed near river mouths whereas clay and silt are dominant in the central parts (Priddy, Crisler et al. 1954). Oyster reefs are widely distributed within the sound and its adjoining bays (Eleuterius 1977) and a benthic community is well established (Mcbee and Brehm 1982; Supan 1983; Valentine 1991; Perry, Eleuterius et al. 1995; Kim, Park et al. 2008). Overall, Mississippi Sound is a healthy estuary with natural events causing the most concern for the ecosystem. St. Louis Bay (SLB) is located within central Mississippi Sound (Fig. 6.1). It receives fresh water from the Jourdan and Wolf Rivers; peak discharges of ~300 and ~600 m^3/s, respectively, occur in spring and minima of 40 and 80 m^3/s occur in summer (unpublished data).

The motivation for studying the Mississippi Sound estuary system (Fig. 6.1) is based on several characteristics that it shares with other environmentally stressed estuaries (McCreary, Twiss et al. 1992; Martinho, Viegas et al. 2008). Mississippi Sound has a large shellfish industry (Mcbee and Brehm 1982; Chigbu, Strange et al. 2006) and its wetlands serve as a hatchery for marine and freshwater fish (Overstreet and Heard 1982; Hoffmayer and Parsons 2003; Franks, Hendon et al. 2004; Ross, Slack et al. 2009). Freshwater input is variable at seasonal and decadal time scales and thus the environment is sensitive to perturbations (Chigbu, Gordon et al. 2004; Bianchi, DiMarco et al. 2010). Furthermore, many subareas within its boundaries are subject to typically low-energy hydrodynamics throughout much of the year, but with episodic flow events that can substantially alter their properties (Blumberg, Ahsan et al. 2000; Cobb and Blain 2002; Keen and Harding 2008). This region has a growing population, and a history of contamination by both point and distributed sources (Lytle and Lytle 1983; Liu, Kingery et al. 2008). Harmful algal blooms have also appeared episodically (Perry and Mclelland 1981).

The primary contaminant of historical interest within the waters of the sound and its adjacent bays is fecal coliform, which is introduced from the many creeks and streams that form the watershed (Liu, Kingery et al. 2008). The transport and distribution of this excess nutrient is also sensitive to atmospheric and oceanographic factors (Chigbu, Gordon et al. 2004; Ufnar, Ufnar et al. 2006; Liu, Kingery et al. 2008; Liu, Hashim et al. 2010). For this reason, there has been increased interest in understanding estuarine transport processes (Runner and Floyd 2002; Dortch, Zakikhani et al. 2007). A relatively new source of contaminants is associated with the industrial facilities constructed on the estuary's bays. These point sources have caused an increase in anthropogenic toxins in sediments and shellfish (Lytle and Lytle 1982; Lytle and Lytle 1983). The anthropogenic contaminant load in SLB was small before the construction of a

titanium dioxide refinery on the north shore of SLB (see Fig. 6.1) (Lytle and Lytle 1982). A more recent survey suggests that these toxins have increased by as much as 100 times in shellfish from the bay (Elston, Cake et al. 2005).

This study was undertaken to evaluate the feasibility of simulating the hydrodynamics and mass transport within estuaries using non-specialized models. These simulations thus represent the kind of effort that can be undertaken at minimal expense and with the least amount of site-specific knowledge. This approach has been successfully applied to oil spill prediction using operational or near-operational models (Ko, Rowley et al. 2005; Castanedo, Medina et al. 2006).

6.1 Background

This work was initiated to investigate the transport of terrigenous material in coastal regions in a manner analogous to that for the Gulf of Papua (Keen, Ko et al. 2006) but at smaller scales. The HQCM model was used in order to quantify the concentrations if possible. This is not easily done with Lagrangian particle tracking models. The objectives were expanded to include the potential application to the remobilization of contaminated sediments as in San Francisco Bay. Thus, there are two aspects to this problem: (1) the circulation field in the estuary system; and (2) the behavior of the toxins in the sediment and water column.

6.1.1 Circulation in Mississippi Sound and St. Louis Bay

Detailed observations of water level and current data within the MSB have been used to analyze the tides (Seim, Kjerfve et al. 1987). The diurnal tide is partly explained by reflection of the tidal wave propagating normal to the coast. Consequently, the period of the K_1 tide is equal to the inertial period in the region. The resulting diurnal shelf currents are Sverdrup waves with typical speeds of 5-10 cm/s. The tidal wave is transformed into a rectilinear shallow-water wave within the sound and the semidiurnal currents are enhanced by the tidal inlets. The tidal waves become increasingly progressive within MSE because of bottom friction.

The northerly winds after cold fronts drive MSE water through the inlets into the MSB, where it flows westward until it enters Chandeleur Sound between Ship Island and the northern end of the Chandeleur Islands (Schroeder, Huh et al. 1985; Crout, Diercks et al. 2001). This cold water flows southward and piles up within Breton Sound, eventually generating a narrow high-velocity flow (squirt) that enters the Gulf of Mexico near the Mississippi River mouth (Walker 1996; Walker, Huh et al. 1996; Morey, Martin et al. 2003).

A forecasting system was developed for the MSB region as part of the NGLI (Northern Gulf of Mexico Littoral Initiative) (Ahsan, Barron et al. 2001). This model was calibrated with available tidal and remote sensing data. The results suggest that bottom friction is the reason for the significant phase difference in the tide between MSE and the open water of the MSB. Fresh-

water inflow from Biloxi and St. Louis Bays is transported westward by a combination of Coriolis and tidal influences (Blumberg, Ahsan et al. 2000). Forecast currents for Apr. 2002 indicate the existence of strong southward flow near the Mississippi River delta to the west and a persistent anticyclonic eddy (CW) in the SE part of the MSB (Blumberg, Ahsan et al. 2002). The model predicts that the salinity difference between the surface and bottom can reach 25 psu during high-runoff events in the spring (Ahsan, Blumberg et al. 2001).

The relative contribution of tide, wind, and river forcing within the MSB has been discussed using a model system being developed at NRL (Blain and Edwards 2002). These results suggest that the tide is dominant within the MSE but the prefrontal southerly winds have an increased effect in more open water. The tidal currents within the MSB appear to be strongly influenced by bathymetry in shallow areas and highly correlated with the boundary forcing in open water and passes. This is consistent with both observations and other model results. The model also suggests that St. Louis Bay is flushed in 15–30 days by large inflow events. Simulations with a coupled current-wave model system demonstrate the generation of variable alongshore currents and wave heights at the entrance to SLB over a tidal cycle (Cobb and Blain 2002). That study used waves with a period of 10 s and a height of 50 cm, which are common during prefrontal winds in this region (Corson, Rhee et al. 2002). The predicted generation of eddies near the bay entrance is reasonable for these waves.

Measurements and numerical model predictions are consistent in demonstrating the sensitivity of local water level and currents to changes in wind direction within the tidal inlets (Keen 2002). The tidal flow within Cat Island Channel in the western sound is strongly asymmetric, with a net flow into Chandeleur Sound and the Gulf of Mexico. The modeled waves, water levels, and currents further demonstrate the importance of their relative timing with respect to alongshore flow and coastal erosion. The general trend of westward transport within the sound by northerly post-frontal winds extends to the sound side of the barrier islands (Keen, Stone et al. 2003). Both measurements and model results show the importance of westward flow by flood tides, northeasterly winds, and waves in very shallow water. The persistence of this flow regime is substantiated by the continued erosion of specific sites in Mississippi Sound and other locations in the northern Gulf of Mexico (Chaney and Stone 1996; Stone and Stapor 1996; Stone G. W. 1998; Stone 1998).

The final component of the flow regime in the MSB is the episodic circulation and flushing caused by tropical cyclones. Simulations of Hurricane Camille indicate maximum currents of 2 m/s into MSE east of Ship Island as the storm approached, which formed a westward flow within the sound (Bentley, Keen et al. 2002). The ebbing storm surge then drove a seaward flow back through the inlets with a strong eastward component within the MSB. A hurricane from 1947 had a more westward track and passed over Breton Sound (Keen, Bentley et al. 2004), which increased seaward flow over and between the Chandeleur Islands. Both of these storms drove westward flow within Mississippi Sound because of the easterly winds that are

found on the right side of the storm's eye. The primary difference between their flows is the location of the maximum currents, which typically occur at the point of landfall (Keen and Slingerland 1993; Keen and Glenn 1999). The existence of the Mississippi delta acts to divide the northern Gulf of Mexico into eastern and western halves, and cause Breton Sound to be the focal point for westward storm flows within the MSB irrespective of storm path.

These preceding studies focused on a range of problems and had different motivations and objectives. Two of them were intended to develop operational forecast model systems that would be of immense value for the present study (Ahsan, Barron et al. 2001; Blain and Edwards 2002). These systems are currently unavailable, however, and it is necessary to construct a conceptual model of circulation within the MSE and SLB before proceeding to the present problem. The asymmetry of the tides within the sound is a fundamental source of the net westward drift of currents. This flow is reinforced by both prefrontal SE wind and postfrontal NE winds in the winter and spring. It is also strengthened by the westward storm flows associated with tropical cyclones. Furthermore, a net westward alongshore drift is present within the area because of the persistent southeasterly winds (Cipriani and Stone 2001). The cumulative result of these flow regimes is a westward transport of water and its contents into western Mississippi Sound, Lake Borgne, and Chandeleur and Breton Sounds.

The flow within St. Louis Bay is more problematical because of a lack of observations and model results. Model results indicate the dominance of wave-driven flow near the coast both within and outside the bay (Cobb and Blain 2002). That study also indicates a wave-driven outflow in the inlet center even during flood tide, which has significant implications for mass transport from the bay to the sound at tidal periods.

6.1.2 Anthropogenic toxins in St. Louis Bay

This study does not focus on the geochemistry of toxins in marine sediments or shellfish; therefore, this section will briefly summarize the most important contaminants in SLB and give some examples of their prevalence in other locations. This is necessary to demonstrate the importance of understanding the hydrodynamics of a potentially contaminated estuary.

Many of the substances found in polluted waters are termed "heavy metals", which has no formal definition (Duffus 2002). This term can be thought of as consisting of elements that are beneficial in moderate amounts to organisms, including iron, cobalt, copper, manganese, molybdenum, and zinc, but which become toxic in excessive quantities. The most common type of anthropogenic toxins reported from natural water bodies are toxic metals like mercury, which have no known benefit to humans (Chen, Serrell et al. 2008). This group includes normally occurring radioactive material (NORM) whose concentration in the environment can be enhanced by technology (Michalik 2008). These trace metals and radionuclides can be highly mobile in marine environments (Radakovitch, Roussiez et al. 2008). Furthermore, this material is concentrated in estuaries after being transported by rivers (Klavins, Briede et al. 2000;

Karamanis, Stamoulis et al. 2008; Lalah, Ochieng et al. 2008; Saeedi and Karbassi 2008; Wang, Cao et al. 2008). The Mississippi Sound estuary has moderate levels of metals in its sediments and shellfish (Lytle and Lytle 1982; Lytle and Lytle 1990).

Terrigenous sources of sewage waste introduce nitrogen, as well as fecal coliform (E. coli) and cryptosporidium, into estuaries. Nitrogen joins nutrient loading from fertilizers to feed algal communities in the coastal ocean and contribute to harmful algal blooms (Erdner, Dyble et al. 2008) and hypoxia (Bianchi, DiMarco et al. 2010).

Organic pollutants include hydrocarbons, PCB, insecticides, and detergents. They are all anthropogenic and deleterious to the environment (Delle Site 2001). The polychlorinated dibenzofuran (PCDD/F) class of compounds is a byproduct of the production of an herbicide (2, 4, 5-trichlorophenoxyacetic acid) and hexachlorophene (an antibacterial agent used in soap). Both of these compounds are now banned in developed countries (Chaudhary, Hassan et al. 2009). Dioxins are also produced during incineration and the bleaching of wood pulp. All of these sources of dioxin were significantly reduced in the U. S. between 1987 and 2000 (USEPA 2006). The pollutants in St. Louis Bay that were measured in previous studies (Lytle and Lytle 1982; Lytle and Lytle 1983) were probably produced by either pulp processing locations around the bay or the titanium dioxide refinery on the north shore of SLB. It should be noted that refining titanium dioxide produces large quantities of trace metals but it does not directly create dioxins. However, it has been suggested that some dioxins produced during processing may be released from the refinery sewage outfall on an ongoing basis (Elston, Cake et al. 2005).

For the purpose of evaluating the mass transport results from the numerical models, we will focus on the data for dioxin concentration in sediments (Fig. 6.2) from 2001 (Elston, Cake et al. 2005). The concentrations are lowest along the eastern side of SLB (7 pg/g) and slightly higher on the western margin (< 11pg/g). The largest values inside the bay are located near the outfall from the Titanium dioxide refinery (< 12 pg/g). The sediment concentrations decrease to 6-9 pg/g in the inlet before increasing to a max value of 15.33 pg/g SE of the bay inlet. The concentration near Waveland, located 6 km to the west, is < 9 pg/g. These data will be used to evaluate the overall accuracy of the hydrodynamics and mass transport simulations discussed below. The objective is to determine whether the dioxins contained in the sediments of SLB have been transported into the sound and when such transports have potentially occurred.

6.2 Atmospheric forcing in the northern Gulf of Mexico

The NOGAPS (Navy Operational Global Atmospheric Prediction System) was used for wind forcing because this study was designed to examine the potential for using operational forecast products to predict the movement of water-borne contaminants in estuaries. The zonal (E-W) and meridional (N-S) winds measured near the north end of the Chandeleur Islands for 2005 (red lines in Fig. 6.3) reveal the recurrence of northerly winds (meridional component < 0 in Fig. 6.3) during fall to spring. These “cold fronts” are circled for post-frontal northerly winds >

10 m/s in the figure. Only ten events are circled because many do not meet the speed requirement. The buoy was damaged by Hurricane Katrina in Aug. and no data were reported for Sep.-Oct. The forecast wind from NOGAPS (blue lines in Fig. 6.3) has much lower magnitudes but follows the overall trend of the observations. The model also indicates the passage of H. Katrina on JD 243 with an easterly wind of 22 m/s. The following sections will focus on three events from 2005 for which the NOGAPS winds are closer to the observations (Fig. 6.4): (1) a cold front on JD 66-70 (Mar. 7-11); (2) a cold front that passed over during JD 338-343 (Dec. 4-9); and (3) Hurricane Katrina, which made landfall on JD 421 (Aug. 29).

The Mar. cold front is best captured in the meridional winds from NOGAPS (Fig. 6.4B). It is more important to reproduce this component because of the impact of northerly winds on the MSE waters. The predicted zonal wind (Fig. 6.4A) peaks at <5 m/s from the west, whereas the measured wind is easterly while fluctuating between 0 and -10 m/s during the cold front. The buoy wind does not have a westerly component until the wind bearing becomes southwesterly. The simulated wind does not reproduce the details of the cold front but it does capture the fundamental wind reversal from southerly to northerly.

The cold front of early Dec. was somewhat different from the spring event. The northerly wind persisted for several days (red line in Fig. 6.4D) and it was preceded by a strong (>12 m/s) easterly flow (zonal wind < 0 in Fig. 6.4C). NOGAPS completely missed the prefrontal wind (blue line in Fig. 6.4C) but did a reasonable job for the northerly component. Both cold fronts were preceded by southeasterly winds but the northerly wind in Mar. lasted less than half as long as that from Dec.

We will examine the approach of H. Katrina because such strong flows are obviously important for flushing bays during the season of low flow from rivers. The zonal wind for this event (Fig. 6.4E) does not indicate the approach of the storm in either the observations or the model. The meridional wind, however, clearly indicates the inflow associated with a tropical cyclone (Fig. 6.4F). NOGAPS fails to capture this inflow but, instead, predicts a weak northerly wind beginning on JD 238. The reversal in dominant wind origin from easterly to westerly is apparent in NOGAPS because the eye passed directly over the study area and ,as expected, the pre-landfall easterly wind is much stronger.

6.3 Numerical modeling

The dynamics of estuarine flow within St. Louis Bay and Mississippi Sound are being investigated using the nested NCOM models on several grids. A St. Louis Bay model (Fig. 6.1 inset) with a cell size of 80 m is nested within a Mississippi Bight model grid (cell ≈ 900 m), which is in turn nested to the global model (cell size ~ 13 km). Tides are introduced into the MSB grid (Table 2) and allowed to propagate into the SLB grid using its open boundary

condition, which is the same as between MSB and the global model. Both grids receive three-dimensional currents, temperature *T*, and salinity *S* at their open boundaries in addition to water surface elevations η and vertically integrated transports *U* and *V*. The SLB and MSB models are initialized with *T*/*S* fields from global NCOM. Both model grids use a minimum water depth of 2 m. The MSB grid includes mean monthly inflow from the Pearl, Pascagoula, Mobile, Biloxi, Jourdan, and Wolf Rivers (unpublished NRL data).

The transport of dissolved material within the bay and the adjacent sound are being simulated with the HydroQual Contaminant Model (HQCM). Some simulations include both tracer fields and some focus on discrete particles released at the Jourdan and Wolf Rivers. The tracer concentrations were not selected to represent the TEQ values from Fig. 6.2, however. They will be used to interpret the model results qualitatively.

6.3.1 NCOM validation

A tide gauge was installed at the Bay Waveland Yacht Club in Nov. 2005, but the data were not available in time to influence these simulations. Instead, we can compare a tidal cycle from the tide gauge data with available NCOM results for Jan. 2005, which did not include tides in any of the model grids (Fig. 6.5). After adjusting the model data by +20 cm to account for the different reference heights, we see that the phase is good but there is a substantial discrepancy in the tidal elevations. This problem has been noted before (see section 5 in this report). The tidal constituents at the open boundary (Table 2) can be compared to those derived from measurements (Seim, Kjerfve et al. 1987). Typical tidal amplitudes from NCOM (Seim et al) are: O_1 = 14.2 cm (<14 cm); K_1 = 14.4 cm (<15 cm); M_2 = 2.7 cm (<3 cm). Typical phase values are: O_1 = 15° (15°); K_1 = 18° (<25°); M_2 = 103° (<100°). These comparisons suggest that the differences are caused by either the model grid (bathymetry, resolution, and coastline) or bottom friction.

This problem can be explored further by comparing the model-predicted tidal elevations for Jan. 2005 to predictions from the IHO database (Keen 2002) that have been adjusted in time as with the SLB tides above (Fig. 6.6). There should be very little discrepancy due to the IHO data being computed for 1997 because of the dominance of diurnal and semidiurnal constituents. The discrepancy in tidal water level is lowest at Cat Island at the western end of Mississippi Sound (Fig. 6.6A), and on an island in Breton Sound (Fig. 6.6B). The errors at spring tide for these stations ≈10 and ≈20 cm, respectively, whereas the error at Mobile Point is > 20 cm (Fig. 6.6C). The minimum bottom drag coefficient used in these simulations was 0.0025 and the bottom roughness was 1 cm. These values are reasonable but they may be too large for this domain. Better results were achieved with POM using values of 0.001 and 0.64 mm, respectively, for these parameters (Keen 2002).

The water level predictions from NCOM can be compared directly for Nov.-Dec. 2005 at St. Louis Bay (Fig. 6.7), which includes interval (2) to be discussed later. This is a good

comparison because it includes subtidal flow. The most noticeable feature of this plot is that the tides are under-predicted as expected from Figs. 44 and 45. The subtidal elevations are much better, however. There is an increase ≈ 25 cm in the mean value of η between JD 315 and 320. This is followed by a decrease ≈ 40 cm in both the observations and the model. The model predicts η by 30 cm on JD 328 because NOGAPS predicts a westerly component > 5 m/s when the observed zonal wind was easterly at 7 m/s (Fig. 6.4C). This error caused an excessive set-down because the output point is on a coast with an east-west orientation in SLB. The rest of the record follows this pattern. The good performance for a direct comparison within the bay demonstrates the usefulness of the model output for the following discussions. We should keep in mind, however, that the model-predicted tidal flow is probably weaker than it should be.

6.3.2 Tidal circulation

The net effect of the tides can be evaluated using cumulative vectors for Jan. 2005 (Fig 47). These plots were generated by summing the currents at each model cell for 31 days. The cumulative surface currents (Fig. 6.8A) indicate weak outflow along the eastern side of the bay entrance with very little movement to the north or east. A strong southward flow is predicted at the east side of the inlet and the net tidal flow is eastward within the sound. The tide can be seen to bifurcate around Square Handkerchief Shoal (labeled in Fig. 6.8A) and there is a net westward flow at its eastern end. The net bottom flow (Fig. 6.8B) indicates net outflow through the bay entrance. The cumulative flow around the shoal is seen to extend to the bottom with similar magnitudes (~200 cm/s). There also appears to be a net eastward bottom flow near Waveland that is reinforced from within the sound by net NE currents (contoured in yellow). The cumulative tidal currents suggest that mixing within SLB is minimal but that water does exit. The high net southward bottom flow in the center of the bay is probably caused by the confluence of the Jourdan and Wolf channels (see Fig. 6.1 inset).

Because of the cumulative flow indicated for the SLB model, it is instructive to examine the net flow for the entire MSE (Fig. 6.9). The surface net flow (Fig. 6.9A) indicates that the eastward flow seen in the SLB grid does not continue but is actually part of the net flow through Cat Island Channel and into Chandeleur Sound. This cumulative outflow is more extensive at the bottom (Fig. 6.9B). A similar pattern of net outflow is seen through the other barrier island passes whereas the net flow is landward on the northern side of Mississippi Sound. The cumulative flow within Chandeleur Sound is northward, which indicates that the observed transport into Breton Sound is very likely caused by winds alone. There is net southward movement on the gulf side of the Chandeleur Islands, however.

6.3.3 Baroclinic circulation and mass transport during a cold front (March 2005)

The sensitivity of the SLB circulation to the wind forcing during a cold front can be examined using a simulation with no tides, but with the Wolf and Jourdan Rivers. The prefrontal wind on Mar. 5 was southwesterly at 5 m/s (Fig. 6.10A). The predicted surface circulation is

nevertheless southward throughout SLB because of the river inflow. Flow through the inlet is southward at all depths (upper panel in Fig. 6.11A) with the strongest currents in the middle. The salinity ≈1.5 psu less on the west side and the water column is well mixed (lower panel in Fig. 6.11A). This flow regime continues into Mar. 6 (Fig. 6.10B) as the wind weakens and the water becomes somewhat fresher in the inlet (lower panel in Fig. 6.11B). The surface flow remains constant through Mar. 7 (Figs. 49C, D) but the southward currents reach 20 cm/s across the inlet (upper panel in Fig. 6.11D).

The transport of tracers originating at the Jourdan and Wolf Rivers (inflow = 400) was investigated with HQCM beginning on Mar. 1. The tracer is neutrally buoyant and has a decay rate of 0.01 d^{-1}. By Mar. 3, the tracer originating at the Jourdan River on the west side of SLB has reached the mouth (Fig. 6.12A) but it is not widely distributed within the bay. One path taken by the input tracer is along the ship channel. This channel directs tracer to the center of the bay where it is joined by tracer originating at the Wolf River. The simulated distribution changes little during the next 24 hr (Fig. 6.12B). The western tongue separates from the coast near Waveland by Mar. 5 (Fig. 6.12C) where a persistent convergence zone is located and by Mar. 6, this feature begins to form an isolated patch within the sound (Fig. 6.12D). Note also the transport of lower concentrations through the eastern side of the bay mouth. The NOGAPS wind rotates to northeasterly by Mar. 6 (Fig. 6.10A) and the increased surface flow truncates development of the tracer tongue near Waveland (Fig. 6.12E). Instead, a CW eddy develops and focuses tracer at this location. After the postfrontal wind weakens, tracer remains trapped at the coast west of the bay mouth (Fig. 6.12F) and low concentrations are predicted within the sound south of the bay. The tracer becomes concentrated where gradients exist in the transport field. Consequently, surface values are high on the west side of the inlet whereas the bottom value is negligible (Fig. 6.13). This occurs because of upwelling flow along the western side of the bay mouth due to a convergent flow. Within the central inlet, however, the concentration is uniform over much of the water column. A front exists on the eastern side of the inlet with stratification predicted in the shallow water on the eastern shore.

The particle-tracking module of HQCM was also used to examine Lagrangian transport during this cold front. Neutrally buoyant particles were released at the Jourdan and Wolf Rivers at 3-hr intervals. The distribution of particles on Mar. 15 is interesting (Fig. 6.14). The baroclinic flow caused by river input forms two streams along the margins of the bay mouth. It appears the particles from the Jourdan River (blue circles) are more restricted in their transport whereas those from the Wolf River have the potential to be transported eastward within Mississippi sound. A few of the Jourdan particles have been transported past Square Handkerchief Shoal (see Fig. 6.2 for location) by the end of the simulation.

6.3.4 Combined flow during back-to-back cold fronts (December 2005)

The cold front of Dec. 4-9 2005 was simulated using NCOM with winds, rivers, and tides. The NOGAPS prefrontal winds on Dec. 4 set up a 12 cm/s inflow along the eastern side of the bay

mouth (Fig. 6.15A). This flow comprises two surface jets with weak outflow to the west (Fig. 6.16A). The SW wind persists until after high water but has little effect on the outflow during the following ebb tide (Fig. 6.15B). This flow is uniform across the inlet (Fig. 6.16B). The wind continues to weaken until low water and a northward jet forms in central SLB (Fig. 6.15C). The inflow is strongest on the west side of the bay mouth and a weak outflow is predicted at the bottom (Fig. 6.16C).

The forecast wind has become northerly by 1200 UT on Dec. 5 (JD 339.5) and it drives an outflow just before the ebb tide (Fig. 6.15D). The resulting outflow is uniform across the inlet (Fig. 6.16D). The tide is just beginning to flood 12 hr later as the northerly wind reaches 9.1 m/s (Fig. 6.15E). Southward currents are generated by this wind in the shallow water on the margins of the bay mouth while the new flood tide flows to the north. These flows extend to the sea bed and fronts form on each side of the inlet (Fig. 6.16E). The forecast wind weakens during the next 12 hr and sets up a strong ebb tide with currents > 25 cm/s on the west shore of the bay mouth (Fig. 6.15F). Near-bottom outflow exceeds 10 cm/s across the entire mouth, even in shallow water (Fig. 6.16F). The northerly wind continues until the following flood tide and surface currents within SLB are variable (Fig. 6.15G). Tidal inflow dominates in the center of the inlet while outflow persists at the margins (Fig. 6.16G). The NOGAPS wind is more easterly at 1200 UT on Dec. 7 at high water and surface currents are 24 cm/s on the eastern side of the bay mouth (Fig. 6.15H). This flow is baroclinic with weak near-bottom currents (Fig. 6.16H).

The ENE wind continues until Dec. 8 and surface currents within SLB indicate that mixing should be thorough, with a CCW circulation in the central bay (Fig. 6.15I). The easterly wind appears to have more influence on currents in the bay than a northerly wind. This is seen in the section across the bay mouth, which shows outflow along the western margin and as a jet in mid-channel and flood tide flow elsewhere (Fig. 6.16I). Note the northward near-bottom currents >4 cm/s in the main channel. The wind becomes more southerly during the next 12 hr and the flow within the inlet strengthens to >20 cm/s at the surface (Fig. 6.15J) while the subsurface currents reflect an expansion of the reversed flow of the previous 12 hr (Fig. 6.16J). The multiple jets have merged to form an outflow that weakens to the west.

A second cold front passed over on Dec. 8 and the NOGAPS wind is northerly on Dec. 9. The resultant surface currents are again uniformly seaward (Fig. 6.15K) but the section at the bay mouth indicates highly baroclinic flow (Fig. 6.16K). Inflow exceeds 5 cm/s in near-bottom jets in the main channel while outflow is >12 cm/s in intervening jets that reach the bottom. The northward currents are residual from the preceding flow regime (Fig. 6.16J). The northerly wind strengthens during the following low water and surface currents are greater within the central bay than through the inlet (Fig. 6.15L). The flow through the channel is now complex, with strong outflow (>16 cm/s) along the margins and weak inflow in mid-channel while the beginning flood tide is only evident near the bottom (Fig. 6.16L).

The evolving mass transport through the bay mouth can be examined using sections of salinity (lower panels in Fig. 6.16). The simulated salinity gradient across the bay mouth is <2 psu at low water prior to the first cold front, and stratification is weak (Fig. 6.16A). The salinity decreases during the flood tide and the water column is well mixed by 1200 UT Dec. 4 (Fig. 6.16B). The southerly wind transports high-salinity water into the bay along the eastern shore and causes the salinity at the entrance to increase temporarily (Fig. 6.16C) but as the wind becomes WNW, the salinity decreases even with a flood tide (Fig. 6.16D). The water column becomes well mixed during the ebb tide because of the high wind speed (>9 m/s) (Fig. 6.16E). The flood tide of Dec. 6 increases salinity in the bay mouth until fresh water is transported as outflow on the west shore (Fig. 6.16F). The highest salinity water is located in the center of the inlet. The northwesterly wind of Dec. 7 reduces inflow and the inlet remains unstratified (Fig. 6.16G). The flood tide transports salty water into the eastern side of the inlet (Fig. 6.16H). The following ebb tide transports significant fresh water into the inlet (Fig. 6.16I) and stratification is strengthened by the flood tide until 1200 UT on Dec. 8 (Fig. 6.16J). The return to strong northerly winds reduces stratification and salinity in the inlet, however (Figs. 55K, L).

The preceding discussion reveals several interesting points about mixing and transport within the St. Louis Bay/Mississippi Sound area. Horizontal mixing occurs preferentially during winds with an easterly component rather than an N-S orientation. This may be due to the increased angle between the wind and the tides, which are primarily N-S in the central bay. The water on the western shore of the bay mouth tends to be fresher while the eastern shore is saltier. This implies a residual CW rotation due to the interaction of the tides with the wind. The salinity distribution in the bay entrance varies from well mixed vertically to stratified, and a salinity front often develops aligned with the flow. The bay develops occasional weak estuarine circulation during flood tides (e.g., Fig. 6.16J). The water column is easily mixed by either tidal flow or wind-generated turbulence.

6.3.5 Circulation and mass transport during Hurricane Katrina (August 2005)

Tropical cyclones are obviously important for resuspending bottom sediments and flushing estuaries in the Gulf of Mexico. Therefore, it is necessary to evaluate their contribution to transporting contaminants out of St. Louis Bay. Unlike cold fronts and tides, the strong winds and large waves that are generated will unquestionably entrain fine sediment within SLB; however, such an analysis is beyond the scope of the present study. The following discussion assumes that material will have been released from sediments by wave and current action. This simulation includes tidal flow and rivers. There will be no effort to evaluate the contribution of tides, however, because they are insignificant relative to the storm currents. The river inflow does not include higher discharge rates during the storm because they were unavailable. This is not significant because of the delay in runoff and the volume of high-salinity water that entered the bay.

This discussion will focus on two dynamic periods in the MSE during a tropical cyclone: (1) pre-landfall; and (2) post-landfall. The NOGAPS wind is from ENE at 0600 UT Aug. 28 and surface flow is uniformly into the bay (Fig. 6.17A). The wind continues to strengthen during the next 12 hr but the simulated surface currents change significantly. The flow within SLB has become convergent along the western margin north of the bay mouth (Fig. 6.17B). This convergent flow drives an outflow with a maximum velocity > 15 cm/s along the western margin of the inlet (Fig. 6.18A). All of the low-salinity river water is compressed into this jet (lower panel in Fig. 6.18A) while the overall salinity of this outflow is > 12 psu. The main storm surge builds in the sound at 0600 UT on Aug. 29 and currents are again into the bay but with larger magnitudes (Fig. 6.17C). The flow through the bay mouth is dominated by northward currents > 20 cm/s (upper panel in Fig. 6.18B) and the salinity has increased to > 22 psu (lower panel in Fig. 6.18B). There is a weak outflow along the western margin, however, with lower salinity water. The hurricane eye made landfall at 1110 UT (Knabb, Rhome et al. 2006) and the post-landfall phase of the storm flow began.

The forecast wind at 1800 UT Aug. 29 is westerly and a little weaker than before landfall (Fig. 6.17D). The flow within the sound reverses direction and the bay begins to drain rapidly, with surface currents >10 cm/s in central St. Louis Bay. The outflow is not uniform, however; bottom currents are into the bay (Fig. 6.18C, upper) because of the rapid shift in wind direction and the persistent stratification (Fig. 6.18C, lower). A tongue of 24 psu water intrudes into the bay along the center of the inlet. The bay is still draining 12 hr later despite the southeasterly wind >6 m/s (Fig. 6.17E). In fact, the flow has strengthened to >20 cm/s throughout the bay and outflow dominates through the bay mouth; there is weak inflow near the bottom along the western side of the main channel (Fig. 6.18D, upper). High-salinity water continues to flow from the bay after mixing with river inflow (Fig. 6.18D, lower). This outflow driven by the storm surge continues another 12 hr with little weakening (Fig. 6.17F) and eastward flow within the sound is undiminished.

The flow fields computed by NCOM on the SLB grid were used by HQCM to calculate the transport of both a passive tracer and particles. The tracer was introduced at the Jourdan and Wolf Rivers for Aug. 2005 but very little transport occurred before H. Katrina. The distribution at the end of Aug. (Fig. 6.19A) resembles that from the cold front in Mar. (Fig. 6.12). The concentration is more uniform within the bay and the highest values are predicted along the western shore. The westerly winds after landfall did not generate eastward flow within the bay; instead, the outflow driven by the falling storm surge (Fig. 6.17D) distributes the tracer to the southwest. The most significant difference between the particle distribution after the cold front and the hurricane is the lack of any particles to the west of the bay (Fig. 6.19B). As suggested by the tracer distribution, the particles are mixed within the bay and along the western shore. However, the strong post-landfall eastward flow within the sound has transports all particles to the east. None have been transported south of Square Handkerchief Shoal even because the currents are >50 cm/s.

The hurricane flow system is much larger than St. Louis Bay. Therefore, it should be examined at the scale of the entire Mississippi Bight in order to determine the causes and effects of the storm surge in the bay. The hydrodynamic computations were completed on the MSB grid to supply boundary conditions to the SLB grid. These results show the regional impact of the storm. Four days prior to landfall, the NOGAPS wind over the MSB is easterly at 2 m/s (Fig. 6.20A) and a typical summer flow regime is present. Surface currents within the sound are westward at <35 cm/s and weak in the vicinity of SLB. The surface salinity in the summer varies from 10 psu to 30 psu within Mississippi Sound, which is typical for the area (Smith, Macauley et al. 2009). The lowest salinities are predicted near the largest rivers and in the far west where exchange with the open sea is limited. The steady westward flow during the storm's approach has pushed high-salinity gulf water into the sound and the salinities are higher throughout the MSE (Fig. 6.20B). The model predicts a thin band of water with salinity <30 psu along the coast and mesohaline water is restricted to the bays. The forecast wind 24 hr after landfall is southwesterly at 4.2 m/s and the surface currents throughout the MSE are eastward (Fig. 6.20C). The combination of the wind stress and falling storm surge creates maximum currents of 80 cm/s. Despite this seaward flow, the salinity remains high throughout the estuary except in the west, where mesohaline water is expanding from Lake Borgne. Note that the southerly wind is keeping the salinity high in the lower part of Mobile Bay. These high post-Katrina salinities were noted in previous work (Smith, Macauley et al. 2009).

6.4 Discussion and summary

This study has used numerical models with very little calibration to simulate the hydrodynamics and mass transport within the Mississippi Sound estuary. It was not obvious *a priori* that this approach would yield useful insight into mixing processes in the region. This uncertainty has been alleviated by the robustness of the results. The selected model grids adequately resolve the different scales for the region. The MSB grid (cell size ≈ 900 m) resolves the inlets well and nests reasonably with the global model at the open boundaries. The SLB model (cell size ≈ 80 m) is able to reproduce details of circulation in the bay and still nest to the MSB grid with only minor numerical noise. The vertical structure of flow and mass transport at the inlet to SLB demonstrates the necessity of using a 3D model for these event flows (see Figs. 50, 52, 55, 57). It is noteworthy that this advantage is dependent on the relationships between the components of the flow and is, therefore, difficult to predict ahead.

There are two problems with these simulations: first, the tide amplitude is too low and, second, the wind direction and magnitude are incorrect sometimes. The cause of the tidal prediction error is the bottom drag. The parameterization of bottom friction is not as accurate for tidal currents as it is for other flows. Errors in the wind forecast are beyond the scope of this work but substantial advances have been made in nested atmospheric modeling (http://www.nrlmry.navy.mil/coamps-web/web/home). Both of these sources of error can be addressed in future work, but they do not significantly decrease the results discussed above. As

shown by the results, the timing of flow components is paramount in this application. The events studied were thus selected because the models had fewer phase errors.

The simulations presented above examined three hydrodynamic events in this region with respect to circulation in St. Louis Bay and transport into Mississippi Sound: (1) tidal; (2) cold fronts; and (3) tropical cyclones. The cumulative tidal surface currents for Jan. 2005 (Fig. 6.8) indicate a weak residual outflow along the eastern side of the bay entrance and a recirculation pattern around a shoal just south of the inlet. Similar currents for the sound (Fig. 6.9) suggest that this outflow does not leave the western sound at the bay mouth. If this result is superimposed on the potential outflow associated with waves and currents (Cobb and Blain 2002), it is likely that dissolved substances in the bay water are periodically transported into the sound by tidal movement.

Wind-forced transport during a weak cold front in Mar. 2005 indicates outflow of dissolved material (Fig. 6.12). The tracer is released at a continuous rate at the rivers but it is transported as a patch along the western margin of SLB because the peak northerly wind reinforces the southward drift. This pattern is reflected in the transport of particles from the bay as well (Fig. 6.14). Note, however, that the particles are widely disseminated within the sound. The hydrodynamic results for back-to-back cold fronts in Dec. 2005 support the wind-generated results from the Mar. simulation. The stronger winds during these events generate complex circulation within the bay (e.g., Figs. 54A, G, and I) and continuous outflow at the inlet (Fig. 6.16). The SLB circulation and outflow during H. Katrina are similar to the Dec. cold fronts but much stronger (Fig. 6.17). Ironically, the strength of the flow within the sound limits the dispersion of the tracer and particles (Fig. 6.19).

The model simulations demonstrate the potential for dissolved material to be transported out of St. Louis Bay into Mississippi Sound. The final question, therefore, is whether this is a reasonable result. The model simulations of tracer and particle transport can be validated using the Dioxin data collected in 2001 (Elston, Cake et al. 2005). The highest TEQ values (15-16) were measured outside the bay just north of Square Handkerchief Shoal (Fig. 6.2). This finding is consistent with transport by residual tidal currents, wind-forced outflow during cold fronts, and combined wind- and setup-forced flow during Hurricane Katrina. The specific location of the outfall was not used in this study but the moderate TEQ values (8-10) to the north and west are in agreement with the circulation in SLB during these simulations. The low values (3-7) in the eastern bay are supported by the model results, which indicate little eastward mixing except during the combined flow of the Dec. cold fronts. The consistency of the observations and the simulated event and tidal circulation indicate that the models are capturing the dominant mixing processes in St. Louis Bay.

Table 6.1. Tidal constituents used at the open boundary for the MSB model domain. The actual values varied across the southern boundary (see Fig. 6.1). These are the values at the SE corner (286, 1).

Constituent	Elevation		Normal Velocity		Tangential Velocity	
	Amplitude (m)	Phase (Degrees)	Amplitude (m/s)	Phase (Degrees)	Amplitude (m/s)	Phase (Degrees)
K1	0.144	18	1.393	60	1.883	288
O1	0.142	11	1.456	63	1.385	278
P1	0.048	16	0.489	355	0.531	251
Q1	0.033	354	0.196	301	0.224	234
K2	0.005	60	0.094	184	0.168	303
M2	0.027	103	0.080	295	1.437	71
N2	0.009	118	0.058	108	0.632	48
S2	0.015	90	0.038	18	0.316	353

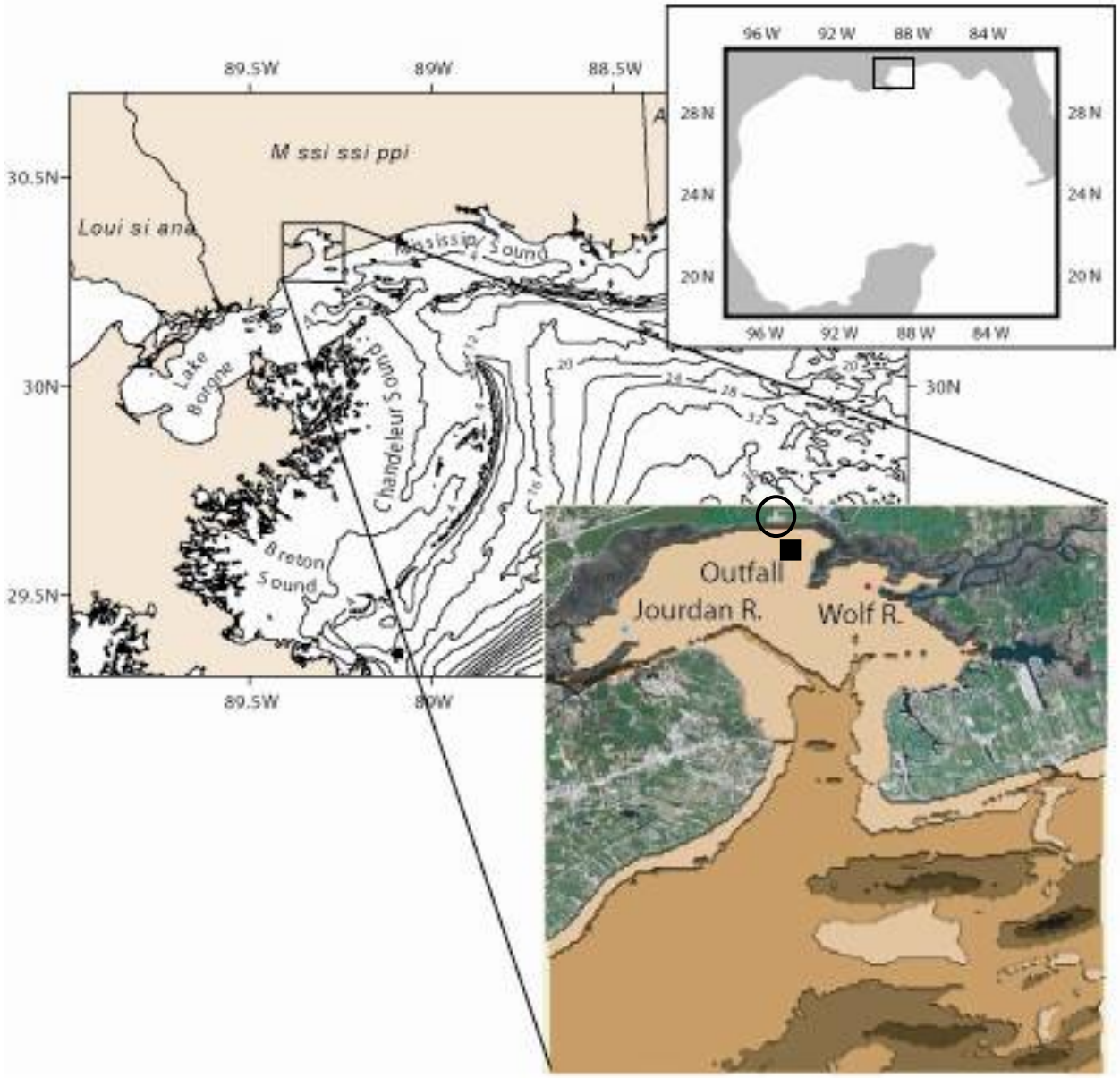

Figure 6.1. Map of Mississippi Sound and St. Louis Bay in the northcentral Gulf of Mexico. The bathymetry in the inset map is shaded using contours intervals of 1 m. The light tan is <2 m and the dark brown is 4-5 m. A Landsat image is overlaid for general reference. Note the Outfall location (square) and the titanium dioxide refinery (circled) discussed in the text.

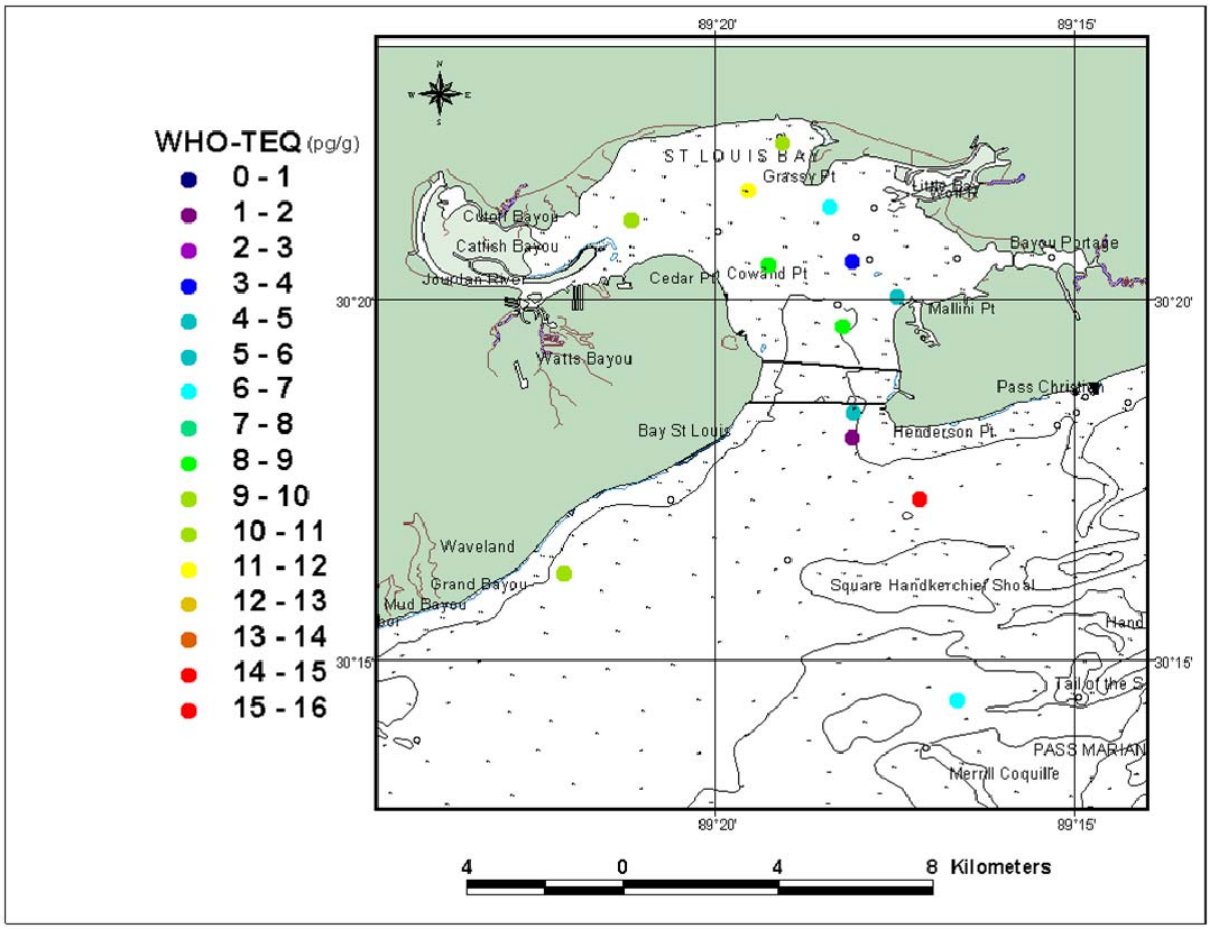

Figure 6.2. Dioxin Total Equivalency Values (TEQ) for sediments from St. Louis Bay and the adjacent Mississippi Sound (Elston, Cake et al. 2005) plotted on a map of St. Louis Bay. The colored circles indicate the concentration of dioxins in World Health Organization Toxicity Equivalent units (1 picogram = 10^{-12} g). This figure was produced by R. Parsons of the National Coastal Data Development Center, NOAA, Stennis Space Center, MS.

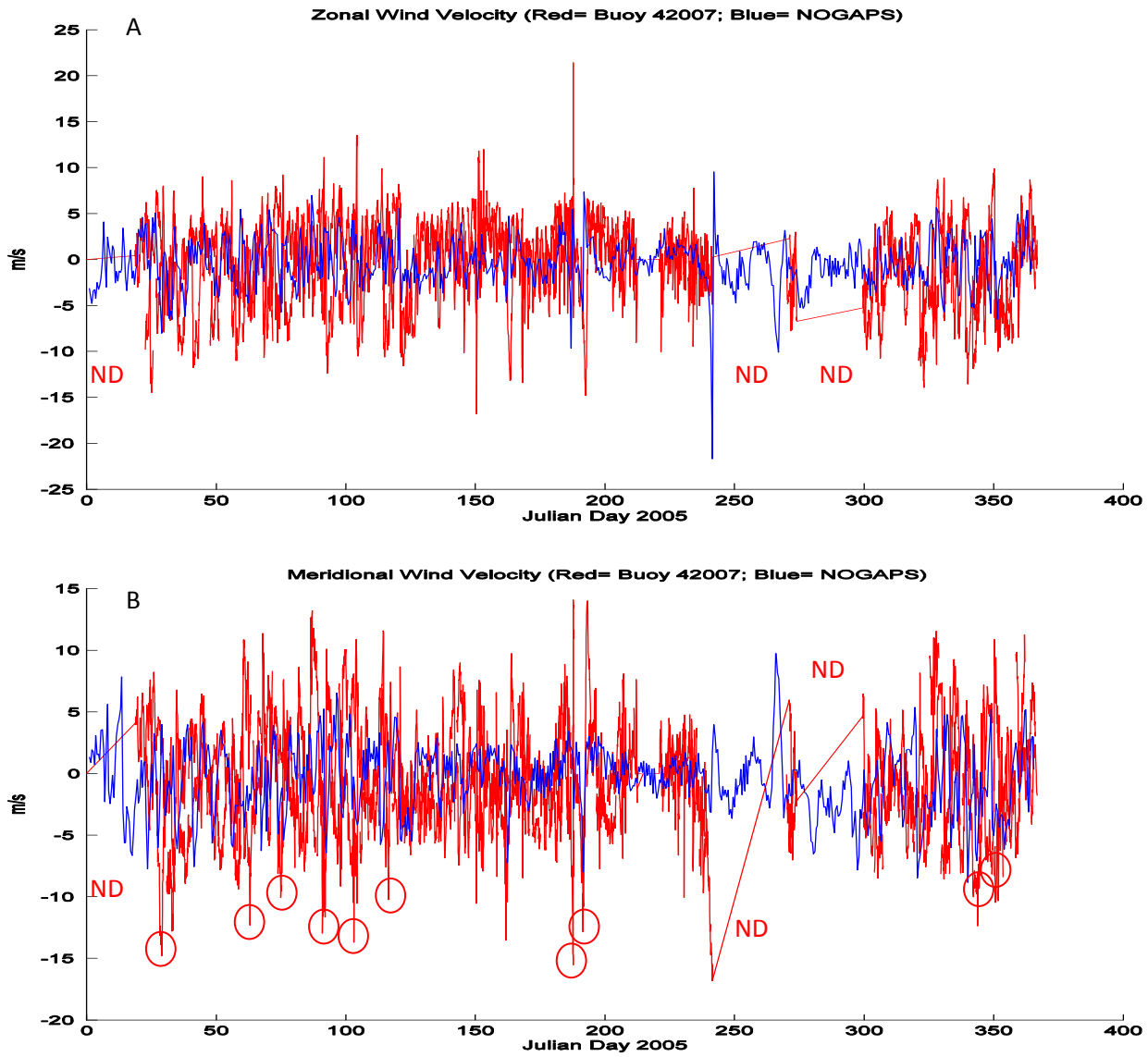

Figure 6.3. Time series of wind in the northern Gulf of Mexico in 2005. (A) E-W (zonal) component. (B) N-S (meridional) component. The red lines in the plots are the 5-m winds from buoy 42007 (30.090 N, 88.769 W) and the blue lines are the 10-m output from NOGAPS at cell (85, 130) on the SLB grid. ND = no data available from buoy 42007. The red circles in B indicate the post-frontal northerly component of the buoy winds for strong cold fronts (N-S wind > 10 m/s). See text for further explanation. Note that the resultant wind vector is the direction toward which the wind is blowing.

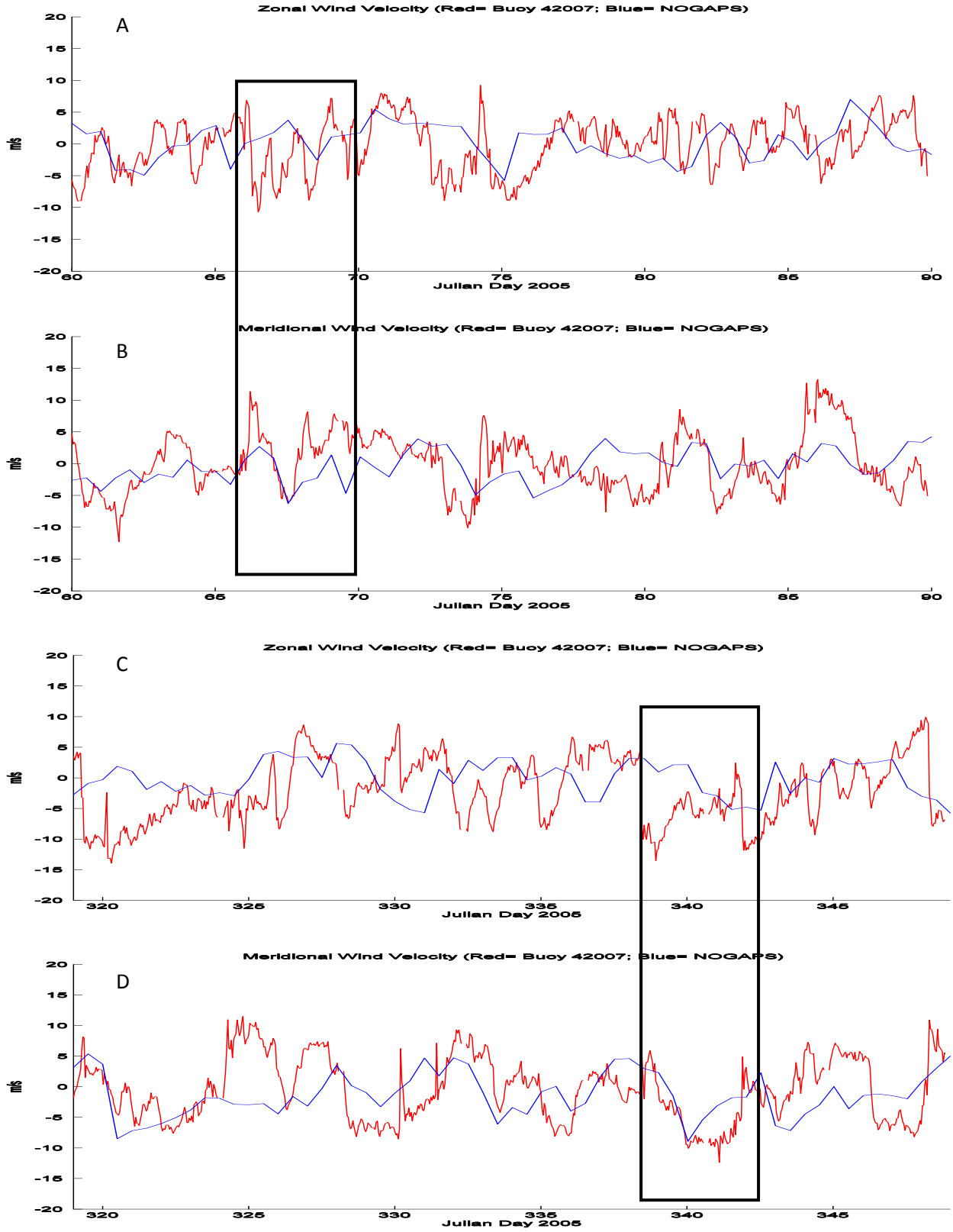
Zonal Wind Velocity (Red= Buoy 42007; Blue= NOGAPS)
A
m/s
Julian Day 2005
Meridional Wind Velocity (Red= Buoy 42007; Blue= NOGAPS)
B
m/s
Julian Day 2005
Zonal Wind Velocity (Red= Buoy 42007; Blue= NOGAPS)
C
m/s
Julian Day 2005
Meridional Wind Velocity (Red= Buoy 42007; Blue= NOGAPS)
D
m/s
Julian Day 2005

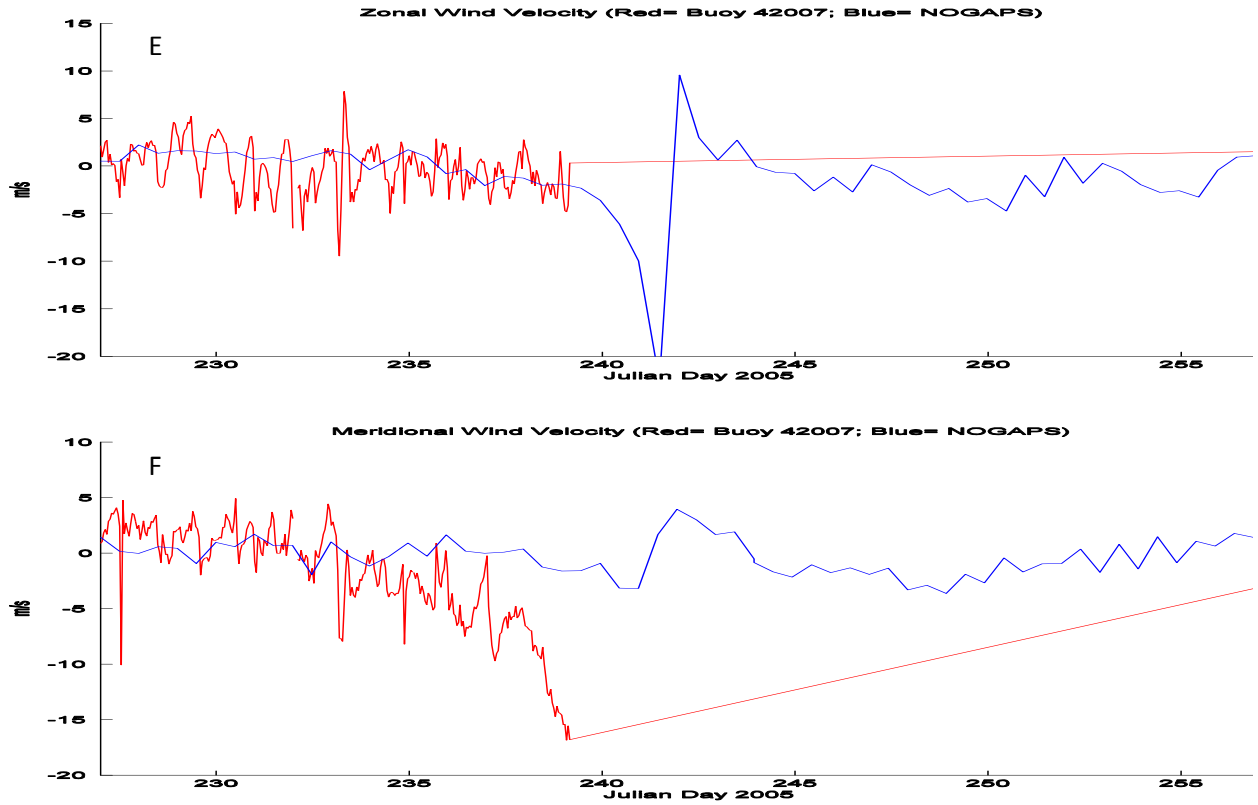

Figure 6.4. Time series of winds in the northern Gulf of Mexico in 2005. (A) Zonal winds for Mar.; (B) Meridional winds for Mar.; (C) Zonal winds for Nov The rectangle indicates the period discussed in the text and shown in Figs. 6.7, 6.10, and 6.11; (D) Meridional winds for Nov.; (E) Zonal winds for Aug. - Sep.; and (F) Meridional winds for Aug. - Sep. The red lines in the plots are the data from buoy 42007 and the blue lines are the output from NOGAPS at cell (85, 130) on the SLB grid. The vertical axis is m/s. Note that the resultant wind vector is the direction toward which the wind is blowing.

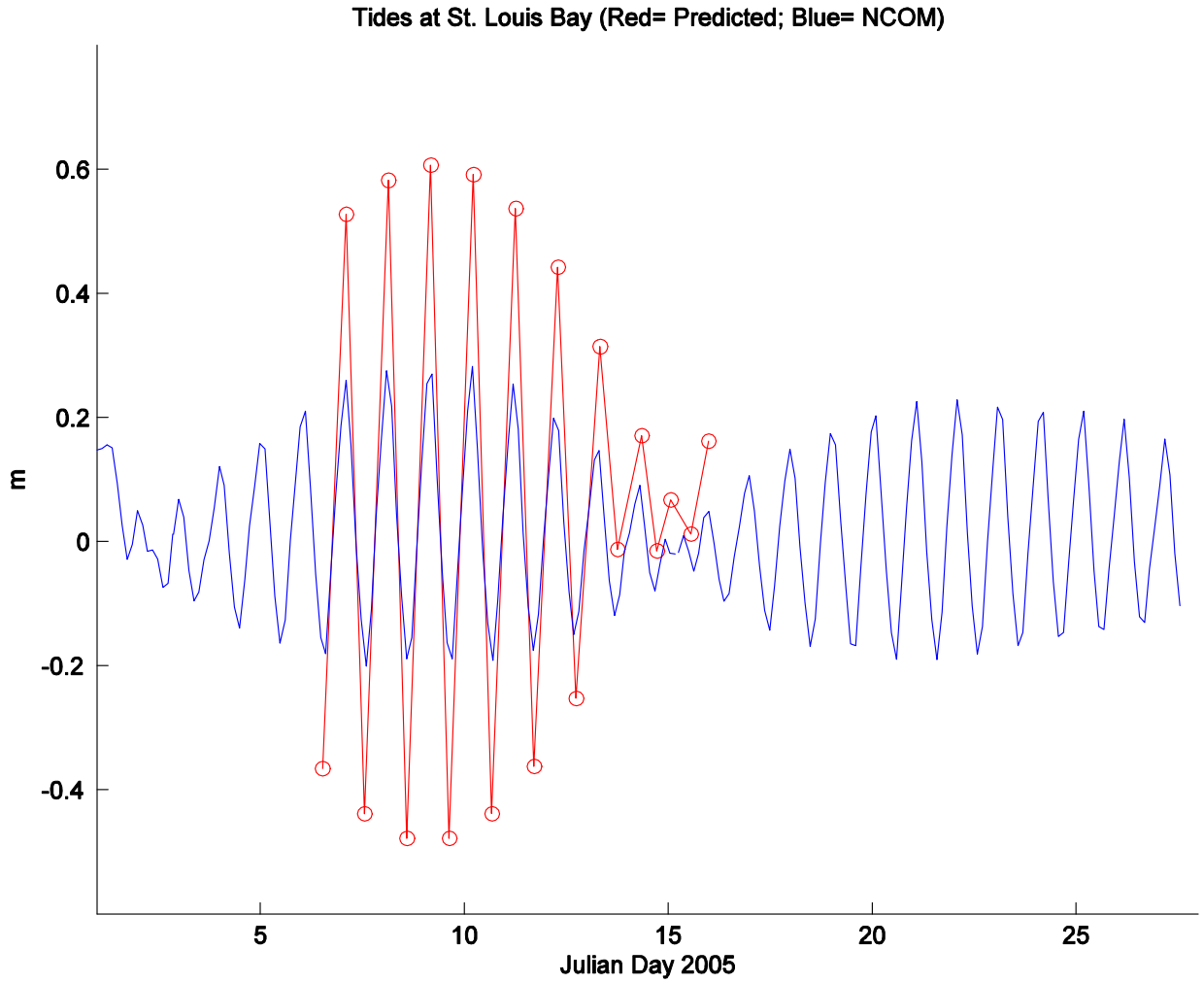

Figure 6.5. High- and low-water predictions at the Bay Waveland Yacht Club (30.3250° N, 89.3250° W) for Jan. 2005 (red circles). A tide gauge was not installed until November, 2005. The tides are referenced to mean lower low water (MLLW), which is the long-term mean of the daily low water in this area. The NCOM predictions on the SLB grid (blue line) have been adjusted +20 cm to account for the different reference levels.

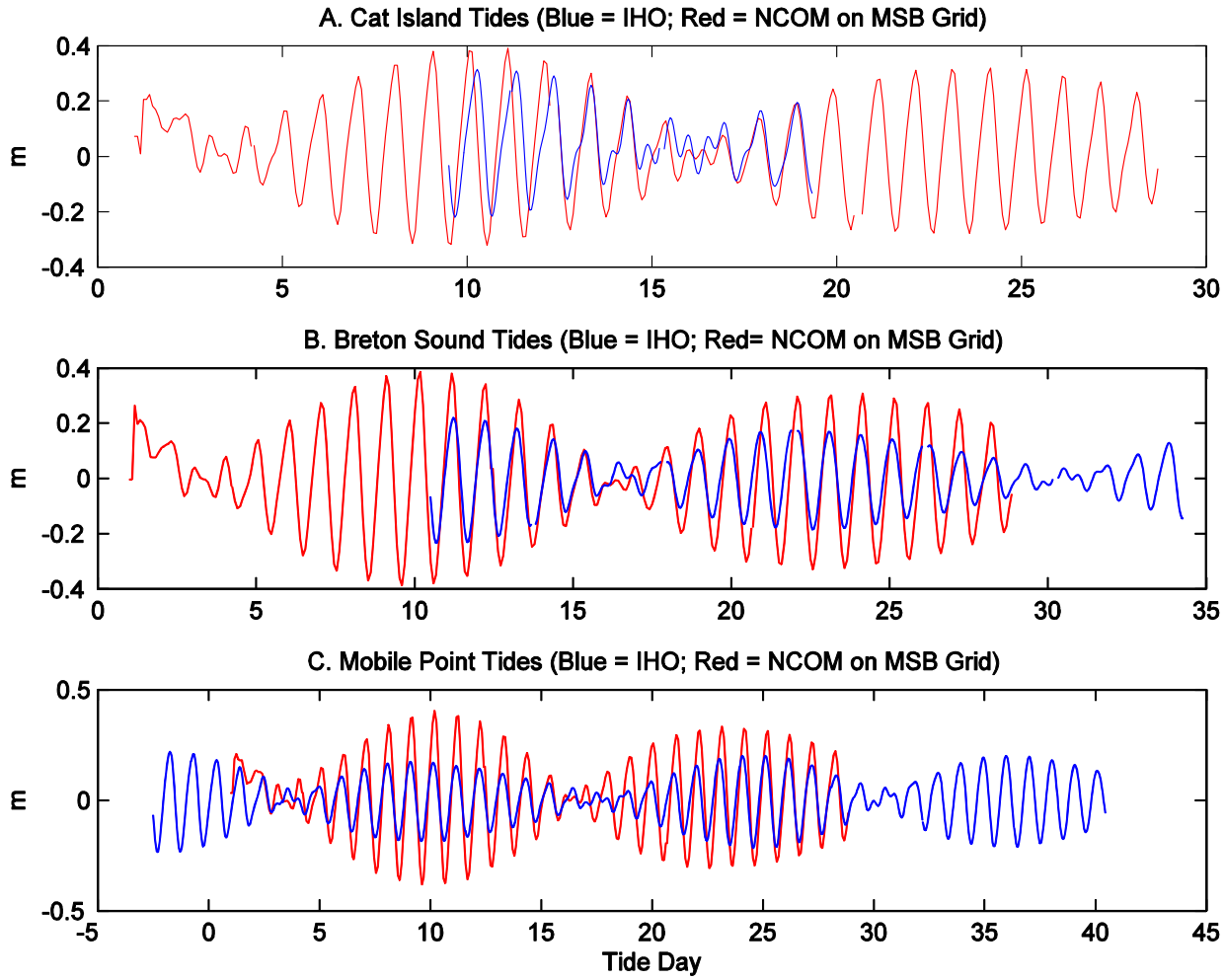

Figure 6.6. Tides within the Mississippi bight. The red lines are from the International Hydrographic Office (IHO) database and the blue lines are from the MSB grid (900 m) NCOM nest. The IHO data are from March 1997 (Keen 2002). They have been adjusted in time to show the relative performance of the NCOM model for the amplitude and phase within a tidal cycle and not for a specific time interval. Neither dataset includes subtidal signals. NCOM used the tidal constituents from Table 6.1 and no river inflow. The horizontal axis refers to the diurnal tide cycle in the area, which is approx. one day.

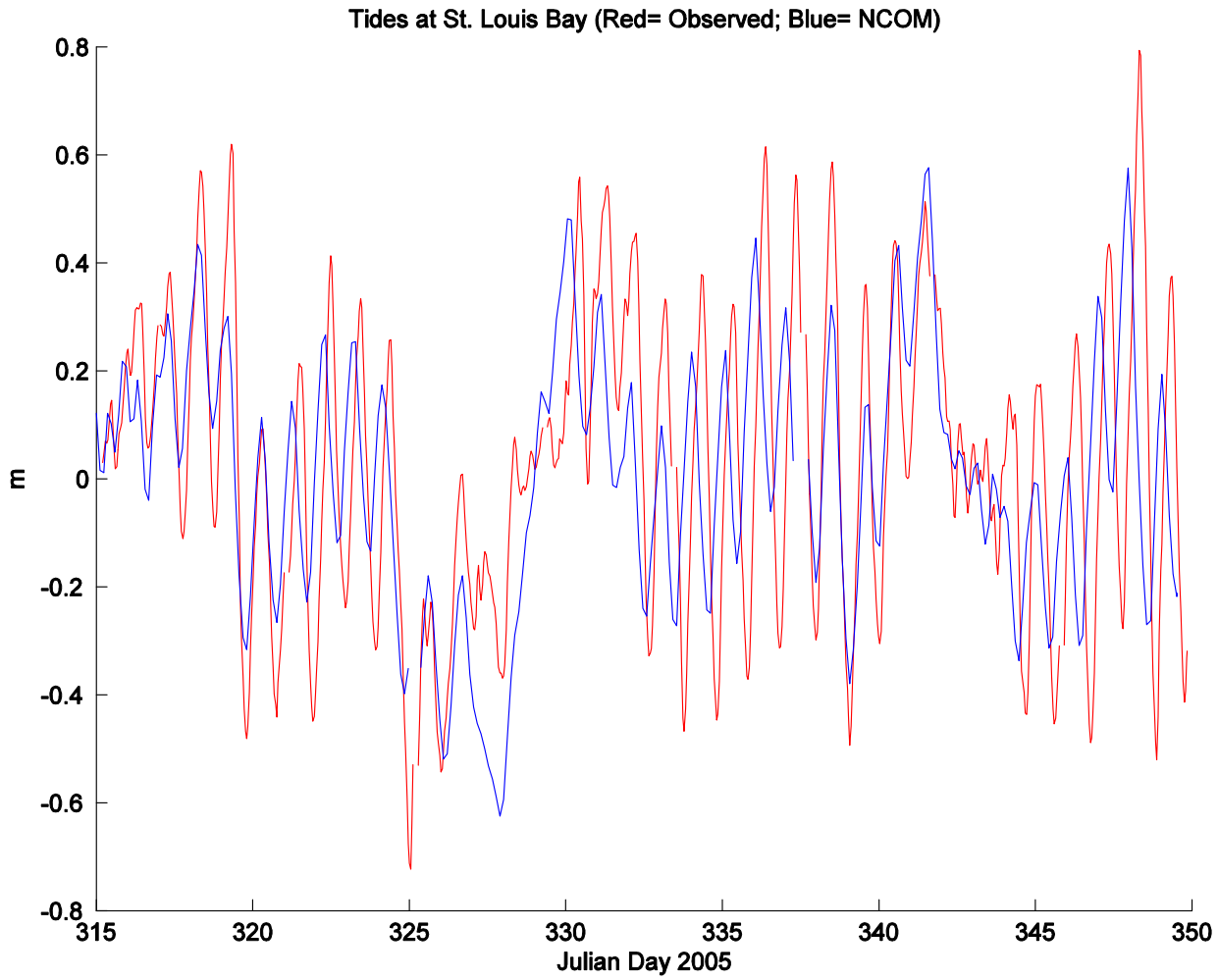

Figure 6.7. Time series of water levels from St. Louis Bay for Nov. - Dec., 2005. The NCOM predictions were adjusted by +20 cm as an estimate of the different reference levels; the model uses zero whereas the tide station uses MLLW (Mean Lower Low Water), which is the mean of the low water each tidal day for the diurnal tides in this location (http://tidesandcurrents.noaa.gov/datum_options.html).

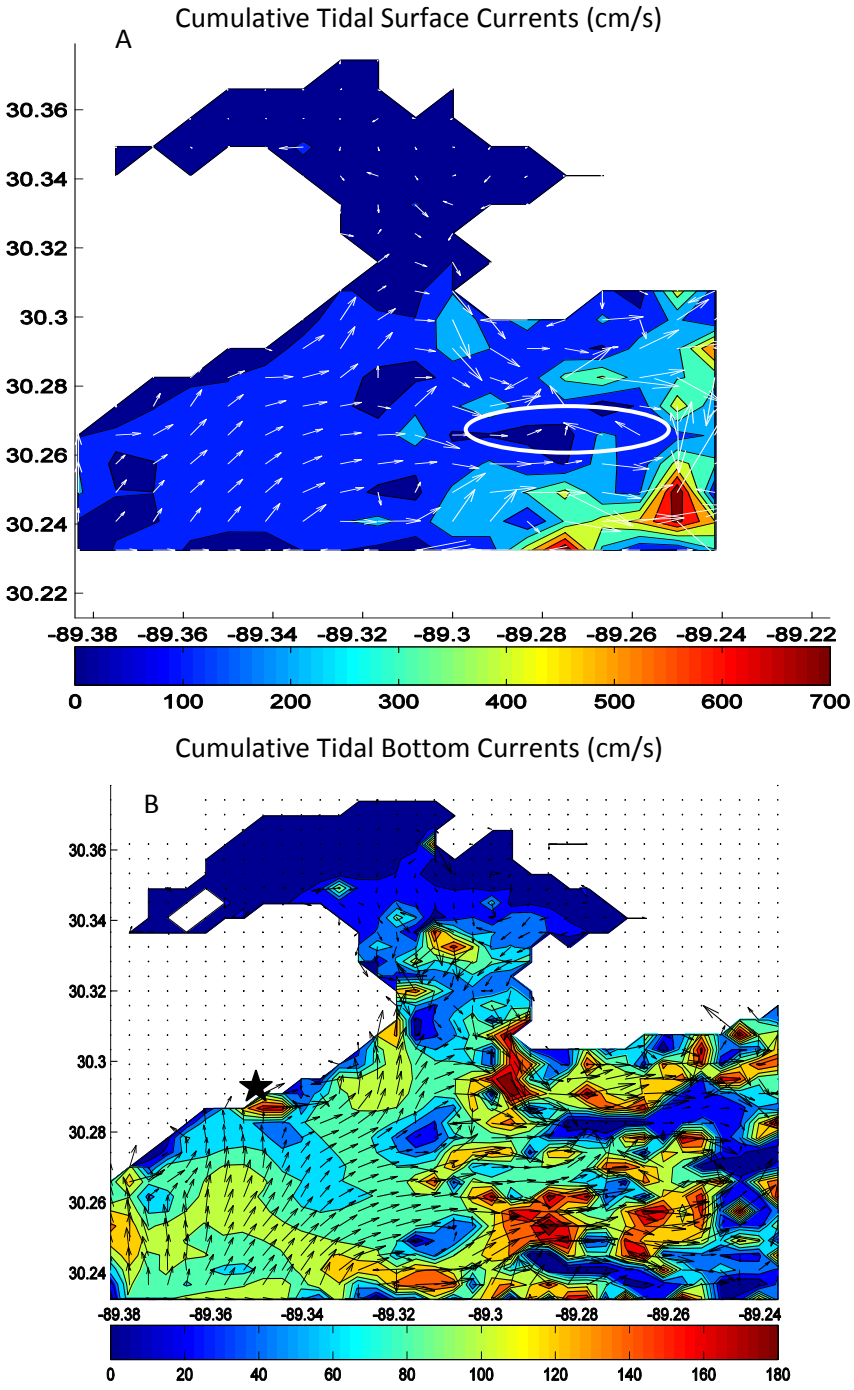

Figure 6.8. Cumulative tidal currents (cm/s) from NCOM for Jan. 2005 on the SLB grid. The model used 8 constituents (see Table 6.1), which were passed as a boundary condition from the MSB grid. (A) Surface currents. The plot shows every tenth grid point. (B) Bottom currents. The plot shows every fifth grid point. The ellipse in A indicates the approx. outline of Square Handkerchief Shoal. Waveland is indicated by a star in B.

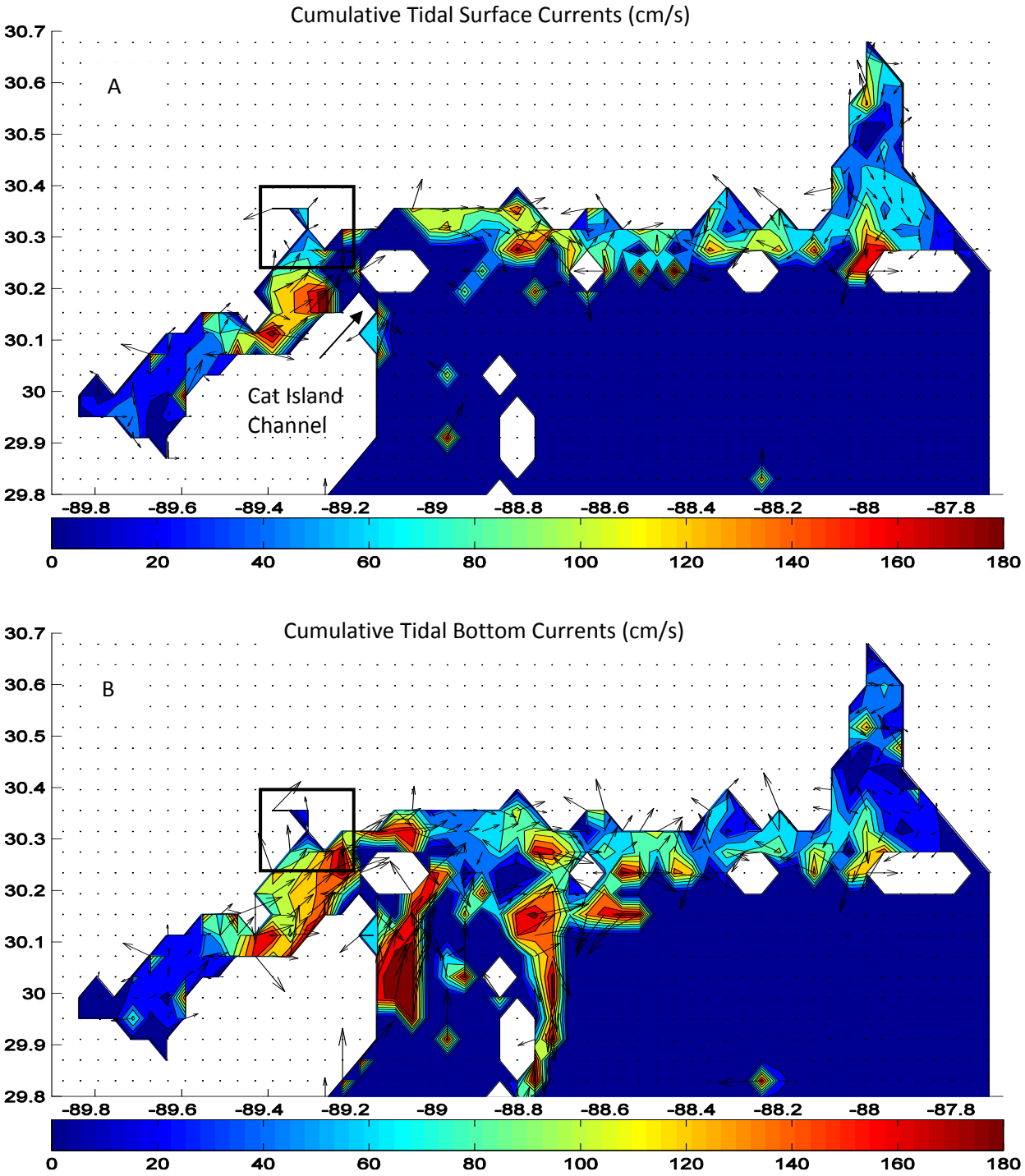

Figure 6.9. Cumulative tidal currents from NCOM for Jan. 2005 on the MSB grid. (A) 50 cm below the surface. (B) The lowest model output layer. The model used 8 constituents (see Table 6.1). The plot shows every fifth grid point. The magnitude was capped in order to show details inside Mississippi Sound. The max values are $>10^4$ cm/s (surface), and 160 cm/s (bottom). A residual > 200 cm/s is normalized by the largest residual in the grid for both figures. The SLB grid is outlined.

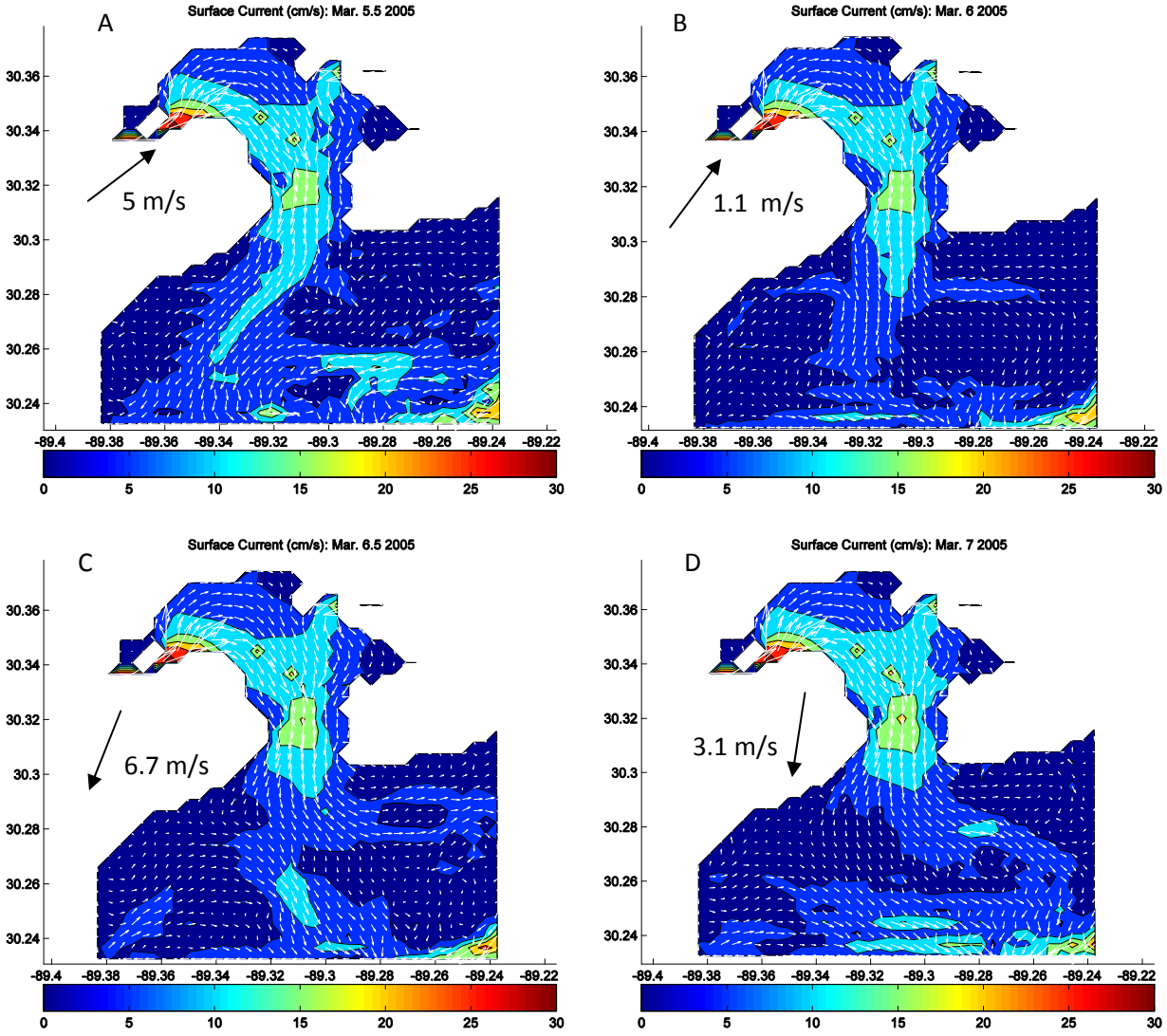

Figure 6.10. Snapshots of surface current vectors over contours of speed (cm/s) during a cold front in Mar. 2005. (A) 1200 UT Mar. 5; (B) 0000 UT Mar. 6; (C) 1200 UT Mar. 6; (D) 0000 UT Mar. 7. This simulation used no tides but did include inflow from rivers. The labeled vectors indicate the wind direction and magnitude from NOGAPS.

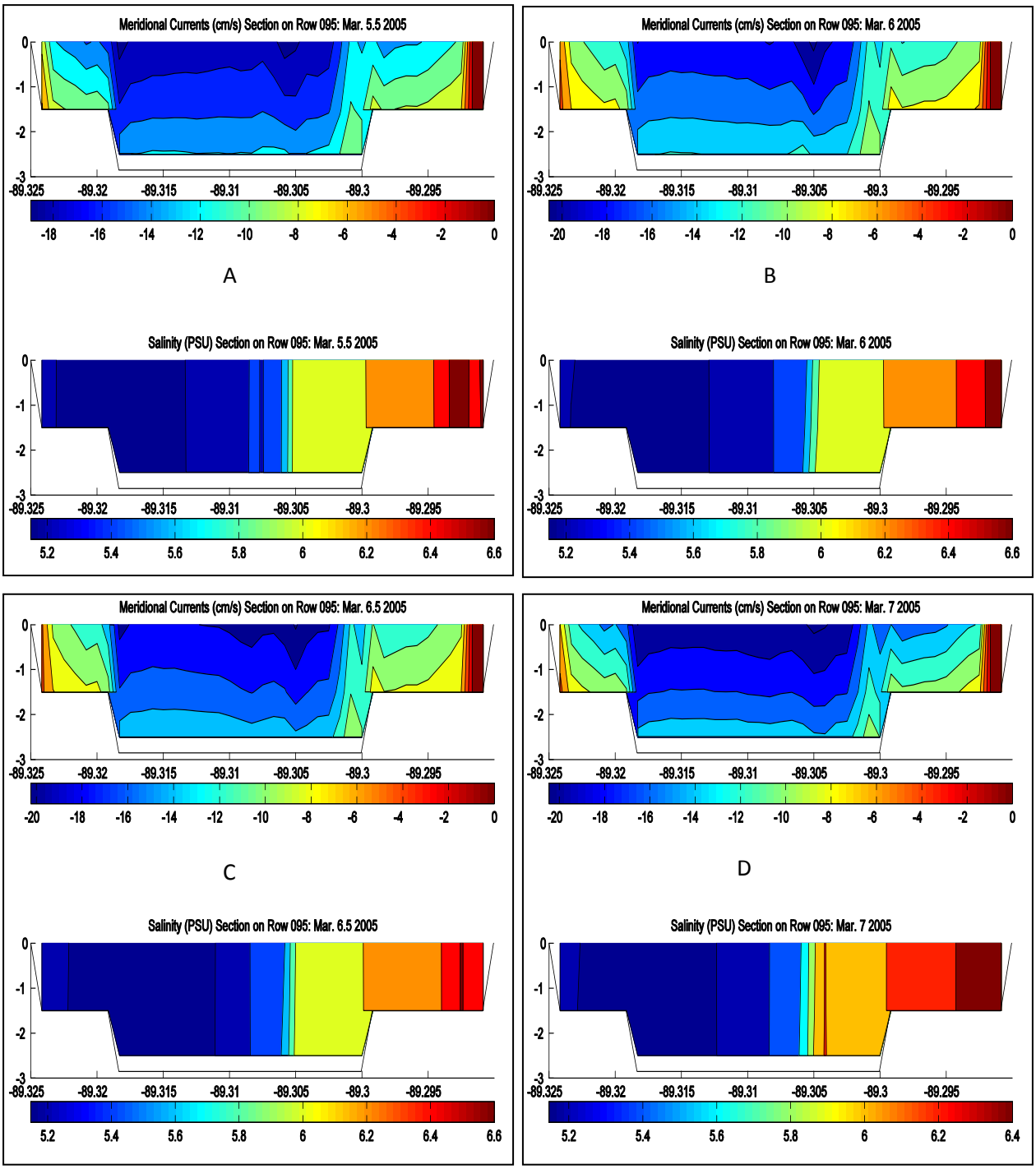

Figure 6.11. Sections of meridional currents (upper panels) and salinity (lower panels) computed by NCOM during the cold front of Mar. 4-7. (A) 12 UT Mar. 5; (B) 00 UT Mar. 6; (C) 12 UT Mar. 6; (D) 00 UT Mar. 7. This simulation did not include tides. The E-W section is across the narrow entrance to St. Louis Bay at row 95 (30.3108N).

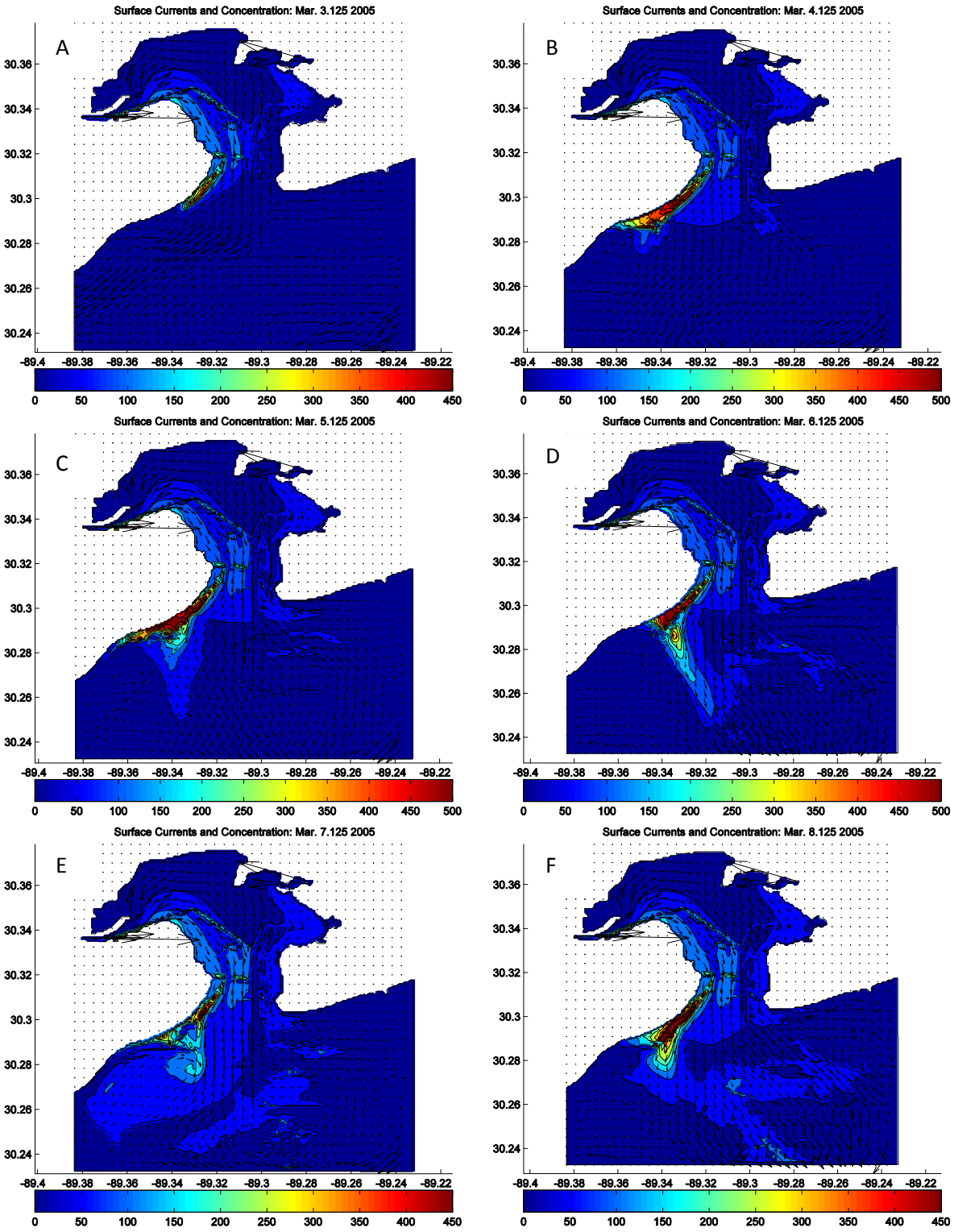

Figure 6.12. Snapshots of surface currents over contours of the tracer concentration computed by HQCM on the SLB grid at 24 hr intervals in Mar. 2005: (A) 0300 UT Mar. 3; (B) Mar 4; (C) Mar. 5; (D) Mar. 6; (E) Mar. 7; and (F) Mar. 8. The currents are from NCOM (see Fig. 6.10 for details). The max current ≈ 35 cm/s.

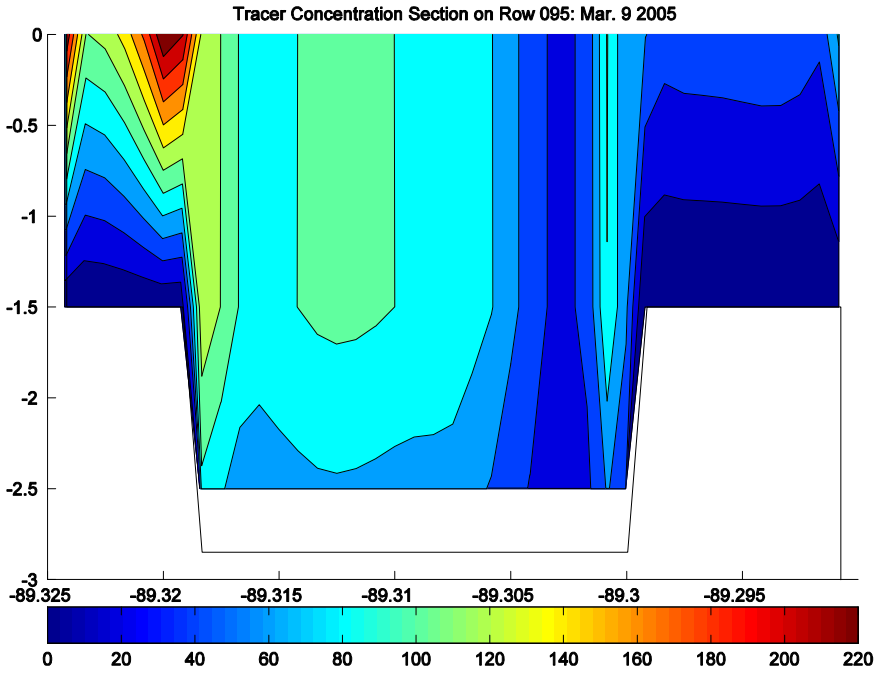

Figure 6.13. Section of Tracer concentration computed by HQCM after the cold front of Mar. 4-7. Forcing currents are from NCOM on the SLB grid. This simulation did not include tides. The E-W section is across the entrance to St. Louis Bay at row 95 (30.3108N).

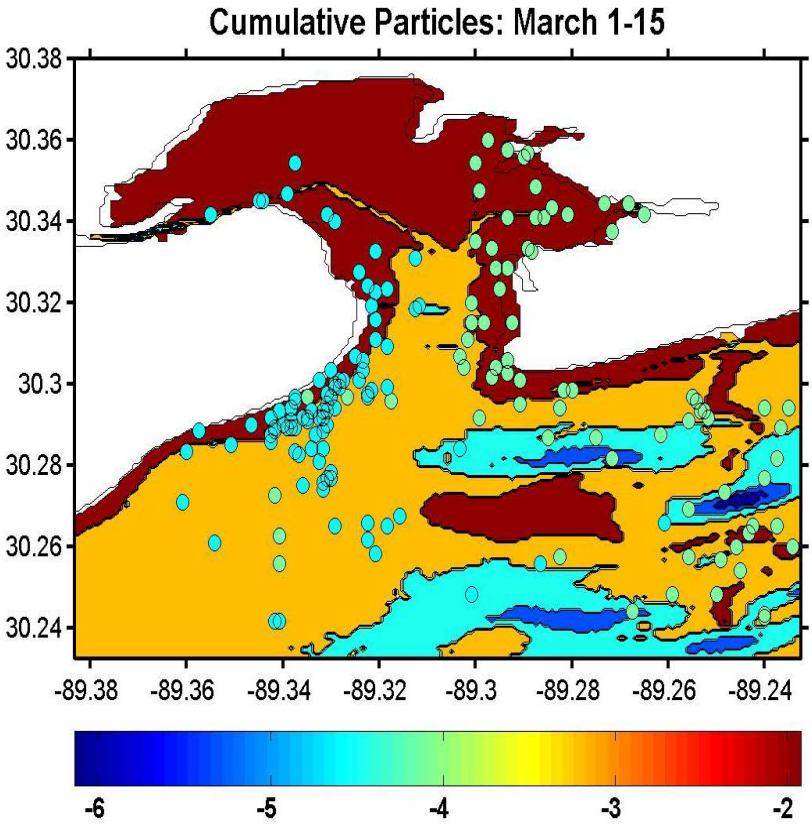

Figure 6.14. Location of particles released at the Wolf (green circles) and Jourdan (blue circles) Rivers in Mar. 2005. Particles were released every 3 hr. The currents are from NCOM on the SLB grid.

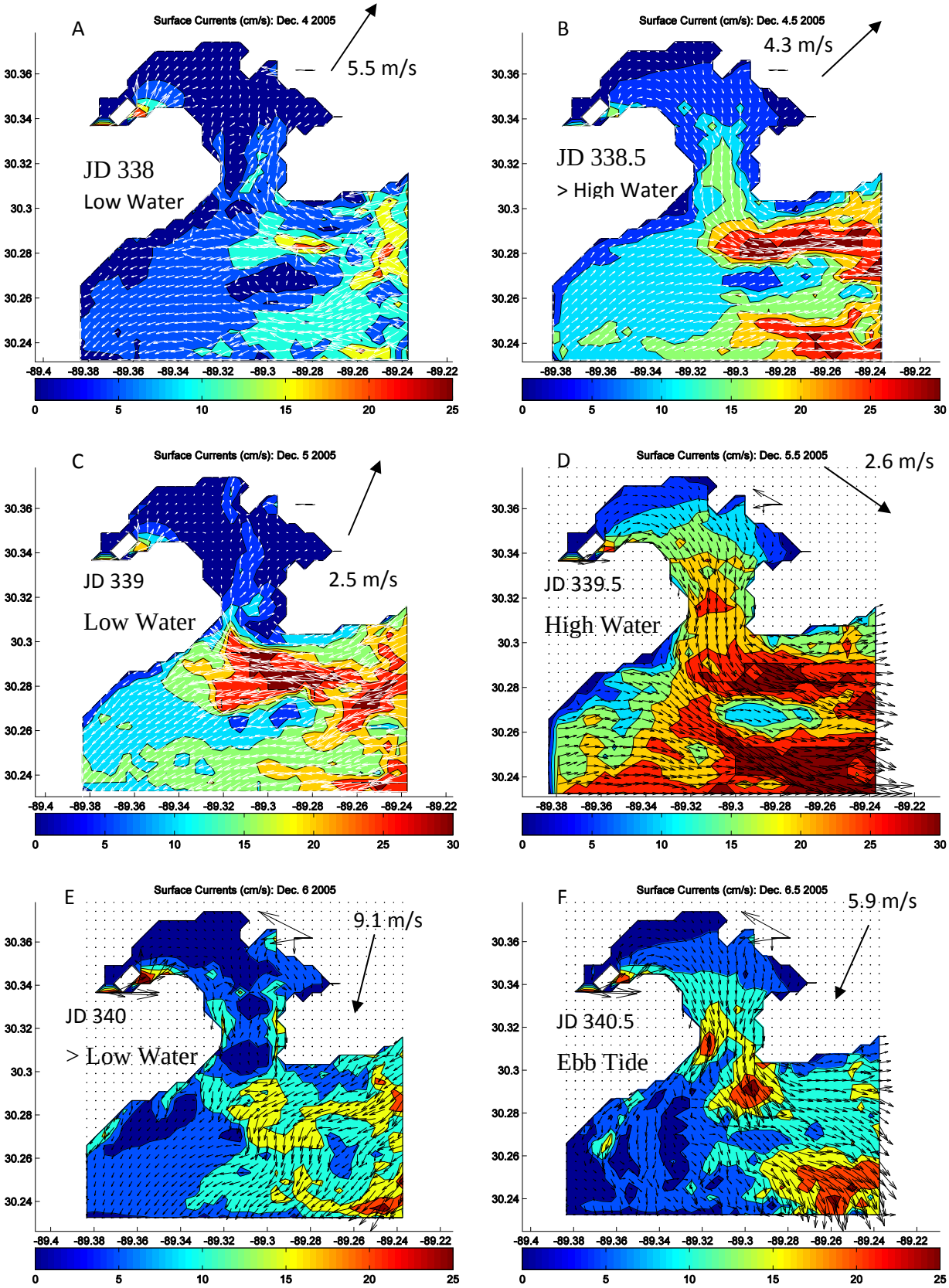
A
Surface Currents (cm/s): Dec. 4 2005
5.5 m/s
JD 338
Low Water
B
Surface Current (cm/s): Dec. 4.5 2005
4.3 m/s
JD 338.5
> High Water
C
Surface Currents (cm/s): Dec. 5 2005
JD 339
Low Water
2.5 m/s
D
Surface Currents (cm/s): Dec. 5.5 2005
2.6 m/s
JD 339.5
High Water
E
Surface Currents (cm/s): Dec. 6 2005
9.1 m/s
JD 340
> Low Water
F
Surface Currents (cm/s): Dec. 6.5 2005
5.9 m/s
JD 340.5
Ebb Tide

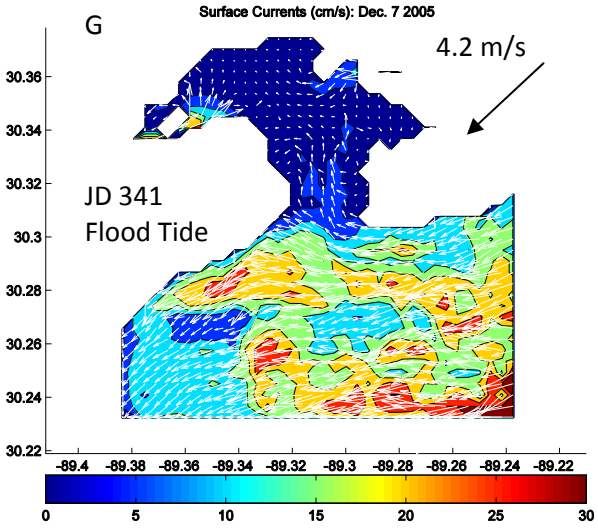
Surface Currents (cm/s): Dec. 7 2005
G
4.2 m/s
JD 341
Flood Tide

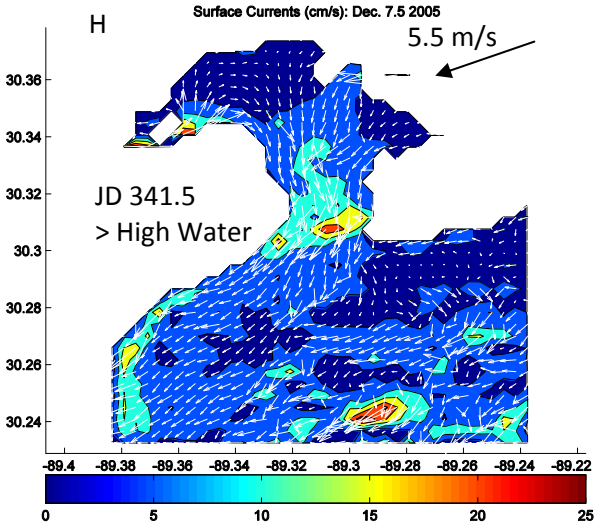
Surface Currents (cm/s): Dec. 7.5 2005
H
5.5 m/s
JD 341.5
> High Water

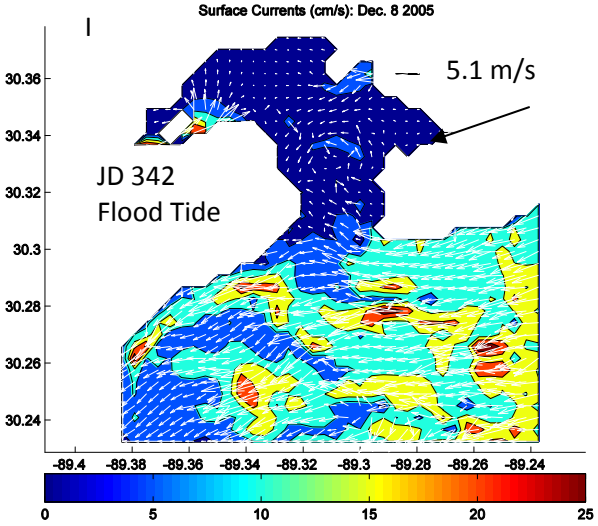
Surface Currents (cm/s): Dec. 8 2005
I
5.1 m/s
JD 342
Flood Tide

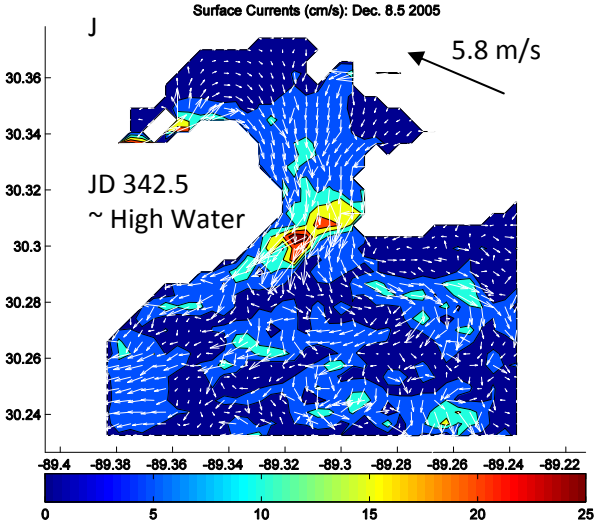
Surface Currents (cm/s): Dec. 8.5 2005
J
5.8 m/s
JD 342.5
~ High Water

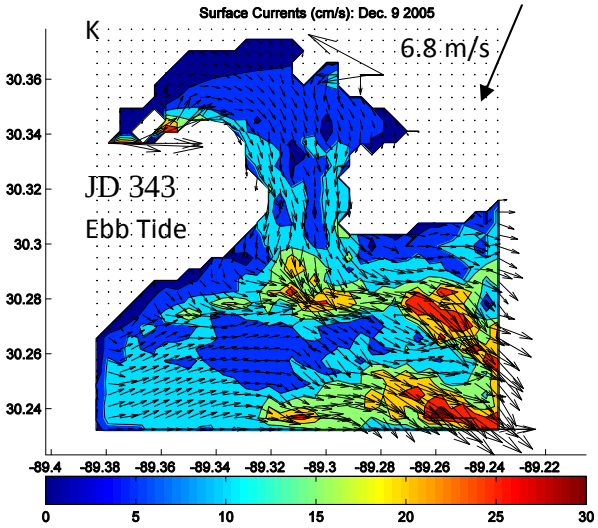
Surface Currents (cm/s): Dec. 9 2005
K
6.8 m/s
JD 343
Ebb Tide

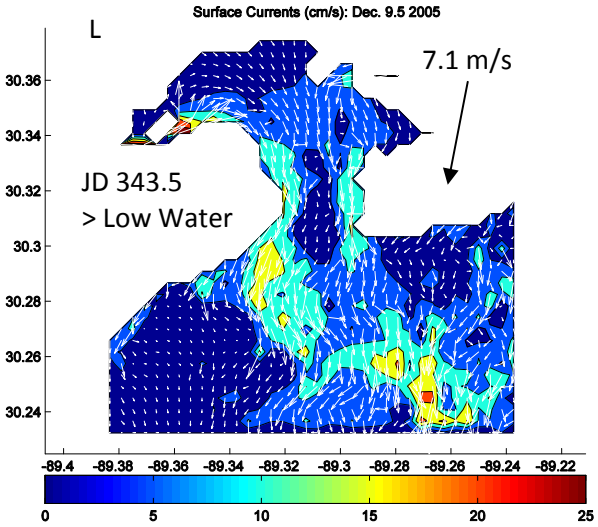
Surface Currents (cm/s): Dec. 9.5 2005
L
7.1 m/s
JD 343.5
> Low Water

Figure 6.15. Snapshots of surface currents calculated by NCOM every 12 hr between 0000 UT Dec. 4 and 1200 UT Dec. 9, 2005. Key: arrows = wind direction; wind speed is indicated next to the arrows; > indicates within 3 hr (model output interval) since slack water; ~ indicates difficulty of reading water level (see Fig. 6.7).

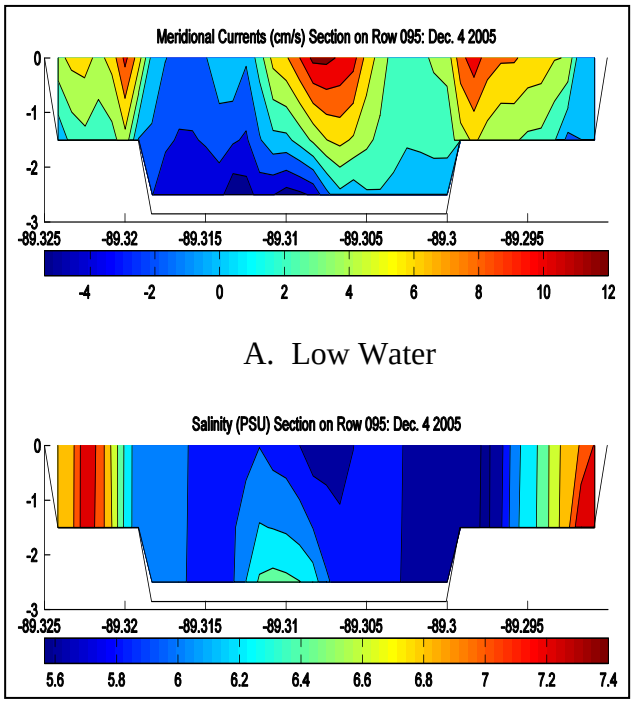

A. Low Water

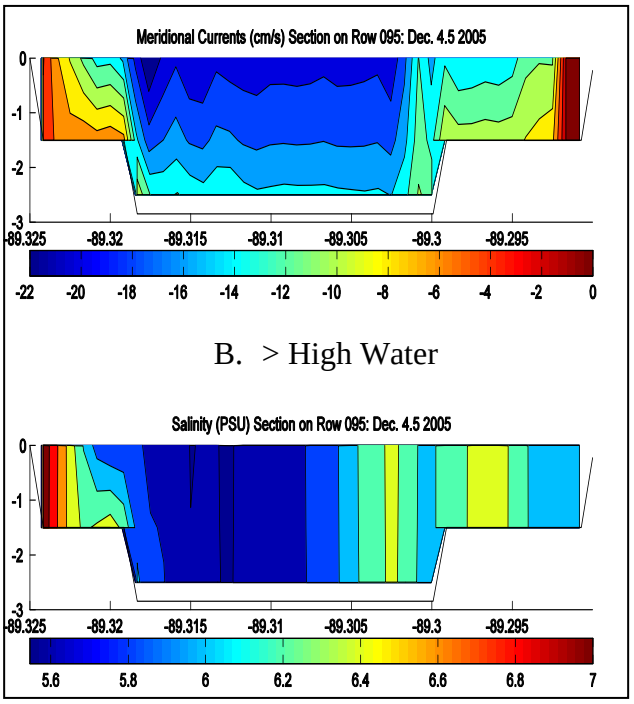

B. > High Water

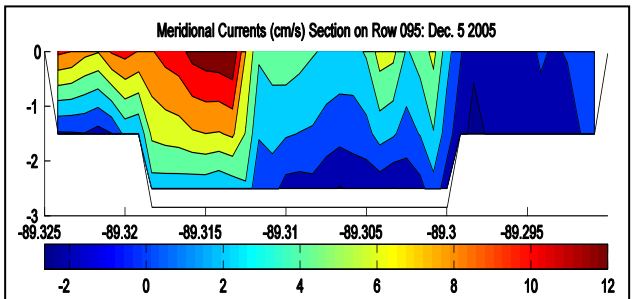

C. Low Water

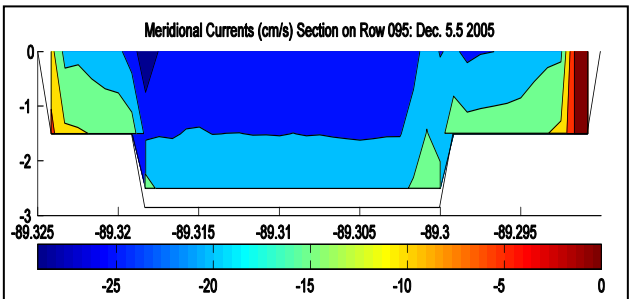

D. High Water

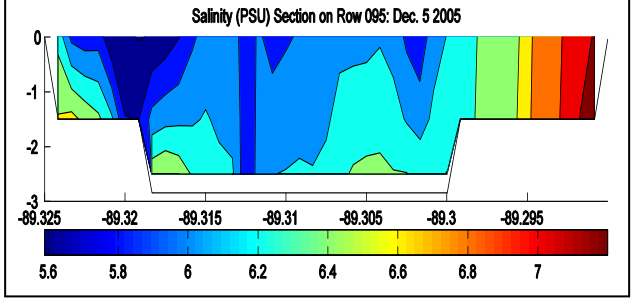

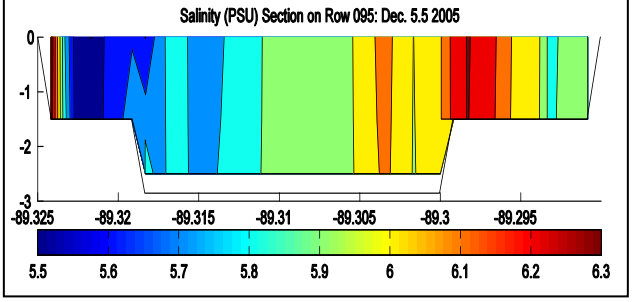

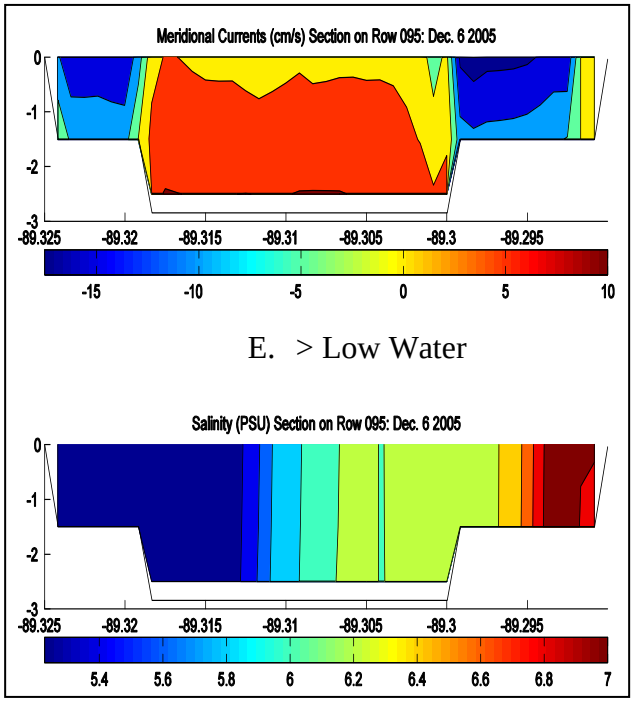

E. > Low Water

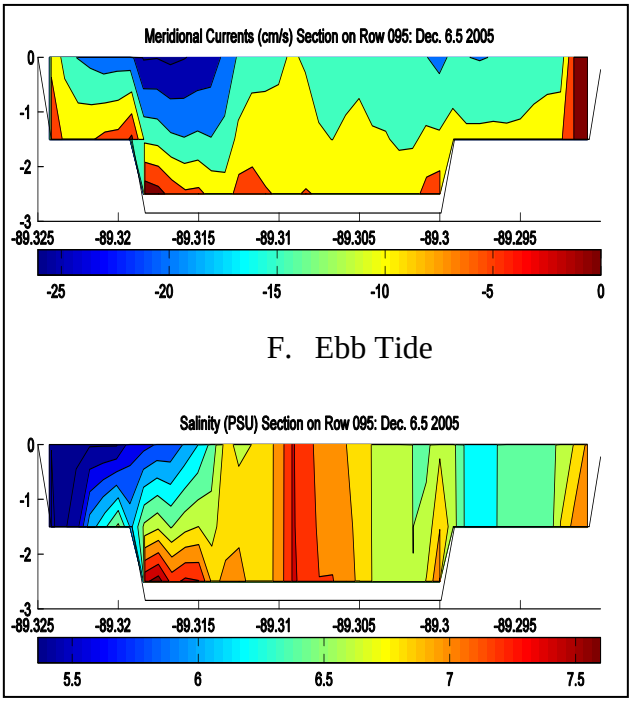

F. Ebb Tide

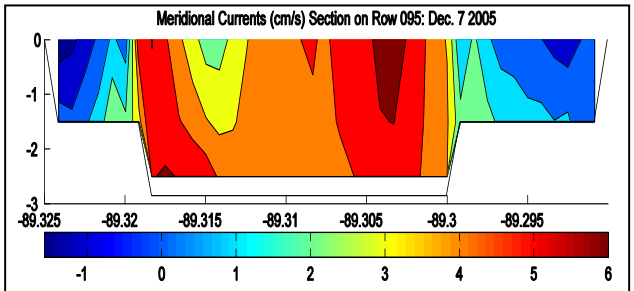

G. Flood Tide

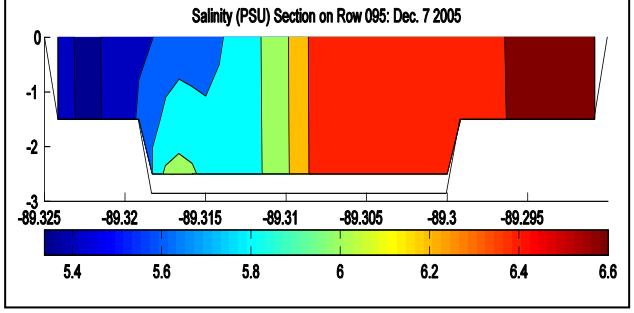

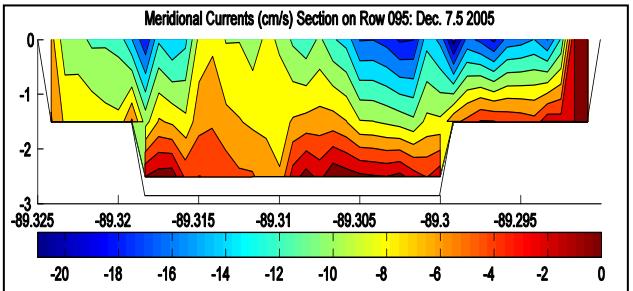

H. > High Water

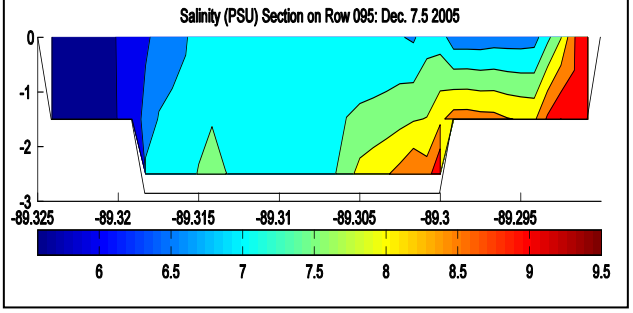

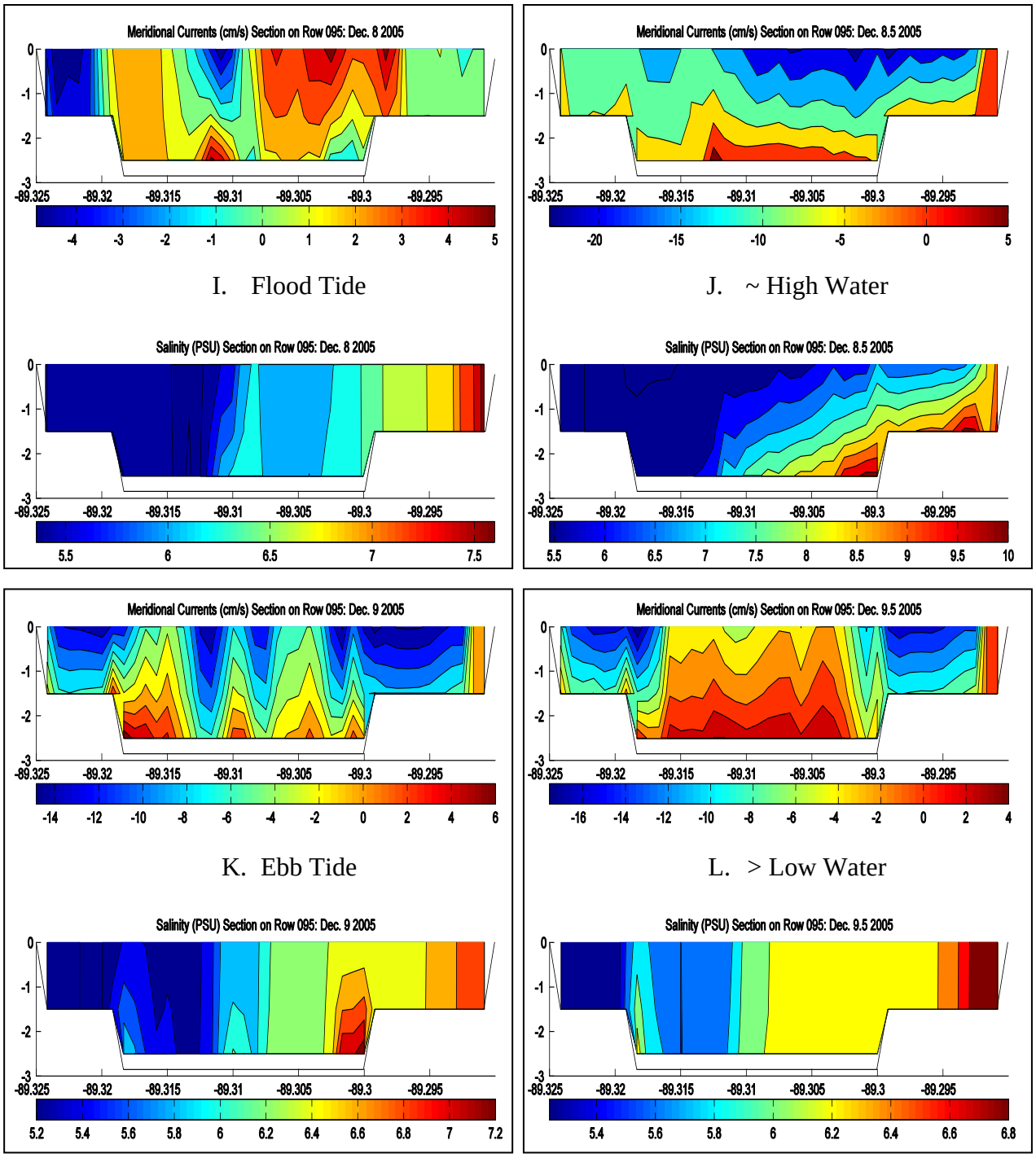

Figure 6.16. Sections of meridional currents (upper panels) and salinity (lower panels) computed by NCOM at 12 hr intervals between 0000 UT Dec. 4 and 1200 UT Dec. 9. The E-W section is across the entrance to St. Louis Bay at row 95 (30.3108N). Key: > indicates within 3 hr (model output interval) since slack water; ~ indicates difficulty of reading water level (see Fig. 6.7).

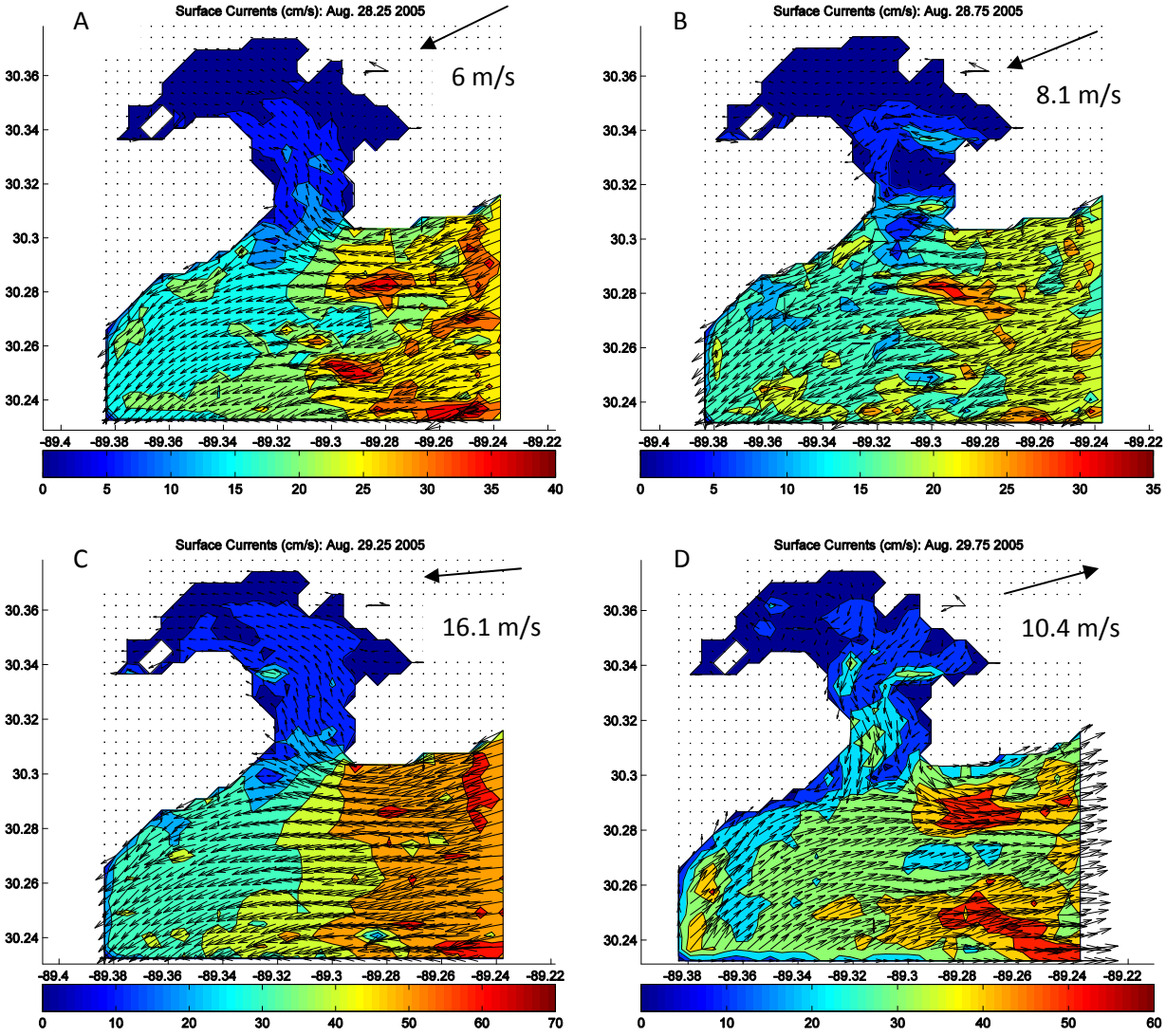
A
Surface Currents (cm/s): Aug. 28.25 2005
6 m/s
B
Surface Currents (cm/s): Aug. 28.75 2005
8.1 m/s
C
Surface Currents (cm/s): Aug. 29.25 2005
16.1 m/s
D
Surface Currents (cm/s): Aug. 29.75 2005
10.4 m/s

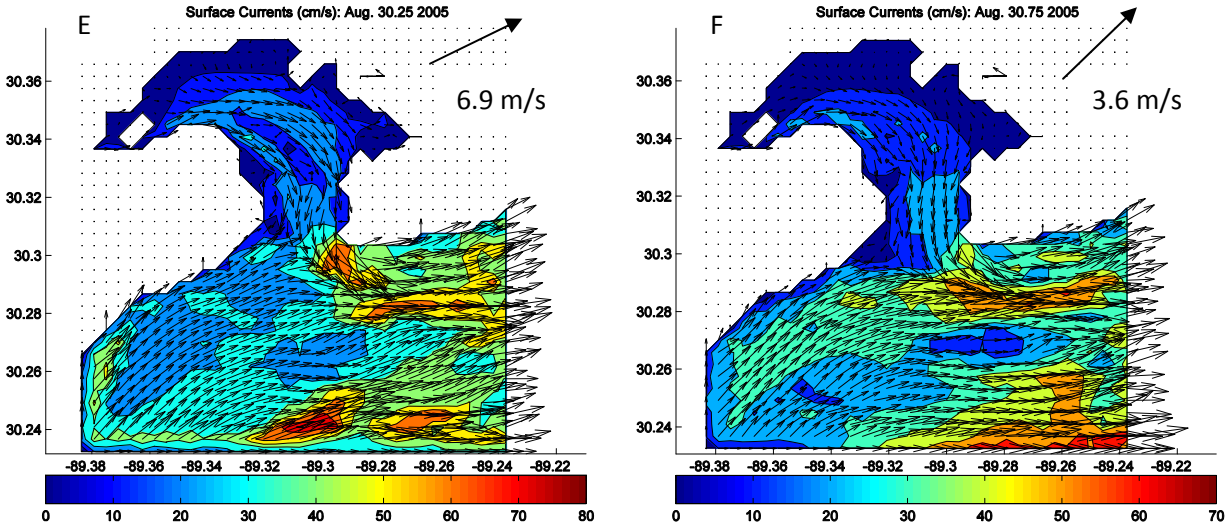

Figure 6.17. Snapshots of surface currents computed by NCOM on the SLB grid during Hurricane Katrina in 2005. (A) 0600 UT Aug. 28; (B) 1800 UT Aug. 28; (C) 0600 UT Aug. 29; (D) 1800 UT Aug. 29; (E) 0600 UT Aug 30; (F) 1800 UT Aug. 30. This simulation included tides and river inflow.

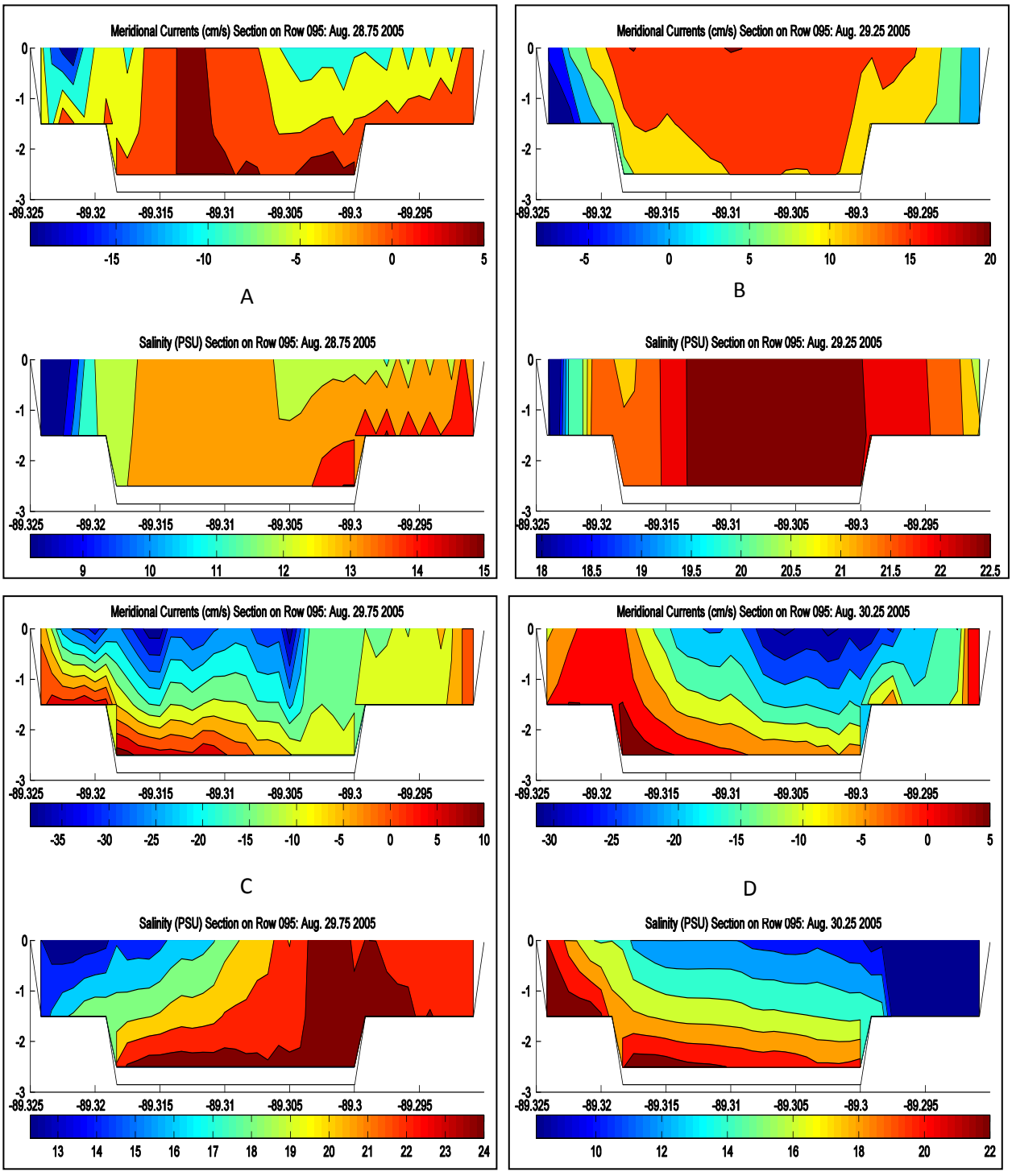

Figure 6.18. Sections of meridional currents (upper panels) and salinity (lower panels) computed by NCOM during Hurricane Katrina in 2005: (A) 1800 UT Aug. 28; (B) 0600 UT Aug. 29; (C) 1800 UT Aug. 30; (D) 0600 UT Aug. 30. The E-W section is across the narrow entrance to St. Louis Bay at row 95 (30.3108N).

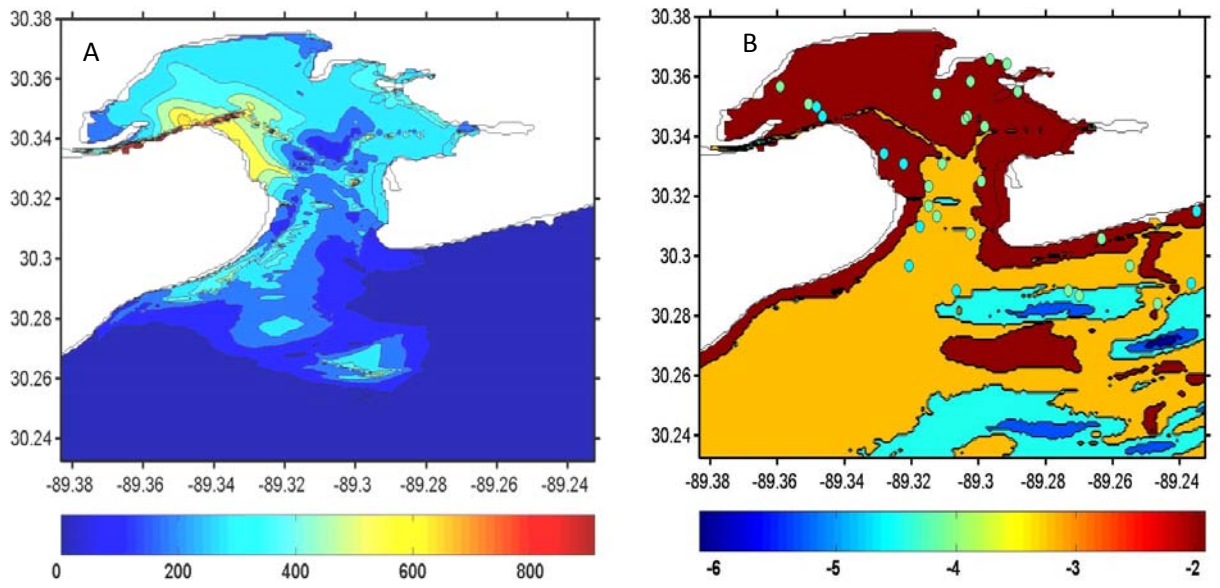

Figure 6.19. Results from HQCM computations for Aug. 2005. (A) Tracer concentration on Aug. 30. (B) Particle distribution for particles released every 18 hr at the Jourdan (blue circles) and Wolf (green circles) Rivers. The particle locations were printed every 72 hr. Forcing came from NCOM on the SLB grid.

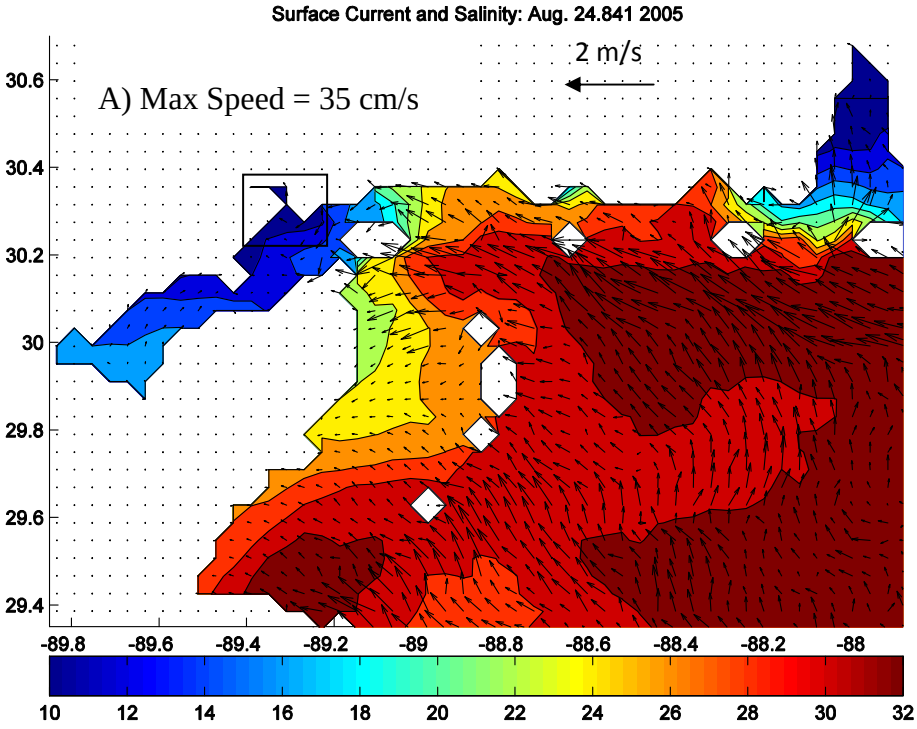
Surface Current and Salinity: Aug. 24.841 2005
2 m/s
A) Max Speed = 35 cm/s
30.6
30.4
30.2
30
29.8
29.6
29.4
-89.8 -89.6 -89.4 -89.2 -89 -88.8 -88.6 -88.4 -88.2 -88
10 12 14 16 18 20 22 24 26 28 30 32

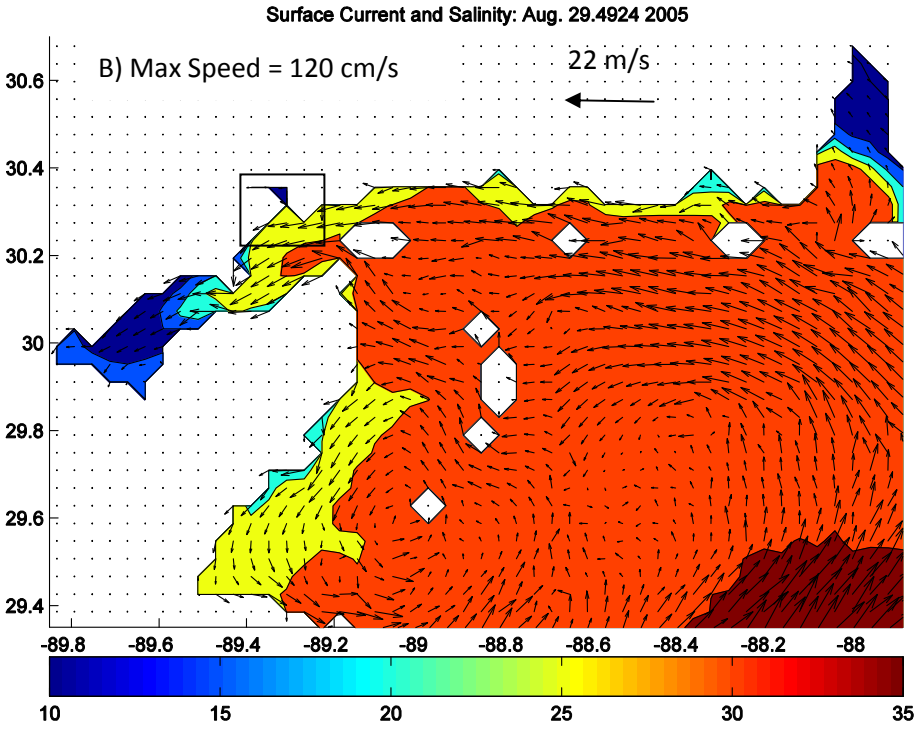
Surface Current and Salinity: Aug. 29.4924 2005
B) Max Speed = 120 cm/s
22 m/s
30.6
30.4
30.2
30
29.8
29.6
29.4
-89.8 -89.6 -89.4 -89.2 -89 -88.8 -88.6 -88.4 -88.2 -88
10 15 20 25 30 35

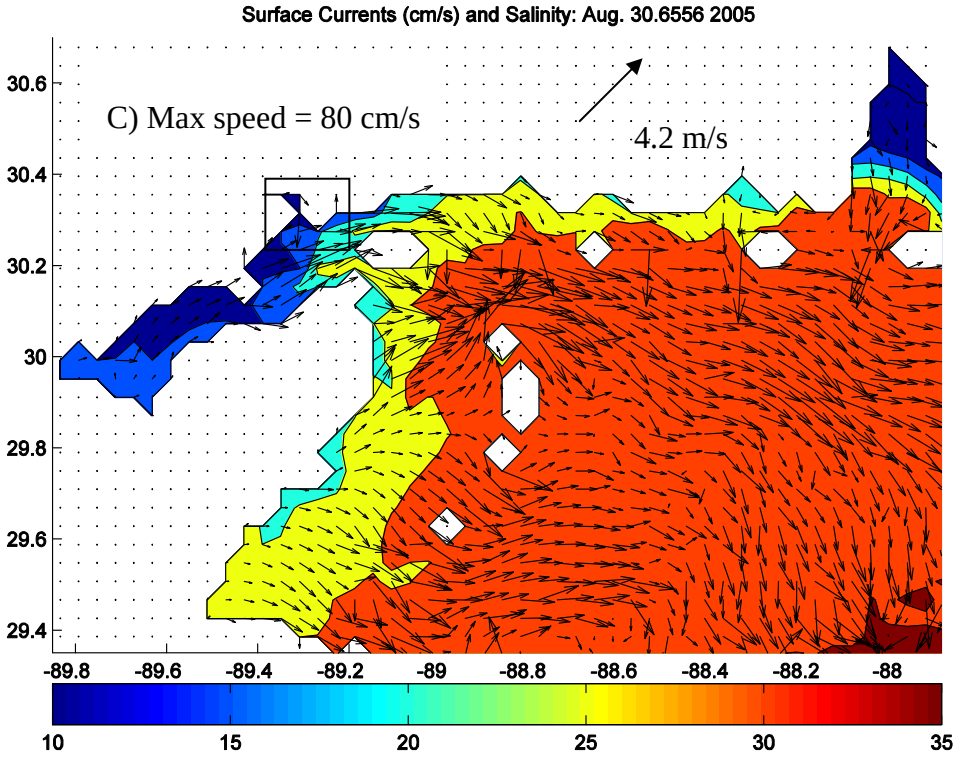

Figure 6.20. Surface current vectors plotted over contours of salinity calculated by NCOM on the MSB grid during Hurricane Katrina: (A) 2000 UT Aug. 24, 111 hr before landfall; (B) 1100 UT Aug. 29, as the eye made landfall. (C) 1330 UT Aug. 30, 26.5 hr after landfall. The rectangle outlines the SLB grid.

7 Summary

This report has presented results from four simulation studies of estuaries. These studies were useful in determining the best approach for further coastal modeling work. The Mullica-Great Bay and Kotar-Boka Bay studies were fundamental in this effort because they helped determine the approach used in the San Francisco Bay and St. Louis Bay work. Two basic concepts have come from these studies: (1) the estuary as a transitional environment; and (2) the need for a broad multi-scale and multi-model approach to estuarine modeling.

7.1 The estuary as a transitional environment

It is convenient to define a transitional littoral environment from a kinematic perspective. The totality of motion within a geographic region is determined by processes that are generated within it (internal) and processes that propagate from elsewhere. An example of internal kinematics would be wind-generated currents like those within St. Louis Bay due to the local wind stress. The tidal currents, however, are externally driven by the tidal wave propagating from the Gulf of Mexico. A second external process acting on SLB is the inflow of fresh water from rivers and bayous. Section 6 demonstrates how these internal and external processes interact to determine flow within SLB and export of water and dissolved constituents to Mississippi Sound. These processes contribute equally to the model result on synoptic time scales, even during an extreme flow event like Hurricane Katrina. Thus, the overlapping kinematics of St. Louis Bay is representative of its position as an intermediary environment between Mississippi Sound and the Jourdan River (for example). We can identify the kinematic components of a transitional environment using models or observations.

Most littoral regions are influenced by multiple processes; therefore, we must refine the kinematic definition if it is to be of practical use. The relative magnitudes of internal and external processes identified from model results or observations within a transitional environment are subequal. The south basin of Hunters Point (SBHP) in San Francisco Bay (section 5 of this report) is a good example. The bottom tidal currents in SBHP are ≈ 5 cm/s whereas the peak currents during wind events are ≈ 10 cm/s. The tides are external and the wind currents are internal but, as was shown in section 5, they both contribute to net export of suspended material from the basin at time scales of hours to days. Furthermore, waves only enter SBHP through an inlet from SFB when the wind is southeasterly (local waves are < 1 cm). Theses external waves have bottom orbital speeds of 3-20 cm/s, which is of the same magnitude as the tides. A third critical external process in this tidal basin is the water depth, which responds to both tides and subtidal variations. The combined impact of these water level anomalies on circulation were not discussed in this report because a circulation model for intertidal flow (i.e., wetting and drying) was unavailable. The water level does affect the relationship between the wave height and bottom orbital speed, however, and thus it influences bottom sediment resuspension and, ultimately, toxin release from the seabed. This example

demonstrates the complex interaction of internal and external processes in transitional environments.

The littoral environments discussed in this report span a range of spatial scales: the south basin at Hunters Point is < 0.5 km^2 whereas Mississippi Sound is ≈ 5000 km^2 (USEPA 1999). Whereas it is convenient to define estuaries, bays, and coasts as transitional, it would not be particularly useful to apply the transitional environment definition to larger areas because they do not reflect a range of processes that require different modeling approaches. For example the Middle Atlantic Bight of N. America is impacted by currents from tides (external), wind (internal), the Gulf Stream (external), baroclinic coastal currents (external), shelf waves (internal), and internal waves (internal/external). However, most of these currents can be represented by a single conceptual/numerical modeling approach (i.e., NCOM or a similar primitive equation model). This contrast exemplifies the purpose of defining a transitional environment. This definition aids in identifying kinematic subregions (KSR's) within a larger domain of interest that may require different approaches for measurement and modeling. The examples in this report demonstrate this concept as it applies to intertidal processes. Tidal flats are impacted by processes that cannot be conceptually or numerically included in a model of coastal flow (e.g., sheet flow, channelization, nonhomgeneous sediment properties, and bioturbation). This KSR was not incorporated in the models that were applied in these studies and this omission had unknown and unquantified impacts on the results.

Estuaries contain other KSR's as well. One of the least understood kinematic zones in most estuaries is the inlet. Bar-built estuaries often have multiple inlets between barrier islands. The processes within these channels vary with location and time and they are not well understood (Barnard and Davis 1999; Davis 1999; McBride 1999). Drowned river valleys like Chesapeake Bay have only one inlet, although compound estuaries can have bay mouth bars as well. These inlets are characterized by changes in channel depth at a range of temporal scales due to external processes interacting with a movable bottom. Despite their relative simplicity, circulation in and near these inlets has not been studied in depth (Chen and Sanford 2009). Another important KSR within estuaries is the estuarine turbidity maximum (ETM). The ETM is characterized by large gradients in salinity, temperature, and suspended solids. Fine sediment dynamics within this KSR are currently being examined in the NRL 6.1 project, "Transport and mixing of terrigenous material in the coastal ocean".

7.2 Multiscale and multimodeling approaches in estuaries

Many problems in coastal oceanography have typically been addressed using numerical models that include one physical model acting on a single scale. This approach is apparent in models that use only one spatial scale and one model grid. It is not as obvious in studies that use nested models like the Hunters Point and St. Louis Bay examples discussed in this report. The nested grids used NCOM and the nesting was done simple to resolve the size of the tidal basin at

Hunters Point. The hydrodynamic results appear reasonable but we do not know what information was lost by applying the same assumptions about the flow at this scale as at the estuary scale. The key questions in both of these studies required consideration of multiple interacting models and scales to represent the processes of interest–i.e., contaminant release from bottom sediments and transport by combined flows. These studies did not adequately address this fundamental problem because they did not include the appropriate models for the relevant scales (Delalondre, Smith et al.).

Two kinematic subregions within San Francisco Bay and the Mississippi Sound estuary system were omitted because they could not be resolved physically by NCOM, which was designed to be coupled to an atmospheric model for application to shelf seas. The SFB simulations utilized a suite of numerical models that included multiphysics and multiscale phenomena (e.g., wave generation, wave-current interaction in the bottom boundary layer, and sediment resuspension). The incorporation of these different scales and models made that study more realistic despite the errors associated with the use of a shelf-scale model in a tidal basin. The MSB/SLB simulations did not use the same multimodel approach because of the logistical difficulties of manually linking the models in a domain with no obvious physical constraints like the small size of SBHP. It has been demonstrated that interaction between currents and waves can be significant in semi-enclosed water bodies like SBHP and SLB (Cobb and Blain 2002). Tides are an important external process in these bays and the lack of intertidal hydrodynamics probably had a negative impact in both studies. This process should be included in all littoral hydrodynamic simulations. This necessity has been noted by the hydrodynamic modeling community and has motivated several approaches to include wetting and drying of grid cells in primitive equation models (Leuttich, Westerink et al. 1992; Cheng, Casulli et al. 1993; Haas and Warner 2009). These approaches address the kinematic problem of drying cells but they do not include the physics of intertidal mud and sand flats (Allen 1985; Dyer 2000; Di Silvio, Lanzoni et al. 2008). The bay/estuary inlet has been studied less than intertidal areas because it has less economical value; however, it is an important KSR in estuaries characterized by mobile beds (Ludwick 1974; Koutitonsky 1979; Berne, Castaing et al. 1993; Teles and Barata 2005). The morphology within this KSR has been simulated using the Delf3D modeling system (Marciano, Wang et al. 2005; Nghiem, Le et al. 2009; Tung, Walstra et al. 2009; Xie, Wang et al. 2009).

There are a number of coupling strategies currently being implemented by different groups for a range of research problems (Delalondre, Smith et al.). The Earth System Modeling Framework (ESMF) has been proposed specifically for earth sciences applications (Hill, DeLuca et al. 2004). These approaches are necessary to link the multiscale/multiphysics models that are applicable to the KSR's within transitional environments. There are difficulties associated with implementing each of them but a coupling system must be implemented if substantial progress is to be made in linking the different kinematic subregions that exist in estuaries. As difficult as such an effort may be, it is easier and more flexible than incorporating all of the physics and

scales into a single model of transitional environments as has been done with ROMS (Warner, Sherwood et al. 2008) and Delf3D (Postma, Boderie et al. 2003).

8 References

Able, K. W., R. Lathrop, et al. (1996). Background for research and monitoring in the Mullica River - Great Bay Estuary. Technical Report. New Brunswick, New Jersey, Institute of Marine and Coastal Science. **Contribution No. 96-07**.

Abril, G., H. Etcheber, et al. (1999). "Oxic/anoxic oscillations and organic carbon mineralization in an estuarine maximum turbidity zone (The Gironde, France)." Limnology and Oceanography **44**(5): 1304-1315.

Ahsan, Q., C. N. Barron, et al. (2001). Northern Gulf of Mexico Littoral Initiative Modeling Program, St. Petersburg, Florida, A.S.C.E.

Ahsan, Q., A. F. Blumberg, et al. (2001). Forecasting the environment of the littoral waters in the northern Gulf of Mexico. Estuarine and Coastal Modeling, St. Petersburg, Florida, A.S.C.E.

Allard, R., A. Wallcraft, et al. (2003). "Providing the Warfighter Information Superiority in Littoral Waters " High Performance Computing Contributions to DOD Mission Success 2002(March): 78-80.

Allen, G. P., J. C. Salomon, et al. (1980). "Effects of Tides on Mixing and Suspended Sediment Transport in Macro-Tidal Estuaries." Sedimentary Geology **26**(1-3): 69-90.

Allen, J. R. L. (1985). "Intertidal Drainage and Mass-Movement Processes in the Severn Estuary - Rills and Creeks (Pills)." Journal of the Geological Society **142**(Sep): 849-861.

Anonymous (1998). A Primer for ECOMSED Version 1.1. 1 Lethbridge Plaza, Mahwah, New Jersey, HydroQual, Inc.**:** 156.

Anthony, E. J. (2004). "Sediment dynamics and morphological stability of estuarine mangrove swamps in Sherbro Bay, West Africa." Marine Geology **208**(2-4): 207-224.

Aoki, K. and A. Isobe (2006). "Numerical study of the summer temperature decrease induced by the enhancement of estuarine circulation in Fukuoka Bay." Journal of Oceanography **62**(2): 207-217.

Barnard, P. L. and R. A. Davis (1999). Anthropogenic vs. natural influences on inlet evolution: West-Central Florida. New York, Amer Soc Civil Engineers.

Barron, C. N., L. F. Smedstad, et al. (2004). "Validation of the 1/8_ global Navy Coastal Ocean Model nowcast/forecast system,." Navigator **Spring 2004**: 5-8.

Battelle, ENTRIX, et al. (2002). Hunters Point Shipyard Parcel F Validation Study Report, San Francisco Bay, California. 1220 Pacific Highway, San Diego, California, U.S. Navy NAVFAC**:** 255.

Bentley, S. J., T. R. Keen, et al. (2002). "The origin and preservation of a major hurricane event bed in the northern Gulf of Mexico: Hurricane Camille, 1969." Marine Geology **186**(3-4): 423-446.

Berne, S., P. Castaing, et al. (1993). "Morphology, Internal Structure, and Reversal of Asymmetry of Large Subtidal Dunes in the Entrance to Gironde Estuary (France)." Journal of Sedimentary Petrology **63**(5): 780-793.

Bever, A. J., C. K. Harris, et al. (2009). "Deposition and flux of sediment from the Po River, Italy: An idealized and wintertime numerical modeling study." Marine Geology **260**(1-4): 69-80.

Bianchi, T. S., S. F. DiMarco, et al. (2010). "The science of hypoxia in the Northern Gulf of Mexico: A review." Science of the Total Environment **408**(7): 1471-1484.

Blain, C. A. and C. R. Edwards (2002). "Development of a forecast capability for coastal embayments of the Mississippi Sound." Oceans 2002 Mts/Ieee Conference & Exhibition, Vols 1-4, Conference Proceedings: 1501-1508.

Blumberg, A. F., Q. Ahsan, et al. (2000). "Modeling hydrodynamics of the Mississippi Sound and adjoining rivers, bays and shelf waters." Oceans 2000 Mts/Ieee - Where Marine Science and Technology Meet, Vols 1-3, Conference Proceedings: 1983-1989.

Blumberg, A. F., Q. Ahsan, et al. (2002). "An operational forecast modeling system for the Mississippi Sound/Bight." Oceans 2002 Mts/Ieee Conference & Exhibition, Vols 1-4, Conference Proceedings: 816-822.

Bogen, J. (1983). "MORPHOLOGY AND SEDIMENTOLOGY OF DELTAS IN FJORD AND FJORD VALLEY LAKES." Sedimentary Geology **36**(2-4): 245-267.

Bogunovic, B. and V. Malacic (2008). "Circulation in the Gulf of Trieste: Measurements and model results." Nuovo Cimento Della Societa Italiana Di Fisica C-Geophysics and Space Physics **31**(3): 301-326.

Castanedo, S., R. Medina, et al. (2006). "The Prestige oil spill in Cantabria (Bay of Biscay). Part I: Operational forecasting system for quick response, risk assessment, and protection of natural resources." Journal of Coastal Research **22**(6): 1474-+.

Casulli, V. and E. Cattani (1994). "STABILITY, ACCURACY AND EFFICIENCY OF A SEMIIMPLICIT METHOD FOR 3-DIMENSIONAL SHALLOW-WATER FLOW." Computers & Mathematics with Applications **27**(4): 99-112.

Casulli, V. and R. T. Cheng (1992). "SEMIIMPLICIT FINITE-DIFFERENCE METHODS FOR 3-DIMENSIONAL SHALLOW-WATER FLOW." International Journal for Numerical Methods in Fluids **15**(6): 629-648.

Chaney, P. L. and G. W. Stone (1996). "Soundside erosion of a nourished beach and implications for winter cold front forcing: West Ship Island, Mississippi." Shore and Beach **64**: 27-33.

Chaudhary, A. J., M. U. Hassan, et al. (2009). "Simultaneous recovery of metals and degradation of organic species: Copper and 2,4,5-trichlorophenoxyacetic acid (2,4,5-T)." Journal of Hazardous Materials **165**(1-3): 825-831.

Chen, C. Y., N. Serrell, et al. (2008). "Meeting Report: Methylmercury in Marine Ecosystems-From Sources to Seafood Consumers." Environmental Health Perspectives **116**(12): 1706-1712.

Chen, J., Y. Li, et al. (2004). "Amino acids in the Pearl River Estuary and adjacent waters: origins, transformation and degradation." Continental Shelf Research **24**(16): 1877-1894.

Chen, S. N. and L. P. Sanford (2009). "Lateral circulation driven by boundary mixing and the associated transport of sediments in idealized partially mixed estuaries." Continental Shelf Research **29**(1): 101-118.

Cheng, R. T., V. Casulli, et al. (1993). "Tidal, Residual, Intertidal Mudflat (TRIM) Model and its Applications to San Francisco Bay, California." Estuarine, Coastal and Shelf Science **36**(3): 235-280.

Cheng, R. T., R. E. Smith, et al. (1998). A nowcast model for tides and tidal currents in San Francisco Bay, California. Washington, Marine Technology Soc.

Chigbu, P., S. Gordon, et al. (2004). "Influence of inter-annual variations in climatic factors on fecal coliform levels in Mississippi Sound." Water Research **38**(20): 4341-4352.

Chigbu, P., T. Strange, et al. (2006). "A decision support tool for shellfish management in Mississippi Sound." Journal of Shellfish Research **25**(3): 1091-1099.

Cipriani, L. E. and G. W. Stone (2001). "Net longshore sediment transport and textural changes in beach sediments along the southwest Alabama and Mississippi barrier islands, USA." Journal of Coastal Research **17**(2): 443-458.

Cloern, J. E. (1984). "TEMPORAL DYNAMICS AND ECOLOGICAL SIGNIFICANCE OF SALINITY STRATIFICATION IN AN ESTUARY (SOUTH SAN-FRANCISCO BAY, USA)." Oceanologica Acta **7**(1): 137-141.

Cloern, J. E., E. A. Canuel, et al. (2002). "Stable carbon and nitrogen isotope composition of aquatic and terrestrial plants of the San Francisco Bay estuarine system." Limnology and Oceanography **47**(3): 713-729.

Cobb, M. and C. A. Blain (2002). "Simulating wave-tide induced circulation in Bay St. Louis, MS with a coupled hydrodynamic-wave model." Oceans 2002 Mts/Ieee Conference & Exhibition, Vols 1-4, Conference Proceedings: 1494-1500.

Cobb, M., T. R. Keen, et al. (2008). "Modeling the circulation of the Atchafalaya Bay system during winter cold front events. Part 1: Model description and validation." Journal of Coastal Research **24**(4): 1036-1047.

Coonley, L. S., E. B. Baker, et al. (1971). "Iron in Mullica River and in Great Bay, New Jersey." Chemical Geology **7**(1): 51-&.

Corson, W., J. Rhee, et al. (2002). "Water-level and directional wave data collection in Mississippi sound and the Gulf of Mexico near Pascagoula, MS." Oceans 2002 Mts/Ieee Conference & Exhibition, Vols 1-4, Conference Proceedings: 525-529.

Crout, R. L., A. R. Diercks, et al. (2001). Mobile Bay response to a strong autumn cold front passage.

Cucco, A. and G. Unigiesser (2006). "Modeling the Venice lagoon residence time." Ecological Modelling **193**(1-2): 34-51.

Cushman-Roisin, B. and K. A. Korotenko (2007). "Mesoscale-resolving simulations of summer and winter bora events in the Adriatic Sea." Journal of Geophysical Research-Oceans **112**(C11): 12.

Cushman-Roisin, B. and C. E. Naimie (2002). "A 3D finite-element model of the Adriatic tides." Journal of Marine Systems **37**(4): 279-297.

Davis, R. A. (1999). Complicated littoral drift systems on the Gulf Coast of peninsular Florida. New York, Amer Soc Civil Engineers.

Delalondre, F., C. Smith, et al. "Collaborative software infrastructure for adaptive multiple model simulation." Computer Methods in Applied Mechanics and Engineering **199**(21-22): 1352-1370.

Delle Site, A. (2001). "Factors affecting sorption of organic compounds in natural sorbent/water systems and sorption coefficients for selected pollutants. A review." Journal of Physical and Chemical Reference Data **30**(1): 187-439.

Deloffre, J., R. Verney, et al. (2007). "Sedimentation on intertidal mudflats in the lower part of macrotidal estuaries: Sedimentation rhythms and their preservation." Marine Geology **241**(1-4): 19-32.

Denisoff, C. and M. Movassaghi (1998). Regional wetlands planning: A case study of coastal wetlands planning in the San Francisco Bay area & southern California. New York, Amer Soc Civil Engineers.

Di Silvio, G., S. Lanzoni, et al. (2008). "Comparative results of tidal and intertidal numerical simulation of dispersion processes." River, Coastal and Estuarine Morphodynamics: Rcem 2007, Vols 1 and 2: 491-497.

Dickhudt, P. J., C. T. Friedrichs, et al. (2009). "Spatial and temporal variation in cohesive sediment erodibility in the York River estuary, eastern USA: A biologically influenced equilibrium modified by seasonal deposition." Marine Geology **267**(3-4): 128-140.

Dortch, M. S., M. Zakikhani, et al. (2007). Application of a Water Quality Model to Mississippi Sound to Evaluate Impacts of Freshwater Diversions. Vicksburg, U.S. Army Engineer Research and Development Center**:** 888.

Doxaran, D., J.-M. Froidefond, et al. (2002). "Spectral signature of highly turbid waters: Application with SPOT data to quantify suspended particulate matter concentrations." Remote Sensing of Environment **81**(1): 149-161.

Duffus, J. H. (2002). ""Heavy metals" - A meaningless term? (IUPAC technical report)." Pure and Applied Chemistry **74**(5): 793-807.

Dyer, K. (2000). "Intertidal mudflats: Properties and processes - Part I: Mudflat properties - Preface." Continental Shelf Research **20**(10-11): 1037-1038.

Dyer, K. R., M. C. Christie, et al. (2004). "The effects of suspended sediment on turbulence within an estuarine turbidity maximum." Estuarine, Coastal and Shelf Science **59**(2): 237-248.

Eleuterius, C. K. (1977). "Location of Mississippi Sound Oyster Reefs as Related to Salinity of Bottom Waters during 1973-1975." Gulf Research Reports **6**(1): 17-23.

Eleuterius, C. K. (1978). "Classification of Mississippi Sound as to Estuary Hydrological Type." Gulf Research Reports **6**(2): 185-187.

Elston, R., E. W. Cake, et al. (2005). "Dioxin and heavy-metal contamination of shellfish and sediments in St. Louis Bay, Mississippi and adjacent marine waters." Journal of Shellfish Research **24**(1): 227-241.

Erdner, D. L., J. Dyble, et al. (2008). "Centers for Oceans and Human Health: a unified approach to the challenge of harmful algal blooms." Environmental Health **7**: -.

Fairbridge, R. W. (1980). The estuary: Its definition and geodynamic cycle. Chemistry and Biogeochemistry of Estuaries. E. Olausson and I. Cato. New York, Wiley**:** 1-35.

Ferrarese, S., C. Cassardo, et al. (2008). "Response of temperature and sea surface circulation to a Sirocco wind event in the Adriatic basin: A model simulation." Journal of Marine Systems **74**(1-2): 659-671.

Festa, J. F. and D. V. Hansen (1976). "2-DIMENSIONAL NUMERICAL-MODEL OF ESTUARINE CIRCULATION - EFFECTS OF ALTERING DEPTH AND RIVER DISCHARGE." Estuarine and Coastal Marine Science **4**(3): 309-323.

Franks, J. S., J. R. Hendon, et al. (2004). "Red snapper (Lutjanus campechanus) associated with a small artificial structure in the Mississippi sound, a northern Gulf of Mexico estuary." Proceedings of the Fifty-Fifth Annual Gulf and Caribbean Fisheries Institute: 853-864.

Gacic, M., V. Kovacevic, et al. (2009). "Surface current patterns in front of the Venice Lagoon." Estuarine, Coastal and Shelf Science **82**(3): 485-494.

Galt, J. A., R. T. Cheng, et al. (1997). "Current pattern analysis for oil-spills - A case study using San Francisco Bay." Oceans '97 Mts/Ieee Conference Proceedings, Vols 1 and 2: 1448-1452.

Geyer, W. R., R. P. Signell, et al. (1993). Lateral trapping of sediment in a partially mixed estuary. Physics of estuaries and coastal seas. J. Dronkers and M. B. A. M. Scheffers. Rotterdam, The Netherlands, A.A. Balkema**:** 115-124.

Gibbs, R. J. (1967). "GEOCHEMISTRY OF AMAZON RIVER SYSTEM .I. FACTORS THAT CONTROL SALINITY AND COMPOSITION AND CONCENTRATION OF SUSPENDED SOLIDS." Geological Society of America Bulletin **78**(10): 1203-&.

Goni, M. A., M. W. Cathey, et al. (2005). "Fluxes and sources of suspended organic matter in an estuarine turbidity maximum region during low discharge conditions." Estuarine Coastal and Shelf Science **63**(4): 683-700.

Grenz, C., J. E. Cloern, et al. (2000). "Dynamics of nutrient cycling and related benthic nutrient and oxygen fluxes during a spring phytoplankton bloom in South San Francisco Bay (USA)." Marine Ecology-Progress Series **197**: 67-80.

Gross, E. S., V. Casulli, et al. (1998). "A semi-implicit method for vertical transport in multidimensional models." International Journal for Numerical Methods in Fluids **28**(1): 157-186.

Gross, E. S., J. R. Koseff, et al. (1999). Salinity simulations in San Francisco Bay. Leiden, A a Balkema Publishers.

Gross, E. S., J. R. Koseff, et al. (1999). "Three-dimensional salinity simulations of south San Francisco Bay." Journal of Hydraulic Engineering-Asce **125**(11): 1199-1209.

Gross, E. S. and M. T. Stacey (2004). Three-dimensional hydrodynamic modeling of Tomales Bay, California. New York, Amer Soc Civil Engineers.

Guo, X. Y. and A. Valle-Levinson (2007). "Tidal effects on estuarine circulation and outflow plume in the Chesapeake Bay." Continental Shelf Research **27**(1): 20-42.

Haas, K. A. and J. C. Warner (2009). "Comparing a quasi-3D to a full 3D nearshore circulation model: SHORECIRC and ROMS." Ocean Modelling **26**(1-2): 91-103.

Harris, C. K., C. R. Sherwood, et al. (2008). "Sediment dispersal in the northwestern Adriatic Sea." Journal of Geophysical Research - Part C - Oceans **113**(C11): C11S03 (18 pp.)-C11S03 (18 pp.).

Hayes, M. O. and R. B. Nairn (2004). "Natural maintenance of sand ridges and linear shoals on the US Gulf and Atlantic continental shelves and the potential impacts of dredging." Journal of Coastal Research **20**(1): 138-148.

Hill, C., C. DeLuca, et al. (2004). "The architecture of the earth system modeling framework." Computing in Science & Engineering **6**(1): 18-28.

Hoffmayer, E. R. and G. R. Parsons (2003). "Food habits of three shark species from the Mississippi Sound in the northern Gulf of Mexico." Southeastern Naturalist **2**(2): 271-280.

Hollibaugh, J. T. and P. S. Wong (1999). "Microbial processes in the San Francisco Bay estuarine turbidity maximum." Estuaries **22**(4): 848-862.

Horvath, K., S. Ivatek-Sahdan, et al. (2009). "Evolution and Structure of Two Severe Cyclonic Bora Events: Contrast between the Northern and Southern Adriatic." Weather and Forecasting **24**(4): 946-964.

Hwang, H. M., P. G. Green, et al. (2009). "Historical trends of trace metals in a sediment core from a contaminated tidal salt marsh in San Francisco Bay." Environmental Geochemistry and Health **31**(4): 421-430.

Jackson, N. L. (2004). Estuary. Encyclopedia of Geomorpholgy. A. S. Goudie. London, Routledge. **1:** 341-344.

Jaffe, B. E., J. H. List, et al. (1997). "Massive sediment bypassing on the lower shoreface offshore of a wide tidal inlet -- Cat Island Pass, Louisiana." Marine Geology **136**(3-4): 131-149.

Jay, D. A. and J. D. Musiak (1994). "Particle Trapping in Estuarine Tidal Flows." Journal of Geophysical Research-Oceans **99**(C10): 20445-20461.

Karamanis, D., K. Stamoulis, et al. (2008). "Spatial and seasonal trends of natural radioactivity and heavy metals in river waters of Epirus, Macedonia and Thessalia." Desalination **224**(1-3): 250-260.

Keen, T. R. (2002). "Waves and currents during a winter cold front in the Mississippi bight, Gulf of Mexico: Implications for barrier island erosion." Journal of Coastal Research **18**(4): 622-636.

Keen, T. R., S. J. Bentley, et al. (2004). "The generation and preservation of multiple hurricane beds in the northern Gulf of Mexico." Marine Geology **210**(1-4): 79-105.

Keen, T. R. and Y. Furukawa (2007). A modular entrainment model for cohesive sediment. Estuarine and Coastal Fine Sediment Dynamics. J. P. Y. Maa. Gloucester Point, Virginia, Elsevier**:** 184-202.

Keen, T. R. and S. M. Glenn (1995). "A Coupled Hydrodynamic Bottom Boundary-Layer Model of Storm and Tidal Flow in the Middle Atlantic Bight of North-America." Journal of Physical Oceanography **25**(3): 391-406.

Keen, T. R. and S. M. Glenn (1999). "Shallow water currents during hurricane Andrew." Journal of Geophysical Research-Oceans **104**(C10): 23443-23458.

Keen, T. R. and F. Harding (2008). "Seasonal patterns of exchange between St. Louis Bay and Mississippi Sound, U.S.A." Eos, Transactions of the American Geophysical Union(Ocean Sciences Meeting, Orlando, Florida): OS-262.

Keen, T. R. and K. T. Holland (2010). The Coastal Dynamics of Heterogeneous Sedimentary Environments: Numerical Modeling of Nearshore Hydrodynamics and Sediment Transport. NRL Memorandum Report. Washington, D. C., Naval Research Laboratory**:** 101.

Keen, T. R., D. S. Ko, et al. (2006). "Potential transport pathways of terrigenous material in the Gulf of Papua." Geophysical Research Letters **33**(4): -.

Keen, T. R. and R. L. Slingerland (1993). "4 Storm-Event Beds and the Tropical Cyclones That Produced Them - a Numerical Hindcast." Journal of Sedimentary Petrology **63**(2): 218-232.

Keen, T. R. and R. H. Stavn (2000). Developing a capability to forecast coastal ocean optics: minerogenic scattering. 6th International Conference on Estuarine and Coastal Modeling, American Society of Civil Engineers**:** 178-193.

Keen, T. R., G. W. Stone, et al. (2003). Barrier island erosion during a winter cold front in Mississippi Sound. Coastal Sediments 2003, Clearwater Beach, Florida, American Society of Civil Engineers.

Kessarkar, P. M., V. P. Rao, et al. (2009). "Wind-driven estuarine turbidity maxima in Mandovi Estuary, central west coast of India." Journal of Earth System Science **118**(4): 369-377.

Kim, C. K., K. Park, et al. (2008). "Transport of oyster larvae in response to tide, river and wind conditions in mobile bay and the adjacent Eastern Mississippi Sound." Journal of Shellfish Research **27**(4): 1021-1021.

Kimmerer, W. J., E. S. Gross, et al. (2009). "Is the Response of Estuarine Nekton to Freshwater Flow in the San Francisco Estuary Explained by Variation in Habitat Volume?" Estuaries and Coasts **32**(2): 375-389.

Kineke, G. C., E. E. Higgins, et al. (2006). "Fine-sediment transport associated with cold-front passages on the shallow shelf, Gulf of Mexico." Continental Shelf Research **26**(17-18): 2073-2091.

Kineke, G. C., R. W. Sternberg, et al. (1996). "Fluid-mud processes on the Amazon continental shelf." Continental Shelf Research **16**(5-6): 667-696.

Kineke, G. C., K. J. Woolfe, et al. (2000). "Sediment export from the Sepik River, Papua New Guinea: evidence for a divergent sediment plume." Continental Shelf Research **20**(16): 2239-2266.

Klavins, M., A. Briede, et al. (2000). "Heavy metals in rivers of Latvia." Science of the Total Environment **262**(1-2): 175-183.

Knabb, R. D., J. R. Rhome, et al. (2006). Tropical cyclone report: Hurricane Katrina 23-30 August 2005. Miami, Florida, National Hurricane Center**:** 43.

Ko, D. S., C. Rowley, et al. (2005). "A real-time coastal ocean prediction experiment." NRL Review(2005): 183-186.

Kostoglidis, A., C. B. Pattiaratchi, et al. (2005). "CDOM and its contribution to the underwater light climate of a shallow, microtidal estuary in south-western Australia." Estuarine, Coastal and Shelf Science **63**(4): 469-477.

Kourafalou, V. H. (1999). "Process studies on the Po River plume, North Adriatic Sea." Journal of Geophysical Research-Oceans **104**(C12): 29963-29985.

Koutitonsky, V. G. (1979). "Water Mass-Transport at the Entrance of the St-Lawrence Estuary." Naturaliste Canadien **106**(1): 75-88.

Lalah, J. O., E. Z. Ochieng, et al. (2008). "Sources of heavy metal input into Winam Gulf, Kenya." Bulletin of Environmental Contamination and Toxicology **81**(3): 277-284.

Leatherman, S. P. (1987). "ANNOTATED CHRONOLOGICAL BIBLIOGRAPHY OF BARRIER-ISLAND MIGRATION." Journal of Coastal Research **3**(1): 1-14.

Lee, C. M., M. Orlic, et al. (2007). "Introduction to special section: recent advances in oceanography and marine meteorology of the Adriatic Sea." Journal of Geophsical Research-Part C-Oceans **112**(C3): 3 pp.-3 pp.

Lehman, P. W. (2000). "The influence of climate on phytoplankton community biomass in San Francisco Bay Estuary." Limnology and Oceanography **45**(3): 580-590.

Leuttich, R. A., J. J. Westerink, et al. (1992). ADCIRC: An advanced three-dimensional circulation model for shelves, coasts, and estuaries. Report 1: Theory and methodology of ADCIRC-2DDI and ADCIRC-3DI. Technical Report**:** 168.

Levasseur, A., L. Shi, et al. (2007). "A three-dimensional hydrodynamic model of estuarine circulation with an application to Southampton Water, UK." Estuarine Coastal and Shelf Science **73**(3-4): 753-767.

Liu, J. T., J. J. Hung, et al. (2009). "Partition of suspended and riverbed sediments related to the salt-wedge in the lower reaches of a small mountainous river." Marine Geology **264**(3-4): 152-164.

Liu, Z., W. L. Kingery, et al. (2008). "Assessment of water quality conditions in the St Louis Bay watershed." Journal of Environmental Science and Health Part a-Toxic/Hazardous Substances & Environmental Engineering **43**(5): 468-477.

Liu, Z. J., N. B. Hashim, et al. (2010). "Fecal coliform modeling under two flow scenarios in St. Louis Bay of Mississippi." Journal of Environmental Science and Health Part a-Toxic/Hazardous Substances & Environmental Engineering **45**(3): 282-291.

Liu, Z. J., W. L. Kingery, et al. (2008). "Modeling nutrient dynamics under critical flow conditions in three tributaries of St. Louis Bay." Journal of Environmental Science and Health Part a-Toxic/Hazardous Substances & Environmental Engineering **43**(6): 633-645.

Ludwick, J. C. (1974). "Tidal Currents and Zig-Zag Sand Shoals in a Wide Estuary Entrance." Geological Society of America Bulletin **85**(5): 717-726.

Lytle, T. F. and J. S. Lytle (1982). "Heavy-Metals in Oysters and Clams of St-Louis Bay, Mississippi." Bulletin of Environmental Contamination and Toxicology **29**(1): 50-57.

Lytle, T. F. and J. S. Lytle (1983). "Anthropogenic Organic Pollutants in Sediments of Mississippi Sound." Abstracts of Papers of the American Chemical Society **185**(Mar): 10-Envr.

Lytle, T. F. and J. S. Lytle (1990). "Heavy-Metals in the Eastern Oyster, Crassostrea-Virginica, of the Mississippi Sound." Bulletin of Environmental Contamination and Toxicology **44**(1): 142-148.

Manning, A. J., S. J. Bass, et al. (2006). "Floc properties in the turbidity maximum of a mesotidal estuary during neap and spring tidal conditions." Marine Geology **235**(1-4): 193-211.

Marciano, R., Z. B. Wang, et al. (2005). "Modeling of channel patterns in short tidal basins." Journal of Geophysical Research-Earth Surface **110**(F1).

Martin, P. J., S. R. Smith, et al. (2009). Use of the Oregon State University Tidal Inversion Software (OTIS) to generate improved tidal prediction in the East-Asian seas. Memorandum Report, Naval Research Laboratory**:** 29.

Martinho, F., I. Viegas, et al. (2008). "Assessing estuarine environmental quality using fish-based indices: Performance evaluation under climatic instability." Marine Pollution Bulletin **56**(11): 1834-1843.

Mcbee, J. T. and W. T. Brehm (1982). "Spatial and Temporal Patterns in the Macrobenthos of St-Louis Bay, Mississippi." Gulf Research Reports **7**(2): 115-124.

McBride, R. A. (1999). Spatial and temporal distribution of historical and active tidal inlets: Delmarva Peninsula and New Jersey, USA. New York, Amer Soc Civil Engineers.

McCreary, S., R. Twiss, et al. (1992). "LAND-USE CHANGE AND IMPACTS ON THE SAN-FRANCISCO ESTUARY - A REGIONAL ASSESSMENT WITH NATIONAL POLICY IMPLICATIONS." Coastal Management **20**(3): 219-253.

Menon, M. G., R. J. Gibbs, et al. (1998). "Accumulation of muds and metals in the Hudson River estuary turbidity maximum." Environmental Geology **34**(2-3): 214-222.

Michalik, B. (2008). "NORM impacts on the environment: An approach to complete environmental risk assessment using the example of areas contaminated due to mining activity." Applied Radiation and Isotopes **66**(11): 1661-1665.

Miles, A. K. and M. A. Ricca (2010). "Temporal and spatial distributions of sediment mercury at salt pond wetland restoration sites, San Francisco Bay, CA, USA." Science of the Total Environment **408**(5): 1154-1165.

Mitchell, S. B. and J. R. West (2002). Particle size distribution in an estuarine turbidity maximum region. Fine Sediment Dynamics in the Marine Environment. J. C. Winterwerp and C. Kranenburg. Amsterdam, Elsevier Science Bv. **5:** 251-263.

Monismith, S. G., W. Kimmerer, et al. (2002). "Structure and flow-induced variability of the subtidal salinity field in northern San Francisco Bay." Journal of Physical Oceanography **32**(11): 3003-3019.

Morey, S. L., P. J. Martin, et al. (2003). "Export pathways for river discharged fresh water in the northern Gulf of Mexico." Journal of Geophysical Research-Oceans **108**(C10).

Murrell, M. C., J. T. Hollibaugh, et al. (1999). "Bacterioplankton dynamics in northern San Francisco Bay: Role of particle association and seasonal freshwater flow." Limnology and Oceanography **44**(2): 295-308.

Nakayama, K., T. Okada, et al. (2005). "Mechanism responsible for fortnightly modulations in estuarine circulation in Tokyo Bay." Estuarine Coastal and Shelf Science **64**(2-3): 459-466.

Nghiem, T. L., D. T. Le, et al. (2009). SEDIMENT TRANSPORT AND MORPHODYNAMICS OF MY A INLET, VIETNAM, IN THE LOW FLOW SEASON. 5th International Conference on Asian and Pacific Coasts, Singapore, World Scientific Publ Co Pte Ltd.

Nidzieko, N. J., J. L. Hench, et al. (2009). "Lateral Circulation in Well-Mixed and Stratified Estuarine Flows with Curvature." Journal of Physical Oceanography **39**(4): 831-851.

Ogston, A. S., D. A. Cacchione, et al. (2000). "Observations of storm and river flood-driven sediment transport on the northern California continental shelf." Continental Shelf Research **20**(16): 2141-2162.

Oram, J. J., L. J. McKee, et al. (2008). "A mass budget of polybrominated diphenyl ethers in San Francisco Bay, CA." Environment International **34**(8): 1137-1147.

Overstreet, R. M. and R. W. Heard (1982). "Food Contents of 6 Commercial Fishes from Mississippi Sound." Gulf Research Reports **7**(2): 137-149.

Park, K., H. V. Wang, et al. (2008). "A model study of the estuarine turbidity maximum along the main channel of the upper Chesapeake bay." Estuaries and Coasts **31**(1): 115-133.

Pereira, W. E., F. D. Hostettler, et al. (1999). "Sedimentary record of anthropogenic and biogenic polycyclic aromatic hydrocarbons in San Francisco Bay, California." Marine Chemistry **64**(1-2): 99-113.

Perry, H. M. (1998). The estuarine ecosystem. Marine Resources and History of the Mississippi Gulf Coast. D. M. McCaughan, Mississippi Department of Marine Resources. **II:** 75-86.

Perry, H. M., C. K. Eleuterius, et al. (1995). "Settlement patterns of Callinectes sapidus megalopae in Mississippi sound: 1991, 1992." Bulletin of Marine Science **57**(3): 821-833.

Perry, H. M. and J. A. Mclelland (1981). "1st Recorded Observance of the Dinoflagellate Prorocentrum-Minimum (Pavillard) Schiller 1933 in Mississippi Sound and Adjacent Waters." Gulf Research Reports **7**(1): 83-85.

Pirazzoli, P. A. and A. Tomasin (1999). "Recent abatement of easterly winds in the northern Adriatic." International Journal of Climatology **19**(11): 1205-1219.

Postma, L., P. M. A. Boderie, et al. (2003). "Component software systems for surface water simulation." Computational Science - Iccs 2003, Pt I, Proceedings **2657**: 649-658.

Priddy, R. R., R. M. Crisler, et al. (1954). "Sediments of Parts of Mississippi Sound." Geological Society of America Bulletin **65**(12): 1366-1367.

Pritchard, D. W. (1967). What is an estuary: physical viewpoint. Estuaries. G. H. Lauf. Washington, D.C., A.A.A.S. **83:** 3-5.

Radakovitch, O., V. Roussiez, et al. (2008). "Input of particulate heavy metals from rivers and associated sedimentary deposits on the Gulf of Lion continental shelf." Estuarine Coastal and Shelf Science **77**(2): 285-295.

Ritson, P. I., R. M. Bouse, et al. (1999). "Stable lead isotopic analyses of historic and contemporary lead contamination of San Francisco Bay estuary." Marine Chemistry **64**(1-2): 71-83.

Roman, C. T., N. Jaworski, et al. (2000). "Estuaries of the northeastern United States: Habitat and land use signatures." Estuaries **23**(6): 743-764.

Ross, S. T., W. T. Slack, et al. (2009). "Estuarine and Coastal Habitat Use of Gulf Sturgeon (Acipenser oxyrinchus desotoi) in the North-Central Gulf of Mexico." Estuaries and Coasts **32**(2): 360-374.

Ruhl, C. A., D. H. Schoellhamer, et al. (2001). "Combined use of remote sensing and continuous monitoring to analyse the variability of suspended-sediment concentrations in San Francisco Bay, California." Estuarine Coastal and Shelf Science **53**(6): 801-812.

Runner, M. S. and T. Floyd (2002). "Water quality monitoring and data collection in the Mississippi Sound." Proceedings of the Fifty-Third Annual Gulf and Caribbean Fisheries Institute: 681-688.

Saeedi, M. and A. R. Karbassi (2008). "Estuarine capacity in removal of trace metals from contaminated river water, Southern Caspian Sea." Water and Environment Journal **22**(3): 193-198.

Schoellhamer, D. H. (2002). "Variability of suspended-sediment concentration at tidal to annual time scales in San Francisco Bay, USA." Continental Shelf Research **22**(11-13): 1857-1866.

Schroeder, W. W., O. K. Huh, et al. (1985). "Satellite observations of the circulation east of the Mississippi Delta: Cold-air outbreak conditions." Remote Sensing of Environment **18**(1): 49-58.

Schubel, J. R. (1968). "Turbidity Maximum of Northern Chesapeake Bay." Science **161**(3845): 1013-&.

Seim, H. E., B. Kjerfve, et al. (1987). "Tides of Mississippi Sound and the adjacent continental shelf." Estuarine, Coastal and Shelf Science **25**(2): 143-156.

Shellenbarger, G. G., N. D. Athearn, et al. (2008). "Fecal indicator bacteria and Salmonella in ponds managed as bird habitat, San Francisco Bay, California, USA." Water Research **42**(12): 2921-2930.

Shiraki, Y. and T. Yanagi (2007). "Dynamics of estuarine residual circulation in a narrow channel including tidal-nonlinear effects." Journal of Oceanography **63**(3): 413-425.

Slingerland, R., R. W. Selover, et al. (2008). "Building the Holocene clinothem in the Gulf of Papua: An ocean circulation study." Journal of Geophysical Research-Earth Surface **113**(F1): -.

Smith, L. M., J. M. Macauley, et al. (2009). "Water Quality in the Near Coastal Waters of the Gulf of Mexico Affected by Hurricane Katrina: Before and After the Storm." Environmental Management **44**(1): 149-162.

Smith, S. J. and N. C. Kraus (1999). Mitigation of a beach-fill hot spot, Monmouth Beach, New Jersey. New York, Amer Soc Civil Engineers.

Smith, S. V. and J. T. Hollibaugh (2006). "Water, salt, and nutrient exchanges in San Francisco Bay." Limnology and Oceanography **51**(1): 504-517.

Stacey, M. T., J. P. Fram, et al. (2008). "Role of tidally periodic density stratification in the creation of estuarine subtidal circulation." Journal of Geophysical Research-Oceans **113**(C8): 13.

Stone G. W. (1998). Soundside wave-current and beach-nearshore profile adjustment to storms and cold fronts field program along western Santa Rosa Island, National Park Service. **III:** 45.

Stone, G. W. (1998). Beach nourishment monitoring program at Fort Massachusetts, West Ship Island, Mississippi, National Park Service. **I:** 16.

Stone, G. W. and F. W. Stapor (1996). "A nearshore sediment transport model for the northeast Gulf of Mexico coast, USA." Journal of Coastal Research **12**(3): 786-793.

Supan, J. (1983). "Evaluation of a Leased Oyster Bottom in Mississippi Sound." Gulf Research Reports **7**(3): 261-266.

Tappin, A. D., J. R. W. Harris, et al. (2003). "The fluxes and transformations of suspended particles, carbon and nitrogen in the Humber estuarine system (UK) from 1994 to 1996: results from an integrated observation and modelling study." The Science of The Total Environment **314-316**: 665-713.

Teles, M. and A. Barata (2005). "Morphodynamics of the Tagus estuary entrance. Simulation of alternative solutions for bar maintenance." Coastal Engineering 2004, Vols 1-4: 2280-2289.

Travis, W., J. Blanchfield, et al. (1998). San Francisco Bay wetland mitigation banking system. New York, Amer Soc Civil Engineers.

Tung, T. T., D. J. R. Walstra, et al. (2009). "Morphological Modeling of Tidal Inlet Migration and Closure." Journal of Coastal Research: 1080-1084.

Ufnar, D., J. A. Ufnar, et al. (2006). "Influence of coastal processes on high fecal coliform counts in the Mississippi Sound." Journal of Coastal Research **22**(6): 1515-+.

Uncles, R. J. and D. H. Peterson (1996). "The long-term salinity field in San Francisco Bay." Continental Shelf Research **16**(15): 2005-2039.

Uncles, R. J., J. A. Stephens, et al. (2006). "Properties of suspended sediment in the estuarine turbidity maximum of the highly turbid Humber Estuary system, UK." Ocean Dynamics **56**(3-4): 235-247.

Uncles, R. J., J. A. Stephens, et al. (2002). "The dependence of estuarine turbidity on tidal intrusion length, tidal range and residence time." Continental Shelf Research **22**(11-13): 1835-1856.

USEPA (1999). Ecological condition of estuaries in the Gulf of Mexico. Gulf Breeze, Florida, Office of Research and Development, National Health and Environmental Effects Research Laboratory 80.

USEPA (2006). An inventory of sources and environmental releases of dioxin-like compounds in the United States for the years 1987, 1995, and 2000. Washington, DC, National Center for Environmental Assessment.

Valente, A. S. and J. C. B. da Silva (2009). "On the observability of the fortnightly cycle of the Tagus estuary turbid plume using MODIS ocean colour images." Journal of Marine Systems **75**(1-2): 131-137.

Valentine, J. F. (1991). "Temporal Variation in Populations of the Brittlestars Hemipholis-Elongata (Say, 1825) and Microphiopholis-Atra (Stimpson, 1852) (Echinodermata, Ophiuroidea) in Eastern Mississippi Sound." Bulletin of Marine Science **48**(3): 597-605.

van Geen, A. and S. N. Luoma (1999). "The impact of human activities on sediments of San Francisco Bay, California: an overview." Marine Chemistry **64**(1-2): 1-6.

van Leussen, W. (1988). Aggregation of particles, settling velocity of mud flocs: A review. Physical processes in estuaries. J. Dronkers and W. v. Leussen. New York, Springer**:** 347-403.

Vijith, V., D. Sundar, et al. (2009). "Time-dependence of salinity in monsoonal estuaries." Estuarine, Coastal and Shelf Science **85**(4): 601-608.

Walker, N. D. (1996). "Satellite assessment of Mississippi River plume variability: Causes and predictability." Remote Sensing of Environment **58**(1): 21-35.

Walker, N. D. and A. B. Hammack (2000). "Impacts of winter storms on circulation and sediment transport: Atchafalaya-Vermilion Bay region, Louisiana, USA." Journal of Coastal Research **16**(4): 996-1010.

Walker, N. D., O. K. Huh, et al. (1996). "Evolution and structure of a coastal squirt off the Mississippi River delta: Northern Gulf of Mexico." Journal of Geophysical Research-Oceans **101**(C9): 20643-20655.

Wang, S. S., Z. M. Cao, et al. (2008). "Concentration distribution and assessment of several heavy metals in sediments of west-four Pearl River Estuary." Environmental Geology **55**(5): 963-975.

Warner, J. C., C. R. Sherwood, et al. (2008). "Development of a three-dimensional, regional, coupled wave, current, and sediment-transport model." Computers & Geosciences **34**(10): 1284-1306.

Weir, D. J. and J. Mcmanus (1987). "The Role of Wind in Generating Turbidity Maxima in the Tay Estuary." Continental Shelf Research **7**(11-12): 1315-1318.

White, P., K. Israel, et al. (2002). Use of sediment transport measurements to evaluate natural recovery potential. Columbus, Battelle Press.

Wiltshire, K. H., S. Harsdorf, et al. (1998). "The determination of algal biomass (as chlorophyll) in suspended matter from the Elbe estuary and the German Bight: A comparison of high-performance liquid chromatography, delayed fluorescence and prompt fluorescence methods." Journal of Experimental Marine Biology and Ecology **222**(1-2): 113-131.

Wolanski, E. (2007). Estuarine Ecohydrology. Amsterdam, The Netherlands, Elsevier.

Xie, D., Z. Wang, et al. (2009). "Modeling the tidal channel morphodynamics in a macro-tidal embayment, Hangzhou Bay, China." Continental Shelf Research **29**(15): 1757-1767.

Yanagi, T. and M. Shimomura (2006). "Seasonal variation in the transverse and layered structure of estuarine circulation in Ariake Bay, Japan." Continental Shelf Research **26**(20): 2598-2606.

Yang, S. L., D. Eisma, et al. (2000). "Sedimentary processes on an estuarine marsh island within the turbidity maximum rone of the Yangtze River mouth." Geo-Marine Letters **20**(2): 87-92.

Zelic, M., N. Levi, et al. "Alpine tectono-metamorphic history of the continental units from Vardar zone: the Kopaonik Metamorphic Complex (Dinaric-Hellenic belt, Serbia)." Geological Journal **45**(1): 59-77.

Zimmerman, J. R., J. D. Bricker, et al. (2008). "The stability of marine sediments at a tidal basin in San Francisco Bay amended with activated carbon for sequestration of organic contaminants." Water Research **42**(15): 4133-4145.